Synthesis and Characterization of Ruddlesden Popper Ferroic Materials

Tiago João Lopes Leal
Master's Degree in Engineering Physics
Department of Physics and Astronomy
Faculty of Sciences
University of Porto
2019

Supervisor
Dr. Armandina Maria Lima Lopes, FCUP

Co-Supervisor
Prof. Dr. João Pedro Esteves de Araújo, FCUP

U.PORTO
FACULDADE DE CIÊNCIAS
UNIVERSIDADE DO PORTO

U.PORTO
FEUP FACULDADE DE ENGENHARIA
UNIVERSIDADE DO PORTO

Todas as correções determinadas pelo júri, e só essas, foram efetuadas.

O Presidente do Júri,

Porto,
_____/_____/_____

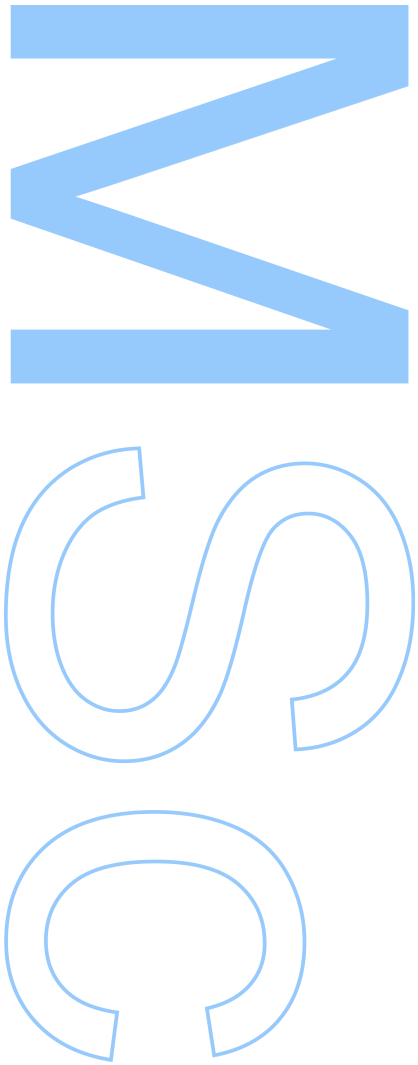

Tiago Leal

Synthesis and Characterization of Ruddlesden Popper Ferroic Materials

Supervisor: *Dr. Armandina Maria Lima Lopes*
Co-Supervisor: *Prof. Dr. João Pedro Esteves de Araújo*

Thesis submitted to the Faculty of Sciences of the University of Porto in fulfilment of the requirements for the degree of Integrated Master's in Engineering Physics

Department of Physics and Astronomy
Faculty of Sciences of the University of Porto
2019

“Eu não me envergonho de corrigir os meus erros e mudar de opinião, porque não me envergonho de raciocinar e aprender.”

***Alexandre Herculano**,*
A Portuguese writer, historian, journalist and poet.

Acknowledgements

This thesis is the culmination of a long period as an Engineering Physics student in the Physics and Astronomy Department at the Faculty of Science at the University of Porto. There were highs and lows and for those moments I could rely on people that helped me made it through. I will deeply remember all those moments and, for the ones not mentioned next, my sincerest thank you.

First I would like to thank the support, and the very first conversation about this topic, Prof. Dr. João Pedro Araújo for the openness and trust deposited on me. My supervisor, Dr. Armandina Lopes, for being so calm and available to clarify any doubts every time that I stepped in her office.

To the members of IFIMUP for their help and support. Namely, my group colleagues, Pedro Rodrigues for all the patience and the companionship in the laboratory time, Dr. Gonçalo Oliveira for the careful reading and suggestions on the drafts of this thesis and Ricardo Moreira for having to put up with me for more than a year.

Everyone from the ISOLDE-CERN facilities that provided essential help, especially Dr. João Guilherme Correia and Dr. João Nuno Gonçalves.

The FCT through the funding of the following projects: POCI-01-0145-FEDER-029454; CERN/FIS-PAR/0005/2017; POCI-01-0145-FEDER-032527 and NECL NORTE-01-0145-FEDER-022096.

To all my friends for the leisure times and the adventures that we spent together. May our curiosity drive us for more of these ventures.

My boyfriend Pedro, whose support and encouragement was fundamental. I hope to continue growing alongside you.

Last but not least, I thank my family, especially my parents, who always gave me the freedom to be me and encouraged me to proceed with my studies.

I deeply apologize if I forgot anyone.

Resumo

Esta tese explora as possíveis abordagens para o desenvolvimento de compostos ferróicos e multiferróicos à temperatura ambiente. Óxidos de cálcio manganês/titânio naturalmente estruturados em camadas têm despertado o interesse da comunidade científica devido às suas propriedades[1], em particular ferroelectricidade imprópria híbrida[i]. De forma a compreender a origem das propriedades destes sistemas, foram produzidas amostras policristalinas puras de Ca_2MnO_4, $Ca_3Mn_2O_7$ (CMO), $Ca_3Ti_2O_7$, $Ca_3Mn_{1.9}Ti_{0.1}O_7$ através de uma reacção de estado sólido, assim como filmes finos de CMO em substratos de $SrTiO_3$ e Si usando deposição por laser pulsado (PLD). Espectroscopia de correlações angulares perturbadas (PAC) foi usada nas amostras sólidas de forma a examinar distorções dos octaedros, uma característica de compostos naturalmente estruturados. A nossa caracterização fornece nova informação que pode ser útil na revelação de transições estruturais.

Para o sistema $\mathbf{Ca_2MnO_4}$, as medições sugerem uma transição de fase estrutural desde uma fase de baixa simetria para uma altamente simétrica a alta temperatura. A temperatura crítica associada a esta transição encontra-se por volta de 1049 - 1079 K.

Para o sistema $\mathbf{Ca_3Mn_2O_7}$, as medições demonstraram uma rota de transições estruturais, desde a conhecida estrutura polar a baixas temperaturas até uma estrutura de alta simetria a temperaturas superiores a 1150 K.

No caso do sistema $\mathbf{Ca_3Ti_2O_7}$, foi observado a distribuição das fracções dos ambientes locais, que foram ajustadas aos dados recolhidos em PAC, é proposta uma transição de fase a alta temperatura.

É apresentado ainda o estudo de materiais Ruddlesden Popper com a composição $\mathbf{Ca_3Mn_{2-x}Ti_xO_7}$ onde é discutido o efeito da substituição parcial dos iões de Mn por Ti na estabilização da fase polar $A2_1am$.

Finalmente, a deposição de **filmes finos** de $Ca_3Mn_2O_7$ em substratos de $SrTiO_3$ e Si foi realizada de forma a manipular novos materiais funcionais, dado que a tensão resultante dos filmes epitaxiais podem influenciar as propriedades magnetoelétricas[2]. Em todas as amostras foram encontradas reflexões que talvez indicam a presença de $Ca_3Mn_2O_7$.

[i] Traduzido livremente do Inglês, *Hybrid Improper Ferroelectricity*

Abstract

This thesis explores possible routes for the development of room temperature ferroic and multiferroic compounds. Naturally layered calcium manganese/titanium oxides have attracted the interest of the scientific community due to their properties, in special since they hold hybrid improper ferroelectricity[1]. In order to master the synthesis of these Ruddlesden Popper materials, polycrystalline samples of Ca_2MnO_4, $Ca_3Mn_2O_7$(CMO), $Ca_3Ti_2O_7$, $Ca_3Mn_{1.9}Ti_{0.1}O_7$ were produced by solid state reaction. In all cases pure materials were synthesized. Thin films of CMO were deposited in $SrTiO_3$ and Si substrates by using Pulsed Layer Deposition (PLD). Perturbed angular correlation (PAC) spectroscopy was implemented in the bulk samples to probe the octahedra distortions, characteristic of naturally layered compounds. Our study provided new information that could help to sort the structural transitions.

For the **Ca_2MnO_4** system, measurements suggest a structural phase transition from a low-symmetric phase to a highly symmetric at high-temperature one. The critical temperature associated with this transition should be around 1049 - 1079 K.

For the **$Ca_3Mn_2O_7$** system, measurements reveal a structural path, from the known low-temperature polar structure up to a highly symmetric phase at high-temperatures (above 1150 K).

In the case of **$Ca_3Ti_2O_7$** system, observing the probe distribution throughout the different local environments obtained from the PAC fittings, a phase transition is suggested to occur at high-temperatures.

A study of the intermediary Ruddlesden Popper materials with the chemical composition of **$Ca_3Mn_{2-x}Ti_xO_7$** is presented. Here it is discussed the stabilization of the polar phase $A2_1am$ through the partial ion substitution of Mn and Ti.

Finally, the deposition of $Ca_3Mn_2O_7$ **thin films** on $SrTiO_3$ and Si substrates was performed as a path to tailor and engineer new functional materials, given that the resulting strain from epitaxial films can influence the magnetoelectric properties[2]. In all the samples it was found particular reflections that might indicate deposition of $Ca_3Mn_2O_7$.

Contents

List of Figures

List of Tables

List of Abreviations

- **BB**, Bragg-Brentano
- **AFM**, Antiferromagnetic
- **CERN**, European Organization for Nuclear Research
- **EDS**, Energy Dispersive X-ray Spectroscopy
- **EFG**, Electric Field Gradient
- **E**, Electric Field
- **FC**, Field-Cooling
- **FCC**, Field-Cool Cooling
- **FCH**, Field-Cool Heating
- **FCUP**, Faculdade Ciências da Universidade do Porto
- **FE**, Ferroelectric
- ***F***, Free Energy
- **FEP**, Ferroelectric Polarization
- **FM**, Ferromagnetic
- **FWHM**, Full Width at Half Maximum
- ***H***, Magnetic Field
- **HI**, Hyperfine Interactions
- **IFIMUP-IN**, Instituto de Física dos Materiais da Universidade do Porto
- **ISOLDE**, On-line Isotope Mass Separator
- **JT**, Jahn-Teller
- **LE**, Local Environment
- ***M***, Magnetization
- **ME**, Magnetoelectric
- **MHF**, Magnetic Hyperfine Field
- **PAC**, Perturbed Angular Correlations
- **PB**, Parallel Beam
- **PLD**, Pulsed Lase Deposition
- **P**, Polarization
- **PSB**, Proton-Synchrotron Booster
- **PXRD**, Powder X-ray Diffraction
- **RP**, Ruddlesden Popper
- **RT**, Room Temperature
- **SEM**, Scanning Electron Microscopy
- **SQUID**, Superconducting Quantum Interference Device
- **XPS**, X-ray Photoelectron Spectroscopy
- **XRD**, X-ray Diffraction
- **ZFC**, Zero Field Cooling
- θ_P, Curie-weiss Temperature
- μ_{eff}, Effective paramagnetic moment
- J_{AFM}, Antiferromagnetic interaction
- J_{FM}, Ferromagnetic interaction
- B_{hf}, Magnetic Hyperfine Field
- χ, Magnetic susceptibility
- $M(H)$, M vs H
- $M(T)$, M vs T
- χ^{-1}, Reciprocal susceptibility
- T_{C}, Curie Temperature
- T_{N}, Néel Temperature
- T, Temperature

Thesis outline

This thesis is structured in 6 chapters, comprising an introduction with General aspects, the Experimental techniques, 3 chapters on the main Results and Discussion and a final chapter with Conclusions. A summary is given:

In **Chapter 1**, it is briefly introduced the background knowledge on perovskites and multiferroicity. The naturally layered Ruddlesden Popper series are described, as well as the associated structural phase transitions and the respective functional properties, *e.g.* the hybrid improper ferroelectricity and the uniaxial negative thermal expansion.

In **Chapter 2**, it is presented a brief description of the used experimental techniques. This comprises the synthesis method, followed by the characterization techniques such as X-Ray Diffraction (XRD), Scanning Electron Microscopy (SEM), Superconducting Quantum Interference Device magnetometer (SQUID) and Perturbed Angular Correlation (PAC).

In **Chapter 3**, it is introduced the $Ca_{n+1}Mn_nO_{3n+1}$ compounds, followed by the study of its structure and magnetic properties. Bulk polycrystalline n = 1, 2 samples were prepared using the method of solid state reaction and n = 2 thin films were deposited on $SrTiO_3$/Si substrates by pulsed laser deposition.

In **Chapter 4**, mimicking the structure of the previous chapter, it is introduced the $Ca_3Ti_2O_7$ compound and the study on its structural properties are presented. The bulk polycrystalline samples of $Ca_3Ti_2O_7$ were synthesized by solid state reaction.

In **Chapter 5**, it is presented the effort towards enhancing some of the properties from the previous $Ca_3Mn_2O_7$ and $Ca_3Ti_2O_7$. It is shown the initial studies of the intermediary phase $Ca_3Mn_{1.9}Ti_{0.1}O_7$ on its structure and magnetic properties.

Finally, the main conclusions and perspectives of this thesis are summarized.

Motivation

Since the silicon industrial revolution during the 1950s, research and developments in materials science have radically impacted and transformed our society. Everyday objects and systems, such as smartphones and wireless communications are rooted in the breakthroughs achieved of solid-state physics from that time onward.

Materials science is, thus, recognized as one of the main factors driving development and economic growth. Now with a strong drive for multifunctional materials that fulfill the goal of miniaturization and increasing efficiency[3,4]. The increased interest in multiferroic materials over the past 15 years[5] comes to meet this purpose.

Multiferroic materials make it possible to exploit the functionalities of two ferroic orders, *e.g.* a magnetic bit may be complemented by an electric bit to establish a four-state memory element. Hence, suggesting a dramatic increase in data storage density. Furthermore, novel functionalities that are not present alone in either ferromagnetic or ferroelectric state could be induced by the coupling between the states[6]. Thus, their attributed potential for technological applications.

ABO_3 perovskites have been studied by solid-state scientists for decades since they display a wide variety of chemical and physical properties[7]. Despite this diversity of properties, very few of these materials are ferroelectric in bulk.

In 2005, the discovery[8] of hybrid improper ferroelectricity in artificial superlattices of $SrTiO_3$/$PbTiO_3$ unveiled an approach to design novel ferroelectric materials. Later, in 2011, it was complemented[1] with the finding of naturally layered systems, the Ruddlesden Popper (RP) phase series. Here, the outstanding physical properties arise from its lattice distortions offering an alternative route to develop room-temperature multiferroics materials[9].

This thesis aims to provide new information that can assist in clarifying the origin of the properties exhibited in naturally layered perovskites.

CHAPTER 1

General Aspects

1.1 Perovskite

The naturally occurring perovskite, $CaTiO_3$, was first named by Gustav Rose as a tribute to the Russian mineralogist Lev A. Perovski in 1839. From this date, the composition ABY_3 has been referred to as perovskites. Usually, A and B are cations from the group I to group XV elements and Y is an anion from the group XV, XVI or XVII. Perovskite-type compounds and related structures represent a large family of important inorganic materials, which have been comprehensively studied throughout the years[10] and have been employed in many technological applications[11].

As can be seen from Fig. 1.1, the perovskite structure consists of BY_6 octahedra interlinked with each corner. Between these octahedral layers, the A ions are situated in the large central vacancies, where they are surrounded by twelve Y ions[i].

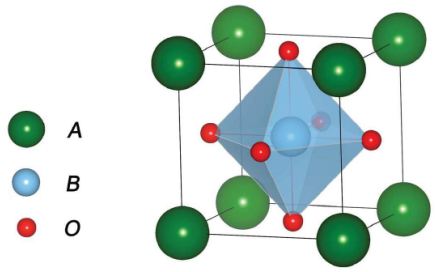

Figure 1.1 – Representation of the ideal ABO_3 perovskite structure which is of cubic symmetry with the space group of $Pm\bar{3}m$.

Perovskites and related materials are known to exhibit many interesting properties that arise in many cases due to octahedral distortions by strongly influencing the structural, magnetic, orbital, and electronic degrees of freedom[12].

1.1.1 Layered perovskites

Among perovskite oxides, the layered type is especially interesting due to the ability it presents for further functionalization. These layered types can be achieved from a regular perovskite by doping with a chemically different element, *e.g.* A' atom intercalated

[i] From therein is assumed that the chosen element Y is oxygen, O.

with an A atom, called **Double perovskites** $AA'B_2O_6$ or by naturally layer an inter growth of AO rock salt layers. In the last, the perovskite ABO_3 layers extend infinity in two dimensions with a given periodicity in the *c*-direction. Hence, they can form superstructures that are known as: the **Aurivillius phase**, $A'_2O_2A_{n-1}B_nO_{3n+1}$; the **Dion-Jacobson phase**, $A'A_{n-1}B_nO_{3n+1}$; or the **Ruddlesden Popper (RP) phase**, $AO(ABO_3)_n$, depending on the structure of the rock salt layer, see all structures in Fig. 1.2.

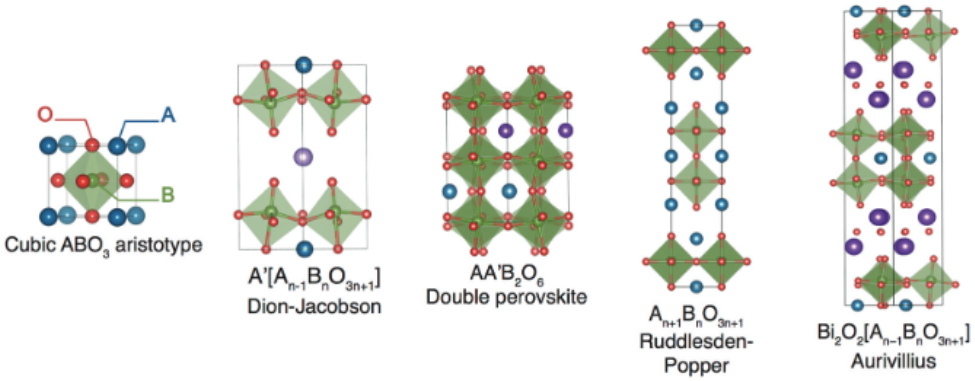

Figure 1.2 – Set of naturally layered perovskites derived from the cubic ABO_3. In the Dion–Jacobson phases, A' is usually an alkali cation, although it can also be a transition metal halide complex. In the Ruddlesden Popper phase the perovskite blocks are interleaved with a AO layer and, in the Aurivillius phase, with A'_2O_2 layers. (Taken from Ref. 3)

Some of these structures can also be fabricated artificially using, for example, epitaxial growth techniques. Recent works in Ruddlesden Popper compounds were able to synthesize $n = 1-5$[13], $n = 4-6$[14] and $n = 10$[15] samples. Disapproving the earlier prediction that $n > 3$ phases would be unstable and decompose[16].

1.1.2 Ruddlesden Popper Phase Series: $AO(ABO_3)_n$

Already, in the years 1957 and 1958, *S.N. Ruddlesden* and *P. Popper* were investigating[17,18] some materials that later on became known as the Ruddlesden Popper Phase Series, namely Sr_2TiO_4, Ca_2MnO_4, $SrLaAlO_4$, $Sr_3Ti_2O_7$. Aiming to determine their structural properties, using x-ray powder diffraction studies they were able to associate these materials to having a K_2NiF_4 type structure, which was found earlier by *Balz*[19] to have a high symmetry *I4/mmm* tetragonal structure.

The Ruddlesden Popper (RP) series, are defined by having a rock salt layer of an oxide AO intercalated with one or multiple slabs of ABO_3 perovskite stacked alternately along the c-axis. The resulting stoichiometry is of the type: $A_{n+1}B_nO_{3n+1}$, with $n = 1, 2, \ldots, \infty$ (see Fig. 1.3). Here, *A* represents an alkali, alkali-earth or rare earth metal and *B* a transition metal element. The first two elements, A or B, can be partly substituted by another chemically different one, in these cases, they are indicated as AA' or BB'.

The shift from three-dimensional to two-dimensional linkage of BO_6 octahedra in the

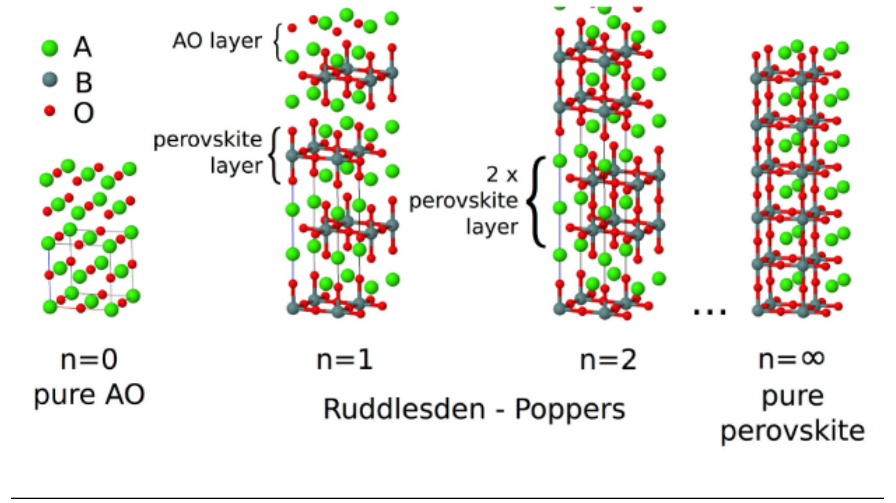

Figure 1.3 – Ruddlesden Popper Phase Series from the parent oxide AO (n = 0), with one (n = 1) and two (n = 2) slabs of perovskite to the pure perovskite ABO_3 ($n = \infty$). (Taken from Ref. 20)

RP compounds, plays an important role in their electronic conductivity, *e.g.* $SrRuO_3$[15] shows metallic conductivity while Sr_2RuO_4 shows in fact superconductivity at low temperatures.

The RP materials have a really broad scope of possible applications since they display different properties such as giant magnetoresistance[21], catalytic activity[22], superconductivity[23], several optical properties and ferroelectricity[1]. This last one is related to one of the most promising characteristics, the hybrid improper ferroelectricity (HIF)[1,24–26] (as it will be discussed in Section 1.2.1.1).

In the literature can be found several RP crystals with different A and B atoms, *e.g.* A = Ca, Sr, La, B = Ti, Mn, V, Fe, Ru or Ir[15,18,27,28].

The octahedral rotations in perovskites are driven by several factors such as coordination preferences of the A-site cation or pressure/epitaxial strain. In some space groups with octahedral rotations, the A-site cation can shift from its 'ideal' $Pm\bar{3}m$ position to further optimize its coordination environment. For example, in *Pnma* space group, the A-site cation can displace in an antipolar pattern, see Fig. 1.4 c). This displacement will contribute to an observable polarization within the perovskites layers as will be described in Section 1.2.3. Furthermore, the octahedral rotations in perovskites are known to respond strongly to pressure and epitaxial strain. For example, it was observed by *Benedek and Fennie*[1], that the energy barrier to switching the sign of the rotation/tilting of the octahedra can be tuned if the material is under (biaxial) compressive/tensile strain, respectively.

The structural transitions of the RP phase series are explained by their characteristically layered composition. Here, the octahedra layer has at least two distortions modes: a rotational and a tilting mode. Each one of these modes will condense into a different space group symmetry, see Fig. 1.5.

These octahedral distortions are most often observed when the *A* cations are not

quite large, expressed in a low ($\ll 1$) tolerance number *t*, see Section 1.1.4.

1.1.3 Notation for octahedral tilting

Glazer has established a compact notation[29] to characterize the rotations[ii] previously introduced. This notation, the **Glazer notation**, consists of three letters, *a*, *b*, *c*, each with superscript 0, + or –. Each of the letters refers to the x, y and z axes of the underlying cubic perovskite structure $Pm\bar{3}m$. Two or more equal letters represent the axes in which the magnitude of the tilts are the same. The superscripts + and – refer to tilts about an axis in the given x, y or z-direction. For +, successive tilts about an axis are equal and in the same direction. For –, successive tilts about an axis are equal in magnitude but opposite directions. Since the octahedra are corner linked, successive tilts in directions perpendicular to the axis are constrained to be equal in magnitude but opposite directions. The superscript 0 means that there is no tilt about an axis in that direction. All possible tilts can be written as a linear combination of the three + tilt systems and its equivalent – tilt system, *e.g.* $a^+b^0b^0$, $b^0a^+b^0$ and $b^0b^0a^+$ about the x, y and z axes, respectively. In that way, $a^-a^-b^+$ denotes a tilt system with – tilts (opposite direction) about both the *x* and *y* axes [110], see Fig. 1.4 b), and + tilts (same direction) about the *z* axis [001], see Fig. 1.4 a). In addition, the repetition of the letter *a* means that the tilts about the *x* axis are equal in magnitude in this structure.

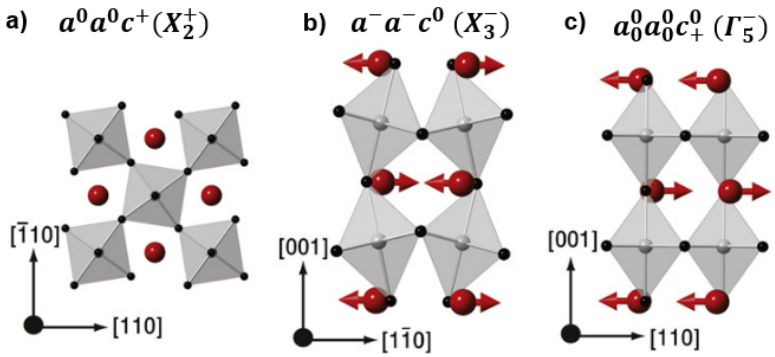

Figure 1.4 – The *Pnma* structure (rotation pattern $a^-a^-c^+$) can be described primarily by three different normal modes of $Pm\bar{3}m$: **a)** octahedral rotation about [001], **b)** rotation about [110] with A-site displacement, and **c)** antipolar A-site displacement without any rotation or tilt. On top the Glazer notation and respective irrep notation equivalent. (Taken from Ref. 12)

In the case where a ferroelectric *B* cation can be displaced, see Fig. 1.4 c), such as in the intensively studied $BaTiO_3$[30] case, its tetragonal ferroelectric structure could be represented, in **irrep notation** (irreducible representation) by Γ_5^-. Although not common, in a modified Glazer notation[31], this displacement could be represented by $a_0^0a_0^0c_+^0$, where the single subscript + denotes *B* cation displacements in the + direction along the z axis without any tilting. The analogous reasoning would apply for a – subscript.

[ii] Generally, throughout this thesis the use of "rotation" means a rotation of the basal oxygen plane around the [001] and "tilt" means a tilt around the [100] axis or [110] axis.

Both notations are used to give a better intuition of what is happening in a perovskite-based material during structural transitions. In Fig. 1.5 it can be seen the direct correspondence that certain tilts/rotations and which crystallographic space groups they will make the system transition to.

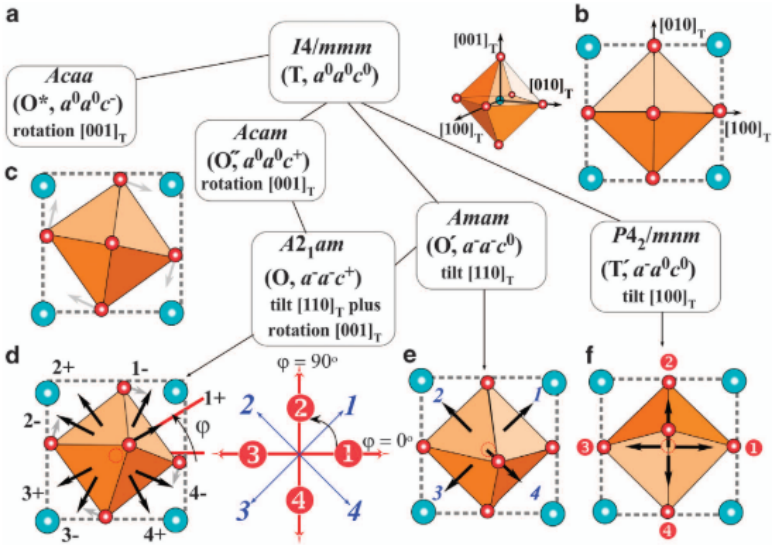

Figure 1.5 – Diagram of possible space groups with the corresponding tilts in Glazer notation for the bi-layered perovskite $A_3B_2O_7$. Lines link the group-subgroup relations. From the undistorted *I*4/*mmm* and under the BO_6 octahedral rotation and tilting modes for the experimentally observed *Acaa* (X_1^-) and $A2_1am$ (X_2^-+X_3^-) structural phases. It is highlighted the combination of an $a^0a^0c^+$ (X_2^+), of the *Acam* space group, and the $a^-a^-c^0$ (X_3^-), present in the *Amam*, to condense in the $A2_1am$ symmetry. (Taken from Ref. 32)

1.1.4 Tolerance Factor

The ideal perovskite structure, as referred previously, is a cubic one in the $Pm\bar{3}m$ space group[30]. However, these structures can be found to be distorted due to different ion sizes, for example between A and B atoms. As a way to evaluate possible distortions and stability in crystal structures, of the type ABX_3, *Goldschmidt* introduced a metric called the tolerance factor[33]:

$$t = \frac{r_A + r_X}{\sqrt{2}(r_B + r_X)} \tag{1.1}$$

where, r_A, r_B and r_X are, respectively, the average ionic radius of the *A*, *B* and *X* ions.

For $t < 1$ the $B-X$ bonds are put under tension whereas $A-X$ bonds are under compression, thus, it is observed a cooperative rotation of the BO_6 octahedra and a corresponding reduction of the strain causing the octahedral to tilt, rotate or expand, leading to the adoption of an orthorhombic/rhombohedral structure type. In the ideal case of a cubic structure, t corresponds to ~ 1 and when *t* is much greater than 1 results in a hexagonal/tetragonal type structure.

Changing the tolerance factor of a compound can be experimentally accomplished

by chemistry and internal structure, *e.g.* through substitution of a cation with a different ionic radius either in A or B sites or a combination of both. Take into account that this factor only considers the ionic radius and perovskites are not truly ionic compounds, nevertheless remains as a popular tool to infer these structures.

A practical application of the tolerance factor in materials engineering can be seen in Ref. 34 where it is studied the impact of the tolerance factor with the establishment of ferroelectricity. It is proved that are the cation displacements that accompany the rotations, rather than the rotations by themselves, that play a decisive role in generating ferroelectricity in these cases. In Ref. 35 it was found that as the tolerance factor of the ABO_3 perovskite, the parent of the corresponding n = 2 RP compound decreases, the octahedral rotations, and consequently the polarization and the switching barrier, would increase, see Fig. 1.6.

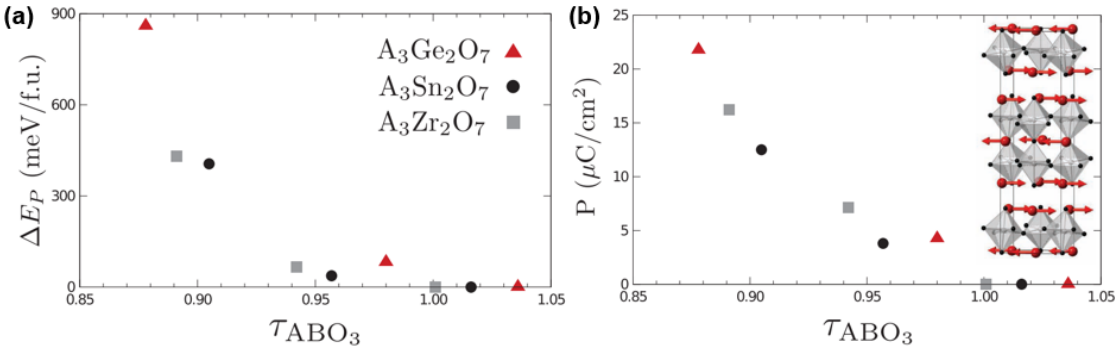

Figure 1.6 – **a)** The polarization switching barrier and **b)** the respective polarization of the n = 2 Ruddlesden Popper materials arranged by the tolerance factor of the ABO_3 parent perovskite. Inset: representation of the cation displacement (Γ_5^-) pattern of the A-sites in the ferroelectric $a^-a^-c^+$ structure. (Taken from Ref. 35)

More recently it was presented a new tolerance factor by *Bartel* that takes into consideration the oxidation states of the *A*, *B* and *X* ions. Further understanding about this suggestion can be found in Ref. 36.

1.2 Multiferroicity

Coined by Hans Schmid in 1994 [37], and extensively studied in the former Soviet Union [38], the possibility of magnetoelectric coupling in solids was first predicted by Pierre Curie in 1894 based on crystal symmetry considerations [39].

Multiferroic materials are a class of compounds, in which at least two primary ferroic properties, namely, ferroelectricity, ferromagnetism, ferroelasticity, and more recently a proposed ferrotoroidicity [40], coexist. In fact, one of the goals of this work is the research into what are called ”multiferroic magnetoelectrics”, single-phase materials that have magnetic and ferroelectric orders with cross-coupling effects, see Fig. 1.8 a).

These materials are a huge source of technological applications [5,40,41] because they

can simultaneously display tunable mechanical, magnetic, electric/dielectric, thermal, and optical properties. Being deployed in sensors, microwave, and energy harvesting devices, photovoltaic technologies, solid-state refrigeration, data storage recorders, and random access multi-state memories. In this last one, the coupling could, in principle, permit data to be written electrically and read magnetically[40], *i.e.*, the electric properties can be controlled by magnetic fields and the magnetic properties by electric fields.

The major difference from a multiferroic magnetoelectric[iii] to a material with magnetoelectric coupling, see Fig. 1.7, it is that the first has both a spontaneous magnetization and a spontaneous polarization while the second may exist whatever the nature of magnetic and electrical order parameters, occurring, for example, in paramagnetic ferroelectrics[42].

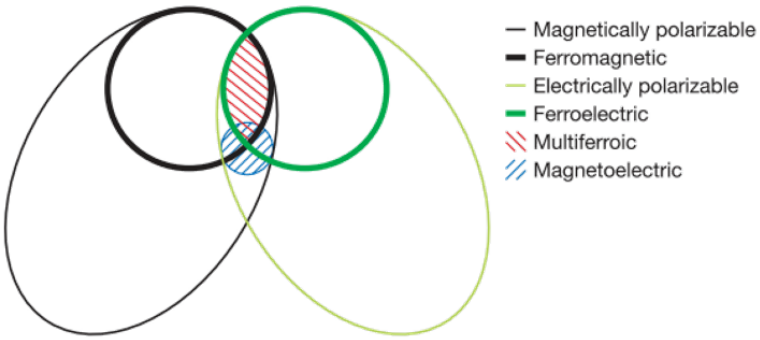

Figure 1.7 – Ferromagnets/electrics form a subset of magnetically/electrically polarizable materials such as paramagnets/electrics and antiferromagnets/electrics. Magnetoelectric coupling, in blue, is an independent phenomenon that can, but need not, appear in any of the materials that are both magnetically and electrically polarizable. In practice, it is likely to arise in all such materials, either directly or mediated via strain. (Taken from Ref. 40)

The magnetoelectric coupling can occur in two forms: if the magnetization/polarization is controlled directly by an external electric/magnetic field, that is the case of a direct magnetoelectric coupling, characteristic of single-phase multiferroic materials; if this effect is not direct, but mediated through strain[43], such as an elasto-magneto-electric effect, there is an indirect magnetoelectric effect. One path for such materials is through the synthesizing of composite materials.

Single-phase multiferroics are further classified into two types: type I and type II. This classification is mainly related to the different physical mechanisms from which electric polarization appears. **Type I** single-phase multiferroics are the materials in which the magnetic and electric phases coexist within the same compound, but have different microscopic origins and are broadly independent of each other. In **type II** single-phase multiferroics the ferroelectricity is induced by the magnetic order, which in turn suggests a very strong magnetoelectric coupling. Please consider consulting the review articles in Ref. 6 and Ref. 40 for a more detailed explanation.

Despite the interest that these materials arise, they are quite scarce. A work by

[iii] From therein abbreviated to just "multiferroic".

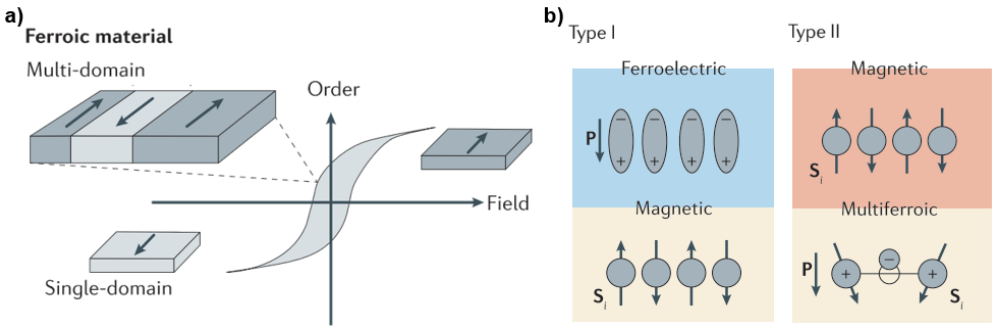

Figure 1.8 – **a)** The ferroic materials display at least one long-range order that can be switched by the same corresponding field, *e.g.* for a ferromagnetic material its magnetism is switched by an applied magnetic field. **b)** The single-phase magnetoelectric multiferroic can be further characterized into type I and type II according with the origin of its electric polarization. (Taken from Ref. 6)

Hill[41] extensively describes the conditions needed for having such multiferroic materials. The author's reason that the transition metal *d* electrons, which are essential for magnetism, reduce the tendency for off-center ferroelectric distortion. This provided a stronger ground than the former reasoning, that only a short amount of crystallographic point groups would accept a single-phase multiferroic (just 13 point groups out of 122), especially given that many candidate materials that are not, in fact, ferromagnetic and ferroelectric exist in one of the allowed symmetries. On top of that, as referenced by *Eerenstein*[40], there is still a major experimental problem about making the multiferroic samples sufficiently insulating to prevent leakage currents which contribute to the polarization signal in standard ferroelectric measurements and hinders their implementation into practical ferroelectric devices.

One approach to circumvent the lack of single-phase multiferroics operating at room-temperature and their weak magnetoelectric coupling is by the design of multiferroic composites. Here the electric, magnetic, and piezo order states are physically separated from each other, thus expanding the choices for magnetic and dielectric materials and enabling to fine-tune the magnetoelectric coupling. More recently, in 2008, *Bousquet*[24] made a key discovery for the field of multiferroic composites by artificially layering perovskites in a superlattice structure of $SrTiO_3/PbTiO_3$. In these structures, the polarization arises from the coupling of two octahedral rotational modes, behaving like an improper ferroelectric as is explained in the following section. Several other approaches are reviewed in Ref. 44 from strain engineering, lattice mode engineering or electronic spin, orbital or charge engineering.

1.2.1 Different types of ferroelectricity

Ferroelectricity (FE) was discovered in 1920 by *Valasek*[45] while studying Rochelle salts and was first observed in $BaTiO_3$ compound (a perovskite material) in 1945. Ferroelectric materials are a group of insulators characterized by having a switchable sponta-

neous polarization in which the coupling between the electric field and polarization gives rise to an electric hysteresis loop as depicted before in Fig 1.8 a). FE materials usually undergo a structural phase transition from a non-polar centrosymmetric paraelectric phase to a polar non-centrosymmetric ferroelectric phase when decreasing the temperature. However, the phase transition mechanism is different between conventional proper ferroelectricity, improper ferroelectricity, and hybrid improper ferroelectricity.

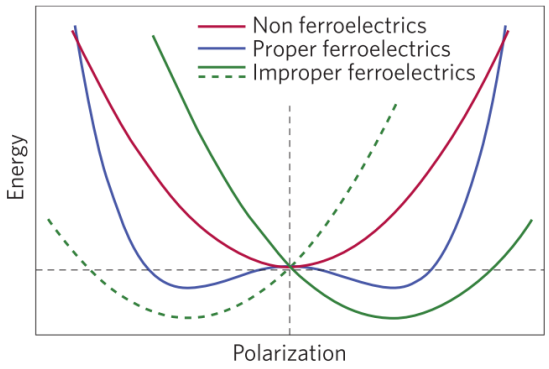

Figure 1.9 – Typical energy versus polarization curves. Non-ferroelectric compounds can be made ferroelectric either by renormalizing the energy curvature at the origin to produce a double-well as can be done via strain (red to blue curve) or by shifting the energy well through the linear coupling with primary non-polar mode(s) as it is done in (hybrid) improper ferroelectrics (red to green curve). In hybrid improper ferroelectrics, owing to a trilinear coupling term (later detailed), switching the polarization implies the reversal of one of the rotational modes (green to dashed-green curve). (Taken from Ref. 46)

In **Conventional Proper Ferroelectrics** the polarization, P, is induced directly by the condensation of unstable polar mode which acts as the primary order parameter. Here, the evolution of the energy with the polarization around $P = 0$ is characterized by a typical double-well, see blue curve in Fig. 1.9. Expanding the free energy, $\mathcal{F}$, in powers of the polarization, P (to fourth power), it is obtained the following:

$$\mathcal{F} = \mathcal{F}_0 + \alpha P^2 + \beta P^4 \tag{1.2}$$

where $\mathcal{F}_0$ is the energy of the undistorted paraelectric phase and α and β are coefficients.

When in the paraelectric phase, α is greater than zero, reflecting the force constant stability. In the opposite (ferroelectric phase), α is less than zero, thus showing the force constant instability. Here, in principle, an electric field can be used to switch the polarization between the two minima without any other structural distortions being involved. Paradigmatic examples of proper ferroelectric materials are the $BaTiO_3$ and the magnetic $BiFeO_3$. Experimentally, also some naturally layered perovskites have been found to present proper ferroelectricity such as $SrBi_2Ta_2O_9$ [47] and $CsBi_2Ti_2NbO_{10}$ [48].

In **Improper Ferroelectrics**, the ferroelectric phase transition is not driven by an unstable polar phonon mode but by another non-polar mode. Here, the polarization is no longer the primary driving force for the transition but is coupled with another mechanism

that will drive the order change, *e.g.*, structural driven improper ferroelectric in $YMnO_3$ [49] or spin-driven improper ferroelectric in $TbMnO_3$ [50]. This last has a strong coupling between magnetism and the polarization, but the polarization is too small for device applications [1].

The polarization which is coupled to another primary cooperative atomic displacement pattern R, can be written in the free energy expansion as:

$$\mathcal{F} = \mathcal{F}_0 + \alpha_{20}R^2 + \alpha_{02}P^2 + \beta_{40}R^4 + \beta_{04}P^4 + \beta_{31}R^3P + \beta_{22}R^2P^2 \tag{1.3}$$

The free energies of all typical improper ferroelectrics will contain a term linear with P (represented in the second to last term), although it may have a slightly different form [51].

The polarization well remains a single well, contrary to proper ferroelectricity (see the green curve in Fig. 1.9), hence to switch the polarization the primary distortion must also switch, $R \rightarrow -R$.

1.2.1.1 Hybrid Improper Ferroelectricity

In the **Hybrid Improper Ferroelectricity** (HIF) the energy curve in terms of polarization, P, is also a single-well as in improper ferroelectricity, see the green curve in Fig. 1.9. However, it holds two independent non-polar order parameters linearly coupled with the polarization, *e.g.* two independent rotational modes [46]. Thus, it can be described in the free energy a trilinear term, which relates P, R_1, and R_2, as:

$$\mathcal{F} = \gamma P R_1 R_2 \tag{1.4}$$

Bear in mind that even though each rotation individually could lead to a non-polar space group, *e.g.* the *Acam* symmetry group, the combined of both rotation patterns breaks all the relevant symmetries that allow a spontaneous polarization to set in, *e.g.* in $A2_1am$ [12].

Although equation 1.4 establishes the symmetry requirements of an HIF it doesn't shed light on the crystal/chemical basis of the phenomenon. However it shows a way for materials to display HIF, *i.e.* those materials would be based on structures that are formed by two different octahedral rotation patterns. Interestingly, ABO_3 perovskites have a set of non-polar structural distortions, such as tilts and rotations of the BO_6 octahedra, that can make these, and several families of layered perovskites, promising candidates in the search for HIF.

Firstly observed by *Bousquets* experimental work [24] on $PbTiO_3/SrTiO_3$ superlattices, HIFs have now been found in many other compounds, for example, the nonmagnetic phase $Ca_3Ti_2O_7$ and the low-temperature magnetically ordered phase $Ca_3Mn_2O_7$ (n = 2 RP compounds [25,26,32,52,53]), $(Ca_ySr_{1-y})_{1.15}Tb_{1.85}Fe_2O_7$ ferrite materials [54] or even $Sr_3Sn_2O_7$ ceramics [55].

Improper ferroelectricity has a great potential application for creating room-temperature

multiferroics since BO_6 octahedral perovskite layers do not compete with unfulfilled *d* orbitals of the *B* ions, which is a necessary condition for (anti) ferromagnetism[52,56]. In this way, HIF provides a mechanism to control the polarization/magnetization coupling, leading to possible strongly coupled RT multiferroicity[24]. Furthermore, with HIF it is added the possibility of coupling other lattice distortions or physical properties to the polarization, such that when the polarization is switched with an electric field, the other structural distortions or properties are also switched.

1.2.2 Polarization–magnetization coupling

Although the octahedral rotations in ABO_3 perovskites can significantly affect their magnetic properties, rotations do not directly couple to electric fields. Octahedral rotation-driven ferroelectricity in $A_3B_2O_7$ appears to solve this problem, since the distortion that induces the polarization also affects the magnetic properties. In the case of HIF materials, there are two independent rotation distortions of different symmetries that can potentially be exploited to control the magnetization.

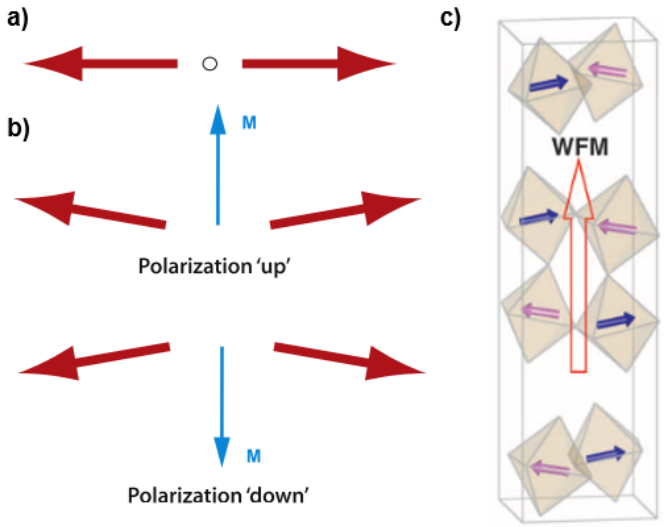

Figure 1.10 – Schematic illustration of ferroelectrically induced weak ferromagnetism through the DM interaction. **a)** In the paraelectric (P = 0) antiferromagnetic state, the spins (represented as red arrows) are related by inversion symmetry. **b)** If a ferroelectric phase transition breaks inversion symmetry, *e.g.* through a $a^-a^-c^0$ tilt, inducing in this way a magnetization (represented by a blue arrow) through spin canting. An electric field can be used to switch P and hence reverse the magnetization. **c)** The $A2_1am$ magnetic structure, with the magnetic Fe^{3+} sublattice illustrated as blue and pink arrows. (Taken from Refs. 12,54)

The RP crystal $Ca_3Mn_2O_7$ is a multiferroic with strong polar-magnetic coupling, which is both a weak ferromagnet and an HIF. The $a^0a^0c^+$ rotation induces a linear magnetoelectric effect as shown by *Benedek* and *Fennie* using a combination of symmetry arguments and first-principles calculations. The $a^-a^-c^0$ tilt induces a weak ferromagnetic response through the antisymmetric exchange, also known as the Dzyaloshinskii–

Moriya interaction[iv] (see Fig. 1.10), or crystalline anisotropy. Thus, every time that this weak ferromagnetic inducing tilt switches both the polarization and the magnetization will also switch.

1.2.3 Polarization Enhancement

The vast majority of ABO_3 perovskites are not ferroelectric, or even polar[34]. Nevertheless when observing the family of layered perovskite, described in section 1.1.1, there can be found several examples that are ferroelectric, even when the parent materials are not, *e.g.*, from the non-polar parent perovskite $CaMnO_3$ to the polar $Ca_3Mn_2O_7$.

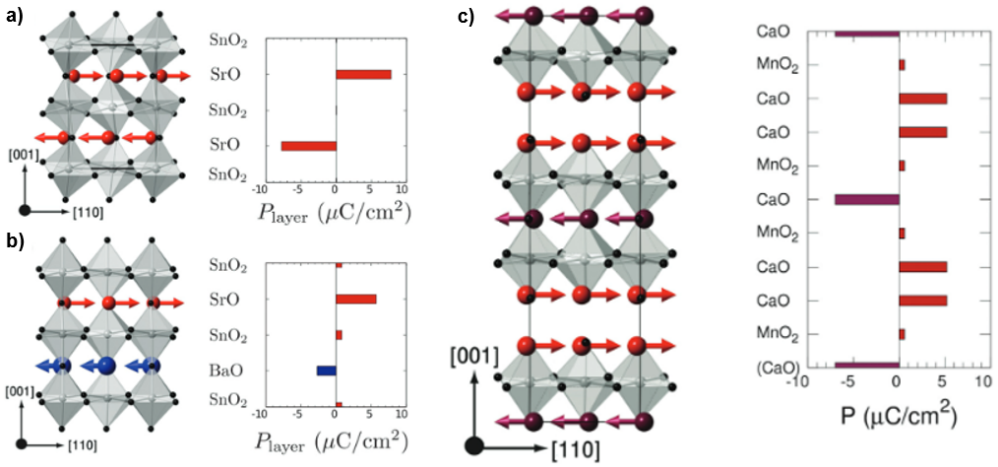

Figure 1.11 – **a)** Layer polarization of $SrSnO_3$ (in non-polar space group *Pnma*). **b)** $BaSrSn_2O_6$ double perovskite (in polar space group $Pmc2_1$). **c)** $Ca_3Mn_2O_7$ naturally layered perovskite (in polar space group $A2_1am$). The polarization values obtained from first principles calculations. The side-way projection shown puts in plain sight the analogy with the *Pnma* symmetry of the ABO_3 perovskites. (Taken from Refs. 12,35)

The structural transitions introduced in section 1.1.3 showed that in the *Pnma* symmetry there is a resulting Γ_5^-, *i.e.* a displacement of the A-site cations, see Fig. 1.4 c). This displacement induces a significant polarization within the AO layers. For example in the $SrSnO_3$ perovskite when the polarization is induced by each SrO layer, see Fig. 1.11 a), it will have the same magnitude but opposite signals, thus canceling each other out and, by consequence, the macroscopic polarization totals zero.

For naturally layered perovskites, it was shown, from first-principles calculations[12,35], that the polarization is resolved individually into AO and BO_2 layers. In the case of double perovskites the previous cancellation is incomplete and a residual polarization remains, see Fig. 1.11 b). This remaining polarization occurs also for Ruddlesden Popper materials, *e.g.* $Ca_3Mn_2O_7$. Here it is originated from the two crystallographically distinct A-sites that give rise to different layers polarization, combined with the fact that each

[iv] The spin canting of (anti)parallel aligned magnetic moments acts as a source of weak ferromagnetic behavior in an antiferromagnet.

perovskite block contains an odd number of polarized layers, see Fig. 1.11 c). Thus, it totals approximately that originating from one CaO layer. Replacing the Ca from the rock salt CaO layer (in red in Fig. 1.11 c)) with a larger ion the polarization no longer cancels with the CaO in between the perovskite layer (in purple in Fig. 1.11 c)). In this layer the polarization is strongly reduced, leading to a polarization total of approximately twice the contribution from a single CaO layer[35].

1.2.3.1 Polarization switching

Initial theoretical studies[1,35] presented a difficulty in determining whether the polarization could be switched experimentally or what the switching mechanism might be. In particular, there were concerns that the switching barrier would be extremely high. Later, *Oh et al.*[25] demonstrated that the polarization in $Ca_3Ti_2O_7$ single crystals could be switched with an applied electric field being finally experimentally confirmed by *Gao*[26] in 2017. *Nonandic et al.*[57] also presented the domain and ferroelectric switching pathways in $Ca_3Ti_2O_7$ to illustrate the reverse polarization. Here via an orthorhombic twin domain or an antipolar structure.

The switching mechanism in the case of $Ca_3Mn_2O_7$, which has more than one lattice distortion modes, is just by one of those modes, not both[1], *i.e.* starting from a fixed X_3^- tilt domain (unstrained or bulk) the switch of polarization is given by switching X_2^+; starting from a fixed X_2^+ rotation domain (compressive biaxial strain), the switch of polarization by switching X_3^- tilts.

In Ref. 35, it is found that the substitution of the A cation in between the perovskite layers increases the polarization while reducing the switching barrier in $A_3B_2O_7$ compounds.

1.3 Uniaxial Negative Thermal Expansion

The investigation into the shrinkage of solids dates as back as 1907 with *Scheel* when looking into quartz and vitreous silica at low temperatures[58]. The research continued in the '50s on lithium aluminum silicates[59,60] and later with sodium zirconate phosphate[61]. These materials can show either positive or negative volume expansion depending on composition, as the contraction is observed along only one[v] or two of the crystallographic axes. It wasn't until the 1990's that a model linking their crystal structures to such behavior was theorized by *Sleight*[62].

In framework structures, formed from strongly bonded polyhedral units, *e.g.* MnO_4 or MnO_6 octahedral units linked by corner-sharing O atoms, the negative thermal expansion (NTE) has been explained by the theory of rigid unit modes. Here, the contraction is driven by soft vibrations of approximately rigid polyhedral units, known as rigid-unit modes (RUMs)[63,64]. With increasing temperature, the amplitudes of these vibrations

[v] Also named Uniaxial Negative Thermal Expansion.

increase and all units are drawn closer together through an effect known as the tension mechanism[47].

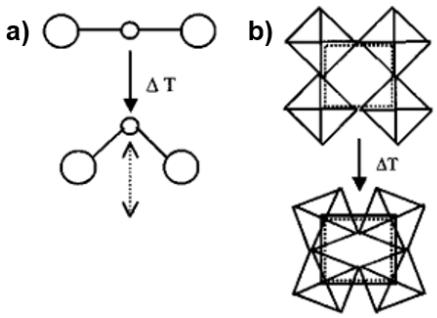

Figure 1.12 – Schematics of vibrational modes leading to NTE: **a)** Transverse vibrational motion of an oxygen atom in a M-O-M linkage causing a decrease of the metal-metal distance; **b)** cooperative rocking of polyhedra causing a decrease in average metal-metal distances. (Taken from Ref. 65)

One condition necessary for NTE is to have low energy vibrational phonon modes with large negative Grüneisen parameter[66], γ, which can be expressed as follows:

$$\gamma = V\left(\frac{dP}{dU}\right)_V = -\left(\frac{\partial \ln T}{\partial \ln V}\right)_S \tag{1.5}$$

where V is volume, U is energy, T is temperature and S is entropy. This parameter is dimensionless.

The sign of this parameter indicates whether the expansion is positive or negative, accordingly. Because the overall expansion behavior of a compound depends on the relative contributions from all phonons, not all materials with low energy phonon modes with negative γ values will necessarily exhibit NTE behavior. A feature necessary for the occurrence of NTE is the presence of low energy phonons with negative γ values, and a phonon gap that separates these modes from the high energy phonons also present in the structure[65].

Nevertheless, this description doesn't suit all materials depending, especially, on the size and rigidity of the polyhedra, here, other mechanisms also contribute to NTE behavior. For example, in Perovskite-like materials, there are the combined effects of proximity to a transition to a competing phase, named symmetry trapping, and highly anisotropic elastic compliance specific to the symmetry of the NTE phase[20,67].

The RP phases with the most pronounced NTE predicted is the $n = 1$[20]. The Ca_2GeO_4 was shown[67] to have a phase that displays pronounced uniaxial NTE over a large temperature range (100 K to 800 K).

The materials that possess NTE can also be interconnected with others having positive expansion in order to obtain a total expansion of approximately zero[65]. This property is expected to be deployed in several applications from precision instruments such as astronomical telescope mirrors, electronics in matching the thermal expansion of Si with substrates and heat sinks or the white composites in dental fillings[62,65].

CHAPTER 2

Experimental Techniques

In this chapter, an overview of the experimental techniques used in this work is presented. Starting with the sample preparation followed by structural, morphological and magnetic characterizations, giving reference to previous works where these techniques are fully explained. Ending with an overview of local probe techniques where it will be introduced the most relevant aspects of the Perturbed Angular Correlations (PAC) technique.

2.1 Sample Preparation

There is a wide range of methods for synthesizing solid-state materials, namely perovskites and its related structures, which have a direct impact on their physical and chemical properties[68,69]. Several scientific reports explore these different methods and their optimal application[7,70].

Guided by previous studies[56], several RP compounds were produced using a standard solid-state reaction method. It was observed that is a stable method to produce and stabilize RP phase structures of n = 1, 2. During the work of novel RP compounds it was also investigated the synthesis using a sol-gel combustion method. These synthesis results are still in an early stage research. The general route procedures are shown in Fig. 2.1.

2.1.1 Solid-state reaction

The solid-state reaction method consists of heating different precursors in the solid form (such as binary oxides, hydroxides, carbonates, etc.), with the appropriated stoichiometric proportions, which will react to form the required compound through ionic diffusion. In order to promote the reaction and ionic diffusion, all the reactants are finely grounded into powder form and pressed into pellets. Increasing the reaction temperature makes the diffusion occur at a faster rate, although it could lead to decomposition of the required compound. In some cases, the solid-state reaction needs to be performed in a controlled atmosphere: using inert gases (Ar, N_2) or vacuum it can prevent oxidation or limit to higher oxidation states; with O_2 flow promotes the formation of a high oxidation state and with a reducing gas, like H_2, favors the formation of a low oxidation state[71].

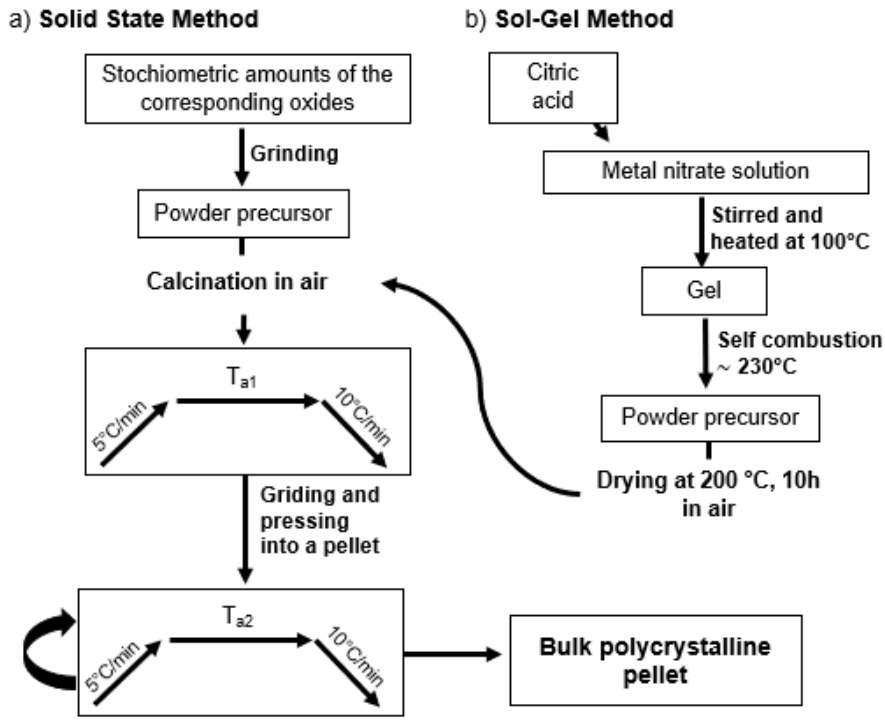

Figure 2.1 – Flowchart summarizing the procedure followed to produce the Ruddlesden Popper compounds **a)** solid-state reaction and **b)** Sol-gel combustion methods. (Adapted from Ref. 7)

Although it is a widely deployed method due to its simplicity and low manufacturing costs, attention must be paid to the precursors assuring a thoroughly grounding. Only then a complete reaction can occur and avoiding problems of homogeneity in complex solids. This procedure of grinding must be undertaken in between pelleting to bring fresh surfaces in contact, which will further promote the reaction. In order to achieve a pure sample, several high-temperature annealings may have to be performed, as shown in Fig. 2.1 a).

2.1.2 Sol-Gel

The sol-gel synthesis is a method where the sol, which is a stable suspension of colloidal solid particles within a liquid, will establish links between the solid particles to form an integrated network - a gel. If the precursor is a solution of sub-colloidal chemical units, the resulting product is called a polymeric gel. For ceramic powder production, this gel is dried and submitted to heat treatments until the desired phase or grain size is obtained.

There is a broad type of procedures and many variations to this method: from the urea sol-gel process, glycine nitrate process, sol-gel microwave combustion to solution combustion synthesis. This last, the sol–gel combustion, is where during a standard sol-gel reaction the gel is allowed to self-ignite into combustion. The self-ignition happens due to the contents on the aqueous solution, salts of the desired metals, and some organic fuel, resulting in a voluminous product with a large surface area.

One of the biggest advantages of this process in comparison with the solid-state reaction is that it allows the mixing of the different ions on an atomic level rather than being mixed by grinding. Hence requiring lower temperatures for phase formation, *i.e.* due to the shorter diffusion lengths of the precursors. For an introductory overview of this technique, please consider consulting Ref. 72.

2.1.3 Thin films deposition

There are several thin film depositing techniques such as chemical vapor deposition (CVD), molecular beam epitaxy (MBE), chemical etching (CE), pulsed laser deposition (PLD), and so on. The PLD presents several advantages such as the wide availability of materials for the target[i], its plume maintains a similar stoichiometry and by controlling the number of the laser pulses, it can be achieved a fine control of film thickness down to atomic monolayer. Given these advantages and simple experimental setup, this technique was chosen for the thin films deposited in this work.

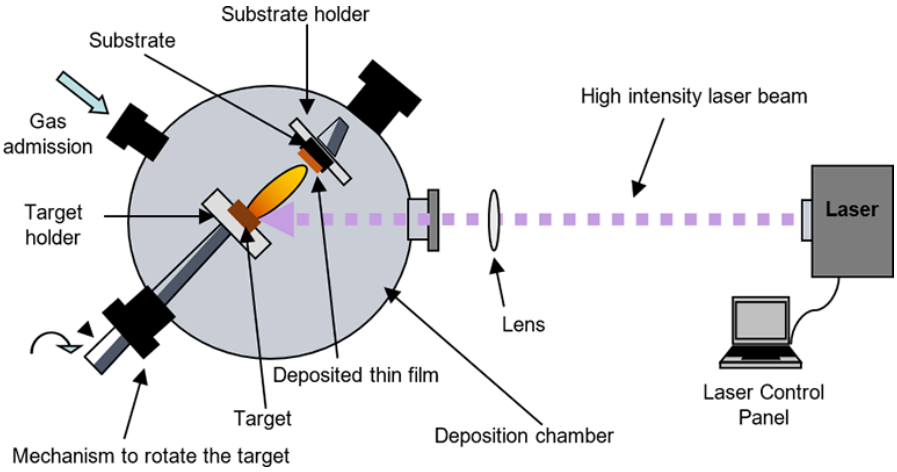

Figure 2.2 – Scheme of a regular pulsed laser deposition set up. (Taken from Ref. 73)

In the PLD experimental setup, there is a target (having the final film stoichiometry) and a substrate where the plume will deposit the material. Both have to be placed parallel in the deposition chamber. The efficiency of the technique is dependent on the presence of a dispersive medium within the chamber, so the vacuum is essential for a good deposition. A high-intensity laser placed outside the deposition chamber is used as an energy source to ablate the target material and to deposit the material. Since the target vaporization is induced by photons, there is no contamination/impurities occurring during the deposition process. A multitude of materials is suitable to be used as a target from metals, ceramics or even temperature resistant organics. As for drawbacks, it can be point out that for large-scale film growth it has an uneven coverage.

[i] The material that is irradiated by the laser beam.

For more information on the factors that influence the laser ablation technique efficiency, please consider consulting the succinct chapter ”Laser Ablation Applied for Synthesis of Thin Films: Insights into Laser Deposition Methods” in Ref. 73.

In some cases, it is possible to obtain a film that has a specific composition different from the targets one. This is achieved by the introduction of a flow of reactive gas in the chamber, this is called reactive pulsed laser deposition (RPLD).

2.1.3.1 Experimental Details

All depositions were performed at the University of Minho, in the Braga facilities. The experimental setup was composed of a Lambda Physic LPXpro 210 pulsed excimer KrF laser with a wavelength of 248 nm and a pulse duration of 20 ns. The energy per pulse can go to a maximum of 800 mJ and the pulse repetition rate can reach 100 Hz. At the output, the laser beam cross section is 10x24 mm^2. The beam is focused on the sample with a set of optical lenses and mirrors.

2.2 Structural and Morphological Characterization

For the structural characterization of materials there are plenty of suitable techniques, within the diffraction, it can be chosen from x-rays, photons, electrons, and neutrons. These are the most suitable since they have a wavelength on the same order as the typical lattice parameters in crystalline solids, a few angstrons (Å). Hence, it is possible to form a constructive and destructive diffraction pattern from the iteration of the particles with the lattice.

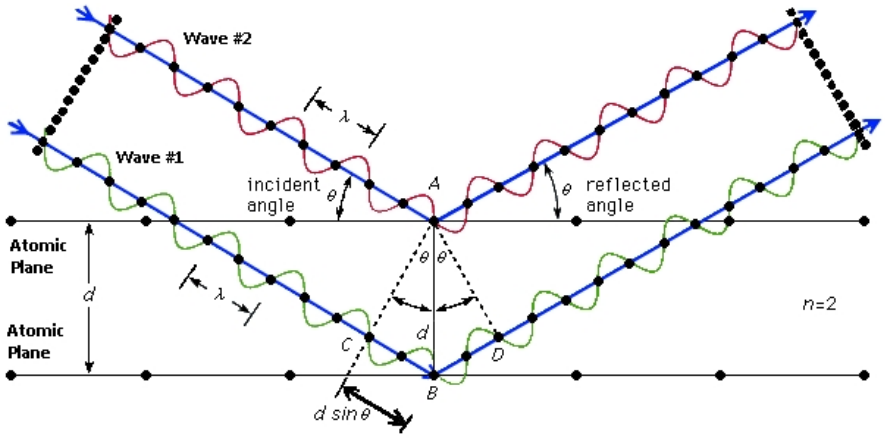

Figure 2.3 – Constructive interference upon diffraction at two subsequent crystallographic planes.

For an elastic scattering, the maximum intensity it will correspond to the constructive interference, i.e., the scattering directions that result from the addition of the incident particle moment and any vector belonging to the reciprocal lattice of the crystal, typically

associated with a set of Miller indices[ii]. These directions are called Bragg positions or Bragg peaks and obey the Bragg's law:

$$\lambda = 2d_{hkl} \sin\theta \quad , \tag{2.1}$$

where λ is the wavelength of the incident wave, d_{hkl}[iii] is the distance between planes in Miller notation, and that θ is the angle formed by the crystallographic plane and the momentum of the incident wave, see Fig. 2.3.

The diffraction experiments give us an insight into the reciprocal lattice, and therefore the lattice in the real space can be obtained as the Fourier transform of the reciprocal space. A crystal consists of many sets of planes and these planes are characterized by interplannar distances d_{hkl}, which are a function of the size and the shape of the unit cell. Other factors including atomic numbers and the position of the atoms in the unit cell, influence the powder pattern. In other words, a powder pattern has two characteristic features, the d spacings of the lines and their intensities.

A unit cell contains some specific atoms, j, with scattering factors, f_j, and coordinates, x_j, y_j and z_j, the amplitude of a wave diffracted by an hkl plane set is given by the structure factor F_{hkl}:

$$F_{hkl} = \sum_i f_j \left[\cos\left(2\pi\left(hx_j + ky_j + lz_j\right)\right) + i\sin\left(2\pi\left(hx_j + ky_j + lz_j\right)\right)\right] \quad . \tag{2.2}$$

The intensities of a pattern peak are proportional to the square of F_{hkl} and also related mainly to variations of electron and atomic scattering, interference effects, anomalous scattering and thermal motion of atoms. The intensity scattered by electrons is given by:

$$I(\theta) = n\frac{I_0}{R^2}\left[\frac{e^2}{m_e c^2}\right]^2 \frac{1+\cos^2(2\theta)}{2} \quad , \tag{2.3}$$

where, n is the number of electrons of an atom, I_0 is the intensity of the incident beam; e is the electron charge; m_e is the mass of the electron; c is the light speed and R is the distance from the scattering electron to the detector.

2.2.1 X-Ray Diffraction

X-ray diffraction (XRD) is one of the most important non-destructive tools to analyze all kinds of matter ranging from fluids to powders and crystals. It is easily found in research units as in industrial facilities for materials characterization and quality control. It will follow a brief approach to the most important issues for the present work. Nevertheless, for a more detailed explanation, please consider consulting the works of *Dinnebier*[74] and *Pecharsky*[75].

[ii] A notation system in crystallography for planes in crystal (Bravais) lattices.
[iii] $d_{hkl} = \frac{d}{n}$, where d is the distance between atomic planes and n is the diffraction order.

As discussed above, the diffraction will occur when the structural periodicities in a crystal are in the order of magnitude of the radiation wavelength which will produce a unique ”x-ray fingerprint”. As *Albert W. Hull* puts it: ”every crystalline substance gives a pattern; the same substance always gives the same pattern, and in a mixture of substances each produces its pattern independently of the others”[76].

To produce x-ray radiation, a beam of electrons is accelerated by an electric field and directed against a metal target, usually copper metal. These accelerated electrons can eject the electrons from the inner shells of the target atoms. Those vacancies will be quickly filled by higher level electrons leading to the characteristic x-ray emission of the target. When the electrons drop down from the $n = 2$ or the $n = 3$ level to fill the gap vacancies that are produced in the $n = 1$ level - K-shell - of the target atom they are called K_α or K_β, accordingly. To make the beam monochromatic it is used a Ni filter that selectively removes the K_β, with a relatively much smaller loss of K_α.

When an x-ray beam hits an atom, electrons around an atom start to oscillate with the same frequency as the incident beam. Destructive interference would occur in almost all directions while the constructive interference will only occur in crystals at a few directions.

The for the x-ray optics there are at least two main setups: Bragg Brentano (BB) and Parallel Beam (PB) reflection geometry, as is illustrated schematically in Figure 2.4.

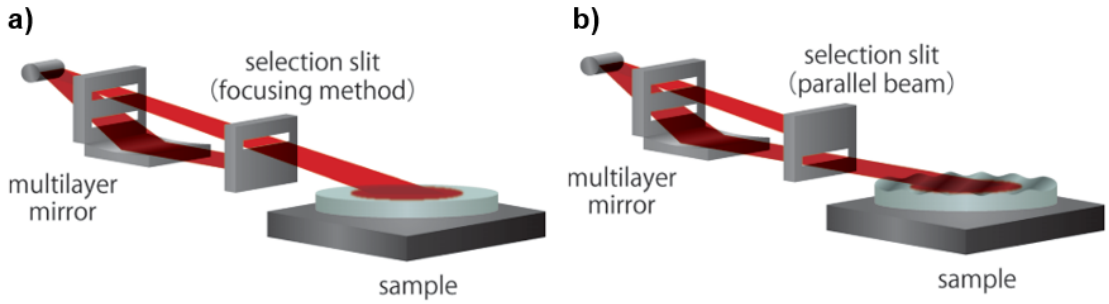

Figure 2.4 – Schematic representation of **a)** the Bragg Brentano and **b)** the Parallel Beam geometry in x-ray diffraction. (Taken from Ref. 77)

Bragg Brentano (BB) reflection geometry has the divergent and diffracted beams are focused at a fixed radius from the sample position. In the simplest setup of this method, the anode can be fixed and the sample and the detector can be rotated by θ and 2θ, respectively. A common alternative is to fix the sample, usually in the horizontal position, and to move both the source and the detector by $-\theta$ and θ. It enables easy acquisition of high resolution and high-intensity data and it is generally used for qualitative and quantitative analysis of powder samples.

Parallel Beam (PB) reflection geometry has a parabolic multilayer mirror that serves as a collimator of the incident beam, thus reaching the sample in a parallel way. It allows accurate measurement of diffracted x-ray positions unaffected by sample shape. Usually, it is used to analyze powder sample profiles and measure the degree of preferred

orientation, as well as to measure thin-film samples. Here, to assure a low penetration the incident beam is put in a grazing incidence angle (ω).

With the diffraction pattern, it is possible to compare it directly with other known powder diffraction patterns of the same sample or chemically different phases. X-ray diffraction patterns are most often used for qualitative phase identification, however, if the sample is unknown, refining the data it can be used to determine the structure, as discussed in the following subsection.

2.2.1.1 Data refinement

In order to extract accurate crystallographic quantitative information from neutron and x-ray diffraction patterns, the data must be refined using, for example, the Rietveld or Le Bail refinement.

The **Le Bail refinement** method is a whole pattern fitting method that extracts the peak positions to find out which are suitable with the allowed reflections of crystalline symmetry. For this method, it is needed to provide a unit cell and the space group of the sample since they are included as a part of the fitting technique. Then the method goes through an iterative process using the steepest descent minimization. In overlapping peaks, it performs a profile intensity partitioning to extract each peak intensities. The algorithm involves refining the unit cell, the peak shape parameters, and the peak intensities to match the observed powder diffraction pattern. This method is very useful for comparing different space groups fits, especially in the cases that have peak overlaps that can't be told by eye.

The **Rietveld method**[78] is a refinement technique that uses a non-linear least square process to fit a set of observed peaks with the ones calculated from a crystal model. For this method, the input data includes the space group, atomic positions, site occupancies, and lattice parameters. Here, it will not only match intensities but also the profile at each peak using a profile function (*e.g.*, the Voigt, the pseudo-Voigt or even the split Pearson VII among others). The Voigt function is the combination of an analytical convolution of a Gaussian and a Lorentzian, where it includes the extremes of being pure Lorentzian to Gaussian. The pseudo-Voigt conveniently allows the refinement of a mixing parameter determining the fraction of Lorentzian and Gaussian components needed to fit an observed peak. The algorithm can provide acute quantitative information including crystal structure information such as lattice parameters, atomic coordinates, displacement factors, site fractions and macroscopic information such as crystallite size and microstrain distribution.

2.2.1.2 Experimental Details

The x-ray diffraction measurements were performed at the IFIMUP facilities. For this purpose, a Rigaku with Cu Kα radiation (λ = 1.541 Å), primary and secondary monochromators and automatic slits were used. For this work, the diffractograms were obtained

in a $10 < 2\theta < 90$ range and, depending on the desired precision of the measurement, the 2θ steps ranged between 0.01 and 0.03.

For the structure analysis, it was used the software Fullprof[79] that is able to perform Le Bail and Rietveld refinements. As for refinement guide, it was used the one reported in Ref. 80.

2.2.2 Scanning Electron Microscopy

The electronic microscopes are instruments that allow the observation and characterization of materials solely studying the resulting radiation of that material with an electron beam. Adjusting the incident beam it is possible to use different techniques of electron microscopy that characterize physically, chemically and structurally the material from the micrometer (μm) to the nanometer (nm) scale. There is a wide range of materials capable to be studied, *e.g.* metals, ceramics, polymers, composites, and biomaterials.

Depending on the volume of interaction within the material there are different signals obtained: secondary electrons, backscattered electrons, characteristic x-rays and other photons of various energies (see Fig. 2.5 a)). For topography imaging, the signals of greatest interest are the secondary electrons because these have a direct correspondence with the morphology of the sample surface. The secondary electron emission, confined to a tiny volume near the surface where the electron beam first impacts, permits images to be obtained at a resolution of the same magnitude order of the focused electron beam size. The backscattered electrons give an image contrast that is sensitive to the distribution of the atomic number of the chemical elements all there.

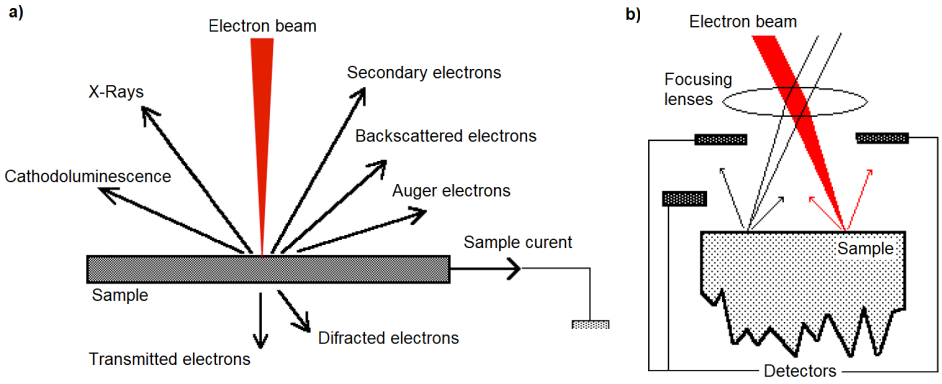

Figure 2.5 – Schematic representation of: a) radiation emitted by the sample due the interaction between the incident beam of electrons and a sample, b) a standard set up for SEM. (Adapted from Ref. 81)

There are three main setups for electron microscopy: transmission electron microscopy (TEM), scanning electron microscopy (SEM) and a combination of both (STEM). The main advantages using one of these techniques are the possibility to study large samples, up to a few cms, with almost no preparation steps, a topographical high reso-

lution, even with a big magnification, and the access to a large set of information on the sample local characteristics.

In a scanning electron microscopy (SEM) setup (see Fig. 2.5 b)) the sample surface is swept by a focused beam of electrons. The brightness of each point in the obtained image corresponds to the combined intensity of the radiations emitted from the sample. In a conventional setup, samples can be thick, up to a few cms, as long as they can keep, or won't suffer degradation, in high vacuum conditions (about 10^{-4} Pa) and are electrically conductive on its surface. With specialized instruments it is possible to use a low vacuum ($p > 10^2$ Pa) or wet conditions in a variable pressure or environmental SEM ($p > 10^3$ Pa).

Usually coupled with a SEM there is an energy dispersive x-ray spectrometer (EDS) for the chemical characterization of a sample. This instrument makes use of the characteristic x-ray radiation emitted from the sample allowing a piece of qualitative elemental information with a spatial resolution of μm, see Section 2.2.1.

For a more detailed description and explanation of different setups as well as measurement principles please consider consulting Ref. 82.

2.2.2.1 Experimental Details

The SEM measurements presented in this work were performed at the Materials Centre of the University of Porto (CEMUP) with an FEI Quanta 400FEG ESEM/EDAX X4M equipped with an EDS. The samples were mounted into the SEM sample holder with carbon tape.

2.3 Magnetic Characterization

The magnetic susceptibility, χ, is a dimensionless proportionality constant that indicates the degree of magnetization M of a material response when placed in an external magnetic field:

$$\chi = \frac{M}{H} \quad , \tag{2.4}$$

Materials can be magnetically classified by the response to an externally applied magnetic field. Diamagnetism, $-1 < \chi < 0$, is a weak property of all materials and opposes the H. Paramagnetism, $0 < \chi \ll 1$, larger than diamagnetism, exhibits proportional magnetization in the same direction of the H. Moreover, the ferromagnetic, $\chi \gg 1$, or antiferromagnetic, can lose its order into a paramagnetic state above to what is called Curie temperature, T_C, or Néel temperature, T_N, in the latter case.

Moreover, the ferromagnetic materials have a spontaneous magnetization that can be lost in an order-disorder transition, in this case, into a paramagnetic one. That transition occurs at the Curie temperature, T_C. Above this point, in the paramagnetic region,

the magnetic susceptibility, χ, can be described by the Curie-Weiss law:

$$\chi = \frac{C_{Curie}}{T - T_C} , \tag{2.5}$$

where T is the absolute temperature in Kelvin and C_{Curie} is a material specific constant, named Curie constant. This constant is given by:

$$C_{Curie} = \frac{n\mu_0 g_j^2 J(J+1)}{3k_B} , \tag{2.6}$$

where μ_0 is the effective paramagnetic moment, J the angular momentum quantum number[iv]. The constant g_j is known as the Landé g-factor and can be written as:

$$g_j = \frac{3}{2} + \frac{S(S+1) - L(L+1)}{2J(J+1)} . \tag{2.7}$$

The expression (2.5) holds for low magnetic fields and can be rewritten as:

$$\chi_m \cong \frac{\mu_0 M}{B} = \frac{\mu_0 N_A \mu_{eff}^2 \mu_B^2}{3k_B T} . \tag{2.8}$$

To measure the magnetic susceptibility and other related properties, different methods can be applied[83]. The one used in this work was the SQUID which has a short description in the following subsection.

2.3.1 Superconducting Quantum Interference Device

Superconducting Quantum Interference Device (SQUID) is an apparatus that measures extremely small magnetic fields produced by a magnetized sample. It is based on flux quantization with superconducting loops containing Josephson junctions. The flux is quantified in units of $\phi_0 = \frac{2\pi\hbar}{2e} \approxeq 2.0678 \times 10^{-15}$ T $\cdot$ m^2. A Josephson junction is defined by having two superconductors separated by a thin insulating layer where Cooper pairs of electrons can experience tunneling. These junctions can be designed to switch in times of a few picoseconds and are extremely sensitive, up to 5×10^{-18} T[84].

There are two types of SQUIDs one that uses direct current (DC) and it's made up of two Josephson junctions and another that uses radio frequency (RF) and is made up of one Josephson junction.

In the DC SQUID, when it is not perturbed by an external magnetic field, an input current, I, is split equally into the two branches of the superconductor (see Fig. 2.6 a)). This current must be under a critical current, I_C, otherwise the SQUID will operate in a resistive mode. If an external magnetic field is applied, a screening current, I_S, appears which will have a different direction relative to each one of the superconductive branches. Given the quantization of magnetic flux, ϕ_0, the I_S will flow favorable or op-

[iv] Defined as $J = L + S$

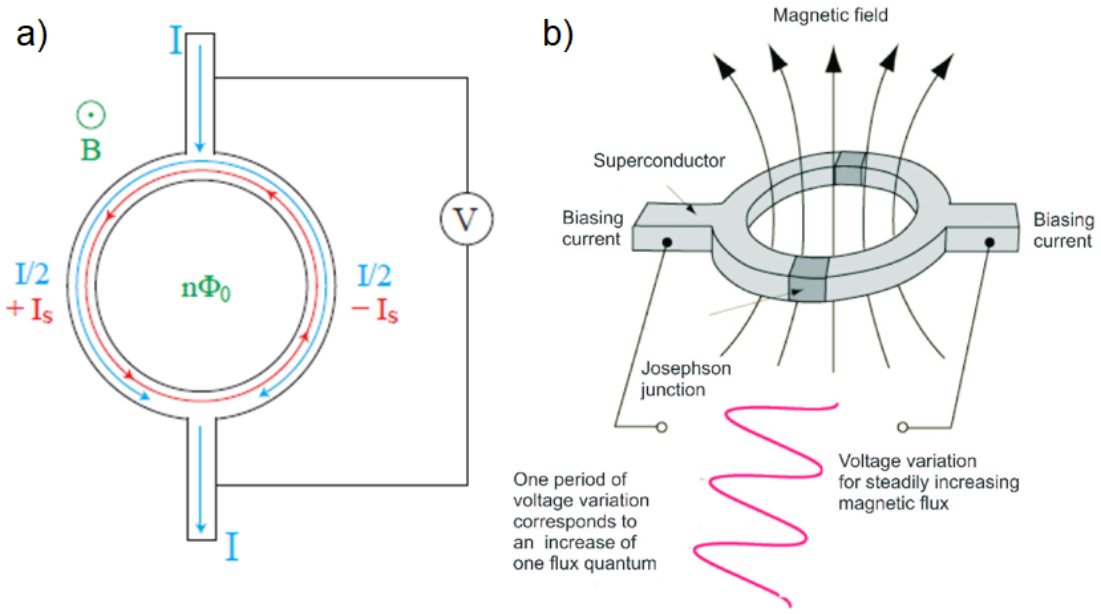

Figure 2.6 – Diagram of a DC SQUID showing the two Josephson junctions in a superconducting ring.

posing *I*. When the external field is increased the current decreases, is zero when the flux is exactly ϕ_0 and again reverses direction as the external field is further increased (see Fig. 2.6 b)). The measured voltage is, thus, a function of the applied magnetic field and the period equal to ϕ_0.

In the RF SQUIDs, there is only one Josephson junction that is inductively coupled to a resonant tank circuit. When an external magnetic field is applied the effective inductance of the tank circuit changes, hence changing the resonant frequency of the tank circuit. These frequencies can be easily measured, and the losses which appear as the voltage across the load resistor in the circuit are a periodic function of the applied magnetic flux with a period of ϕ_0. The external magnetic field is what limits the resistive mode of the RF SQUID. Although the RF SQUID is more common, due to its simplistic construction, however, the DC SQUIDs are more sensitive.

2.3.1.1 Experimental Details

All of the magnetization measurements showed in this thesis were performed at the IFIMUP facilities in a SQUID magnetometer. The device used was a Quantum Design Ref: MPMS-5S. It has a 10^{-7} emu resolution and can perform measurements with magnetic fields up to 5.5 T in the temperature range of 4 to 380 K. The samples were placed inside of cotton filled capsules within plastic straws. The use of the plastic straw allows correct placement of the sample, centering it correctly between the superconducting coils.

For the study of magnetization in terms of the thermal dependence, it was met the

low field magnetization criteria, expressed in equation (2.5), applying around 200 Oe. Two types of measurements: Zero Field Cooling (ZFC) and Field Cooling (FC) were performed. The ZFC mode is when, after the sample is cooled at $H = 0$ to the lowest temperature, the measurements of magnetization are performed with an applied magnetic field whilst sweeping up the temperature in a variable range of temperatures. The FC mode is when the sample is cooled down to the desired temperature under an applied field. The measurement is then performed, with the constant applied field, while heating the sample in the same range of temperatures. To fathom hysteresis, for example, it is interesting to perform both measurements while heating and cooling[v].

Curves of magnetization as a function of an applied magnetic field, $M(H)$, were also obtained in order to evaluate the coercive field, H_c and saturation magnetization, M_s. In these cases, measurements were performed while decreasing the applied field from 5 to 0 Tesla at a stabilized temperature.

2.4 Local Probe Techniques

2.4.1 Nuclear methods for condensed matter physics

The interactions between the electric/magnetic nuclear moments and extra nuclear electromagnetic fields are defined as nuclear hyperfine interactions. Here, the electromagnetic fields interact with the nuclear moments leading to a rearrangement in the nuclear level structure. Therefore, the measurement of these interactions offers a precise tool to investigate condensed matter phenomena proving direct information of the local charge distribution and magnetic hyperfine fields, thus called local probe techniques. The compounds here studied hold very distinct macroscopic properties which in most cases have an origin in subtle differences in microscopic phenomena. Hence, it becomes clear of the great importance of the use of nuclear hyperfine methods for studying these solid-state systems.

Nuclear experimental methods usually involve either the detection of particles (electrons, protons, neutrons, α-particles, etc.), γ-radiation from nuclear decays or nuclear reactions. The methods that use a radioactive probe/source for the particle/radiation detection are the Mössbauer spectroscopy[85] (MES), β-NMR[86] or Perturbed Angular Correlation[87] (PAC). Other techniques that don't use a radioactive probe are nuclear magnetic resonance (NMR) and nuclear quadrupole resonance spectroscopies (NQR).

In the radioactive decay methods information is collected through the electric and magnetic hyperfine interaction, *i.e.* the interaction between the nuclear moments of a specific radioactive nuclei and the magnetic and/or electric fields induced by the surroundings (valence electrons, conduction electrons, neighbor atoms, neighboring defects or distortions) emitting, then, this information via their radioactive decay. Since

[v] In this work it was taken the nomenclature of FCC and FCH for an FC measurement that was performed while cooling or heating, accordingly.

these techniques have a small probing volume with a high sensitivity associated, thus working at the atomic scale, they possess many advantages for studying structural, electronic and dynamical properties of the host atom, single impurities, and impurity-defect complexes. In highly correlated materials the information obtained by these techniques is even more important given that the intrinsic disorder requires real lattice atomic scale studies.

Since the general theory of Perturbed Angular Correlations is mathematically complex and has been well explained in several textbooks[88] and previous thesis[89–91], here only the basic physics and phenomenology of this nuclear technique will be introduced.

2.4.2 Perturbed Angular Correlation Technique

PAC[vi] technique is based on the time differential angular correlation between pairs of gamma-rays emitted from internal decay of a radioactive nuclei, see Fig. 2.7 a) (or a pair electron-gamma in the case of electron-gamma cascade). This angular correlation originates from the gamma-rays that are emitted anisotropically from the probe nucleus, otherwise, if the nucleus spins are randomly oriented the radiation is emitted isotropically. In order to obtain an anisotropic angular distribution, the state from which the second gamma-ray is emitted is at least partly polarized or aligned. This unbalance in sub-level population comes from the lifetime, τ_N, of the intermediate state after the first gamma-ray is emitted.

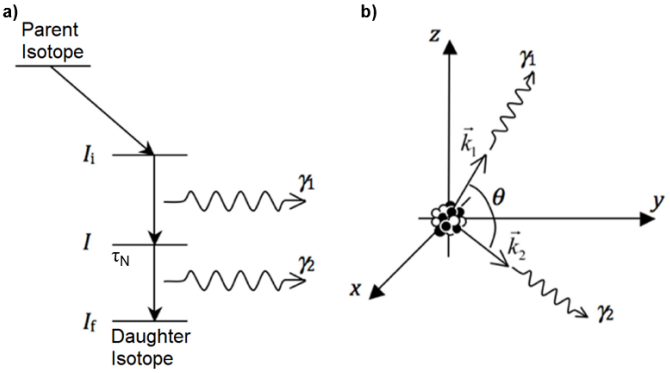

Figure 2.7 – **a)** A gamma-gamma nuclear cascade. **b)** The probe atom is placed inside the material under research and emits radiation in cascade, which is detected by scintillators. (Taken from Ref. 92)

Observing a γ_1 sets a fixed direction, $\vec{k}_1$, to where the population of the m sub-levels in the intermediate state is unequally distributed. Taking profit from the existence of an extra nuclear electric field gradient (EFG) and/or magnetic field, which sets the hyperfine interaction, the PAC spectra shows the resulting angular dependence (see

[vi] Throughout this work "PAC" will be used as a synonymous for TDPAC, which is used to emphasize that the method is Time Differential PAC as opposed to time Integrated PAC, also denoted as IPAC.

Fig. 2.8). Thus, it is possible to define the probability, $W(\theta)$, of finding γ_2 from a certain direction, $\vec{k}_2$, at an angle θ with respect to $\vec{k}_1$ and in coincidence with γ_1 as:

$$W\left(\vec{k}_1, \vec{k}_2\right) = W(\theta) = \sum_{k=0}^{k=k_{max}} A_k(\gamma_1) A_k(\gamma_2) P_k(\cos(\theta)) \tag{2.9}$$

The sum is finite, due to conservation of angular momentum[92], and runs over for even values of k as a result of parity conservation of the electromagnetic radiation. It is usual to consider $k_{max} = 4$ because the contributions from higher values of k are negligible. $A_k(\gamma_1)$ and $A_k(\gamma_2)$ are the anisotropy terms and describe the deviation of the coincidence probability from the isotropic case ($W(\theta) = 1$). Lastly, $P_k(x)$ are the Legendre polynomials[vii] and reflects the spacial angular distributions of the emitted particles. The angular correlation can be measured experimentally using the set up presented in Fig. 2.8 a).

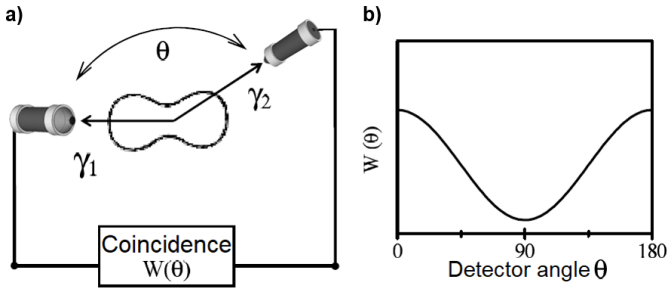

Figure 2.8 – **a)** Experimental setup to measure the angular correlation in a gamma-gamma decay with a sweeping angle of θ. **b)** The resulting graph of $W(\theta)$. (Taken from Ref. 89)

2.4.2.1 Perturbed Angular Correlation

When a nucleus is surrounded by other atoms interactions will occur. These interactions can be due to the fields created by the atomic vicinity. In the presence of external fields, interaction with the nucleus magnetic or/and quadrupole moments appears. Hence a torque on the angular momentum of the intermediate state may appear, which leads the population of the m sub-levels to be reordered.

In polycrystaline materials, the perturbed angular correlation function is obtained by averaging the angular correlation over all possible orientations of the EFG/MHF fields and only the relative angle between the two emission directions is considered. Therefore, for the case of axially symmetric quadrupole interactions, $W(\theta)$ can be expressed as:

$$W(\theta, t) = \sum_{k=0}^{k=k_{max}} A_k(\gamma_1) A_k(\gamma_2) G_{kk}(t) P_k(\cos(\theta)) \tag{2.10}$$

[vii] A Legendre polynomial of degreee n is given by $P_n(x) = \frac{1}{2^n n!} \frac{d^n}{dx^n}[(x^2 - 1)^n]$.

where $G_{kk}(t)$ is the perturbation factor containing all the information on the energy splitting of the sub levels of the intermediate state. It can be written as a sum of cosines with a different set of amplitudes which do not depend on the orientation of hyperfine interactions relative to detector directions:

$$G_{kk} = \sum_{n=0}^{n_{max}} S_{kn} \cos(n\omega_0 t) \tag{2.11}$$

where S_{kn} are the frequency amplitudes, $n = \frac{m^2 - m'^2}{2}$ (for I half integer) and $n = |m^2 - m'^2|$ (for I integer[viii]).

To determine this perturbation factor, $G_{kk}(t)$, it is needed to count the coincidences, N, as a function of time between the emission of the two gammas at a fixed detector angle, $N(\theta, t)$. A count is measured by the means of a clock that is started when a first gamma, γ_1, with a certain energy is detected, and stopped after a certain period when a second gamma, γ_2, of the same energy, is detected in one of the other detectors, see Fig. 2.9.

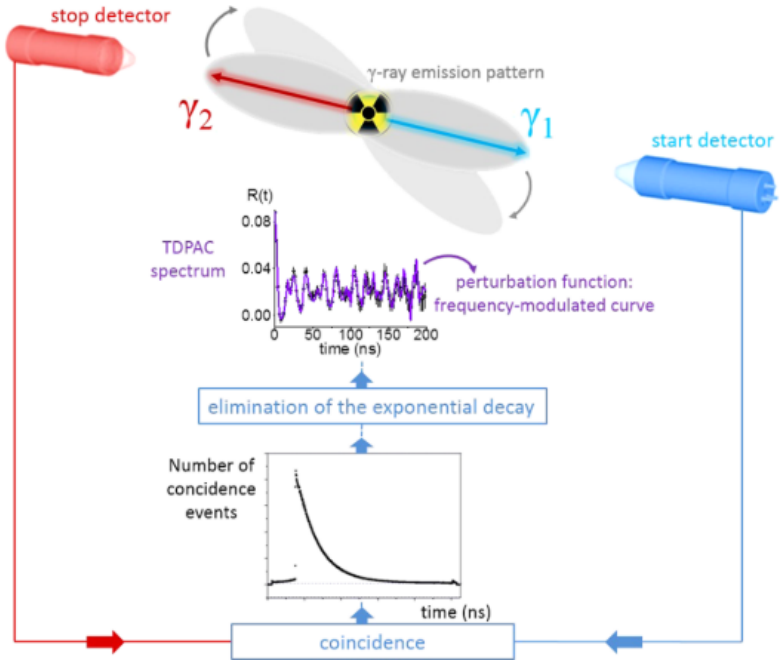

Figure 2.9 – Scheme of the PAC technique: detection and coincidence of the rotating emission gamma-cascade pattern, elimination of the exponential decay and generation of frequency-modulated PAC curve of the intermediate state. (Taken from Ref. 93)

The experimental setup typically have 6 or 4 gamma-detectors usually of BaF_2 or $LaBr_3$. In the 6-detector setup there will be 6 combinations of $\gamma_1 - \gamma_2$ coincidence time spectra from detectors positioned at $\theta = 180°$and 24 combinations from the detectors

[viii] m and m' are the projected spin angular momentum quantum numbers of the initial and final state of the probe

pairs at θ = 90°resulting in 30 spectra which are being simultaneously recorded, see Fig. 2.11 c). In the 4-detector setup there will be only 4 combinations from the detectors positioned at θ = 180°and 8 from the detector pairs at θ = 90°, resulting in 12 spectra recorded. All these resulting spectra are combined to build the $R(t)$ anisotropy ratio function [94].

2.4.2.2 Anisotropy ratio function R(t)

The anisotropy function, $R(t)$, is the observable that contains all the information regarding the coupling of the nuclear moments with the hyperfine magnetic field and electric field gradient and is expressed as:

$$R(t) = 2\frac{N(180\,\mathrm{deg}, t) - N(90\,\mathrm{deg}, t)}{N(180\,\mathrm{deg}, t) + 2N(90\,\mathrm{deg}, t)} \tag{2.12}$$

Eq. 2.12 is fitted by a theoretical function using specific software. Generally, the experimental results can be compared with results obtained using first principles methods that are based on Density Functional Theory (DFT) or the point charge model (PCM).

For the case of a static axial symmetric electric quadrupole interaction in polycrystalline sample the experimental perturbation function, described in Eq. 2.12, relates with the perturbation factor, $G_{kk}(t)$ in:

$$R(t) = A_{kk} \sum_{n=1}^{n_{max}} f_n G'_{kk}(t) \tag{2.13}$$

where f represent the relative fractions for different EFG's contributing to the PAC spectrum and $G'_{kk}(t)$ the corresponding perturbation factor after taking into account the finite time resolution of the PAC setup. Therefore, the $G_{kk}(t)$ is modified multiplying each term in the sum by $P(F*_{whm}, \omega_n)$[ix]. A second term, $D(F_{whm}, t)$[x], is also multiplied to account for possible EFG distributions. The perturbation factor is then written as:

$$G'_{kk} = \sum_n s_{kn} \cos(\omega_n t) D(F_{whm}, t) P(F*_{whm}, \omega_n) \tag{2.14}$$

2.4.2.3 Electric Field Gradient

Using the PAC technique the EFG around the nuclear probe on a lattice site can be asserted. The EFG tensor, V_{ij}, is a traceless matrix, so it can then be completely described by only two of its components. By an appropriate choice of the eigenvector basis, the eigenvalues are arranged in such a way that:

$$|V_{zz}| \geq |V_{yy}| \geq |V_{xx}| \tag{2.15}$$

[ix] Defined as $P(F*_{whm}, \omega_n) = e^{-\frac{F*_{whm}^2}{16\ln 2}\omega_n^2} = e^{-\frac{1}{2}\tau_{setup}^2\omega_n^2}$

[x] Defined as $D_{Lorentz}(F_{whm}, t) = e^{-\frac{F_{whm}}{2}t}$

Therefore, the EFG is commonly described by its largest component, V_{zz}, and the so called asymmetry parameter η, defined as:

$$\eta = \frac{V_{zz} - V_{yy}}{V_{xx}} \tag{2.16}$$

The asymmetry parameter takes values between 0 and 1 and measures the deviation of the local charge distribution from axial symmetry ($\eta = 0$). The quadrupole frequency is defined as:

$$\omega_Q = \frac{eQV_{zz}}{4I(2I-1)\hbar} \tag{2.17}$$

and gives the energy scale for the nuclear quadrupole interaction. For the particular case of an axially symmetric interaction ($\eta = 0$), the eigenvalues of the hamiltonian are:

$$E_Q = \hbar\omega_Q[3m^2 - I(I+1)] \tag{2.18}$$

The transition energy between two sublevels m and m' is given by:

$$\Delta E_Q = \hbar\omega_Q|m^2 - m_2'| \tag{2.19}$$

where $|m^2 - m_2'|$ is always integer so all transition frequencies are multiples of ω_Q and the fundamental observable frequency, ω_0, the lowest transition frequency is either $6\omega_Q$ for I half-integer or $3\omega_Q$ for I integer.

The EFG strength is represented by the quadrupole frequency constant, ν_Q, defined by:

$$\nu_Q = \frac{eQV_{zz}}{h} = \omega_0 \frac{4I(2I-1)}{2\pi k} \tag{2.20}$$

where $k = 3$ (for I integer) or $k = 6$ (I half-integer).

On the other hand, the magnetic dipolar energy, E_m can be introduced from a classical description and the following expression be obtained:

$$E_m = -\vec{\mu}\vec{B} \tag{2.21}$$

where μ and B are the nuclear magnetic moment and B the magnetic hyperfine field, correspondingly. The splitting between two adjacent sub-levels is:

$$\Delta E_m = \hbar\omega_L \tag{2.22}$$

where $\omega_L = \lambda B$ is the Larmor frequency and γ is the gyromagnetic ratio. When both magnetic and electric interactions are present the hamiltonian for such combined static interactions, in the proper reference frame of the EFG tensor, cannot be diagonalized analytically and its eigenvalues and eigenvectors must be calculated numerically.

The electric quadrupole splitting of nucleus angular momentum by an axially sym-

metric EFG and evolution of the splitting as the EFG loses the axial symmetry. In the case of ^{111}Cd the intermediate level is characterized by nuclear spin momentum of I=5/2. The quadrupole interaction splits this level into three sub-levels described as a frequency triplet: ω_1, ω_2 and ω_3, where $\omega_3=\omega_1+\omega_2$, see Fig. 2.10 b).

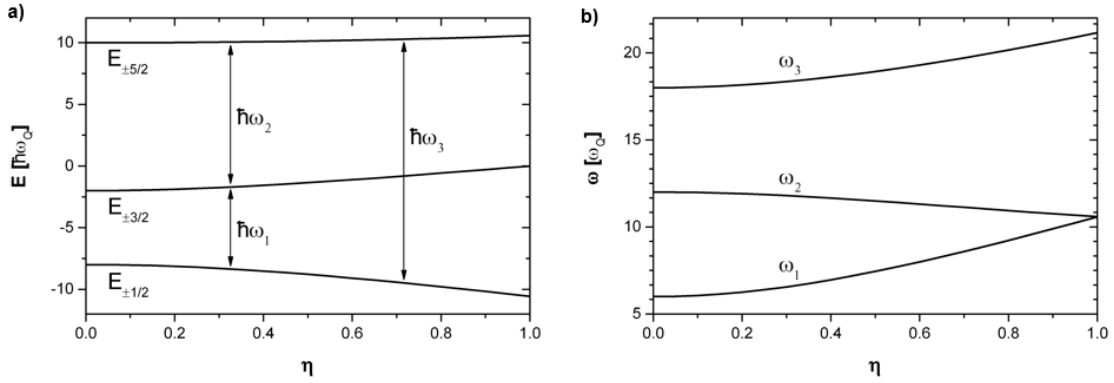

Figure 2.10 – Evolution of a I = 5/2 intermediate nuclear level of **a)** energy splitting and **b)** the associated interaction frequencies depending on the asymmetry parameter η. (Taken from Ref. 91)

2.4.2.4 Electric field gradient calculations: Point charge model

In the point charge model (PCM) the crystal ions are regarded as arrays of point ionic charges $Z_i e_i$, where Z_i represents the ionic valence, located at the ion sites, represented at r_i position from the origin. Therefore, EFG can be represented by a tensor whose components are the second spatial derivatives of the Coulomb potential ϕ at the probe site created by the external charges. The contributions of all lattice atoms, normally within the distance of a few tens of angstroms and except for the probe itself, have to be added.

$$V_{ij}^{PCM} = \frac{\partial^2 \phi(\vec{r})}{\partial x_i \partial x_j} = \sum_i \frac{z_i e}{4\pi\epsilon_0 r_i^5} \begin{bmatrix} 3x_i^2 - r_i^2 & 3x_i y_i & 3x_i z_i \\ 3y_i x_i & 3y_i^2 - r_i^2 & 3y_i z_i \\ 3z_i x_i & 3z_i y_i & 3z_i^2 - r_i^2 \end{bmatrix} \quad (2.23)$$

In covalent solids and large molecules, this approach fails, nevertheless, for ionic solids PCM provides a fair first approximation of EFG.

2.4.2.5 Ion implantation

At the Isotope Mass Separator On-Line facility (ISOLDE)[95], which is located in the Proton-Synchrotron Booster (PSB) at CERN, Switzerland, the isotopes are produced by nuclear reactions via irradiation of an appropriated target placed in the external 1 GeV proton beam delivered by the CERN PSB. This target under intense bombardment supplies the radioactive beam that after element selection and magnetic mass analysis is

steered to the experiments. With this process, a vast array of radioactive isotopes with great purity and high yield are available[93].

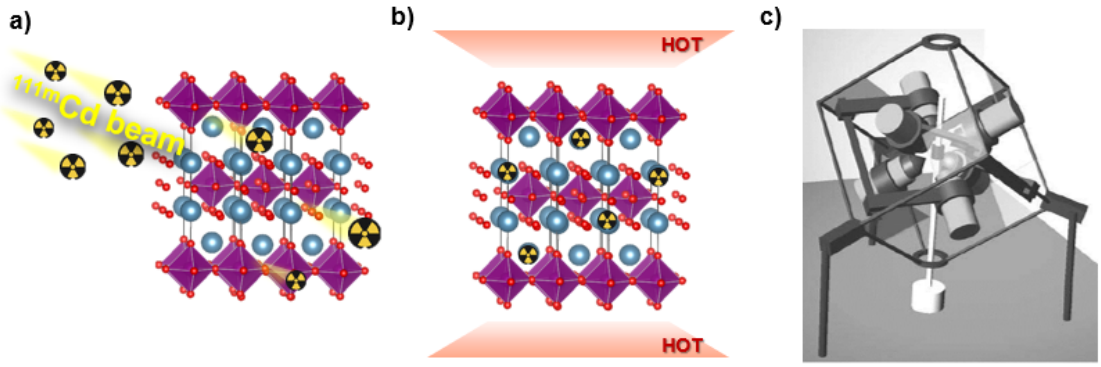

Figure 2.11 – **a)** Beam implantation of radioactive ^{111m}Cd probe atoms onto the studying material. The sample then it undergoes an **b)** annealing to promote ^{111m}Cd diffusion within its crystal structures. Finally, the sample is placed in the center of **c)** a 6 detector set up. Here it can be mounted a refrigerator/furnace for temperature dependent measurements. (Adapted from[89])

The experiments require the introduction of typically 10^{10} to 10^{12} radioactive probe atoms into the material under study. Besides ion implantation, see Fig. 2.11 a), these isotopes can be introduced into the samples in other ways for example the diffusion of a solution containing the desired isotope or irradiation. Even at a probe introduction of 10^{13} atoms, the concentration is quite low so that interference with properties of the sample and doping levels can be excluded. In the case of ion implantation it is necessary thermal annealing to assure that there are no radiation damages locally, see Fig. 2.11 b).

This technique stands out from the other hyperfine techniques given its temperature-independent sensitive, contrary to what happens in MES and NMR, of mechanical vibrations, not like NMR, and normally it is better at resolving weaker nuclear quadrupole interactions than MES. It also avoids the use of high-frequency equipment and the application of external magnetic fields such as in NMR.

The materials under study can be anything from biomolecules, gases, and solid-state materials of very small quantities such as 1 to 100 mg.

2.4.2.6 Experimental Details

At ISOLDE individual pellet samples ($\approx$ 1 mm^3) from the same batch material were implanted with a 30 keV energy beam of ^{111m}Cd ($t_{1/2}$ = 49 minutes). This radioactive probe was used for the ion implantation because of its similar ionic radius and same cation valences, hence Cd^{2+} probe ions easily substitute Ca^{2+}[96] in the $Ca_{n+1}B_nO_{3n+1}$ structures. In this way, the hyperfine fields will specifically be measured at the low concentration of Cd probe nuclei sitting at the Ca site.

After implantation, every single sample undertook a 20 min annealing at $\approx$ 1130 K in

the air to recover from any implantation damage. The recovery of point defects and the incorporation of the Cd probe at the right lattice sites is certified by the PAC measurement itself, leading to well-defined R(t) experimental anisotropy functions, see section 2.4.2.2. A single measurement, at a given stable temperature, takes $\approx 4h$ of acquisition time. Since the parent ^{111m}Cd probe has a short life-time, to cover a wide temperature range of measurements for every PAC spectrum point is required a fresh implantation.

The measurements were performed in a wide range of temperatures using a furnace for the high temperatures (up to 1200 K) and a closed-cycle helium refrigerator for the low temperatures (down to 8 K). Low-temperature measurements were done with the sample in vacuum while above room temperature the measurements were done with the sample in air atmosphere.

The measurements were performed using a 6-detector spectrometer of BaF_2. The R(t) experimental function was fitted with exact numerical methods that build the expected observable by solving the characteristic equations of the hyperfine interaction Hamiltonian[89].

CHAPTER 3

Calcium Manganese Oxides

Naturally layered calcium manganese oxides have been studied for a long time[17], yet the interest in these materials has been revived due to their recently discovered functional properties. In the following chapter, a brief introduction to the $Ca_{n+1}Mn_nO_{3n+1}$ (n = 1, 2) compounds focusing on the structural and consequent magnetic properties is given as they are the main subject of this work.

3.1 Introduction

As described earlier, the Ca_2MnO_4 structure consists in a stacking of $CaMnO_3$ blocks (one layer thick, n = 1), intercalated periodically with CaO, a rock-salt like layer. While the $Ca_3Mn_2O_7$ presents a homologous structure but with two layers thick (n = 2) of $CaMnO_3$ perovskite blocks.

The **Ca_2MnO_4** (n = 1) was first reported, similarly to K_2NiF_4, to be the tetragonal *I4/mmm*[17]. Later, it was found, by XRD measurements at the temperature range of 298 K up to 977 K, to exhibit the $I4_1/cad$ symmetry[97]. By extrapolating the thermal evolution of the Mn–O–Mn distortion angles obtained from Rietveld analysis (see Fig. 3.1 c)), *Takahashi et al.* predicted that the structural transition from the $I4_1/cad$ to the high symmetric tetragonal $I4/mmm$ would occur at ≈ 1500 K, well above the 977 K measured previously[97].

Neutron diffraction measurements[67,98,99] performed at lower temperatures (< 500 K) came to confirm that the experimental results can be well fitted within the $I4_1/cad$ space group. Even so, *Autret* and coworkers showed that Ca_2MnO_4 presented a relative lower structural coherence length along the c-axis. Using electron microscopy measurements[99] performed at room temperature, it was proposed by this group that Ca_2MnO_4 displayed a coexistence of two structural phases, tetragonal $I4_1/cad$ and orthorhombic *Aba2* structural phases in an apparent random stacking along the c-axis.

In the *Aba2* structural phase the MnO_6 octahedra rotate around the c-axis (and can be tilted along c) but unlike $I4_1/cad$, the MnO_6 octahedra in equivalent perovskite slabs, undergo an in-phase rotation. This results in lowering periodicity along the c-axis, ≈ 12 Å, when compared to ≈ 24 Å of the $I4_1/cad$ phase. Actually, the *Aba2* structural phase was only observed by XRD when performing calcium substitution by lanthanide

ions, in $Ca_{2-x}Ln_xMnO_4$ systems[100,101].

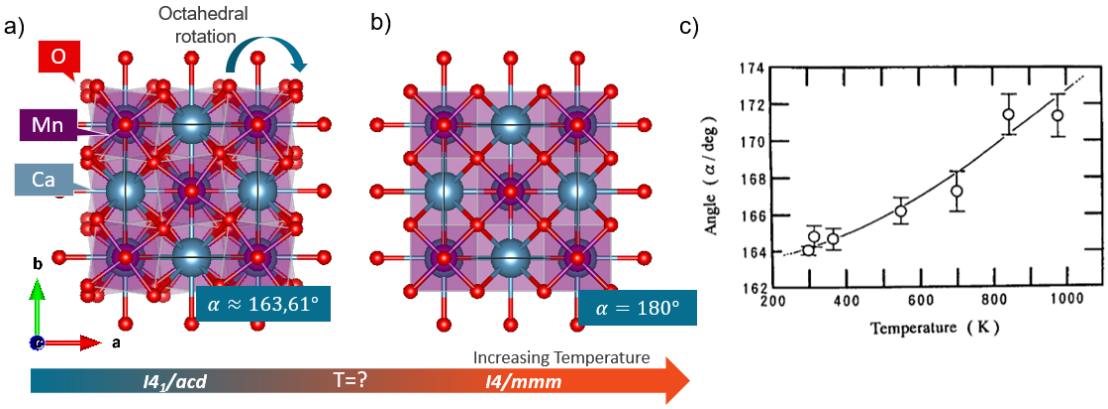

Figure 3.1 – The Ca_2MnO_4 structure in the **a)** distorted $I4_1/cad$ symmetry and in the **b)** highly symmetric $I4/mmm$. **c)** Temperature dependence of Mn-O-Mn bond angle α from XRD measurements. The estimated errors are indicated with bars. (Adapted from Ref. 97)

The $I4_1/cad$ phase is formed by one distortion mode, an oxygen octahedral rotation of MnO_6 around the [001] direction, P_4. In this symmetry, equivalent first neighbour and vertical MnO_6 octahedra undergo an out-of-phase rotation, highlighted by the blue and red arrows in Fig. 3.2 b).

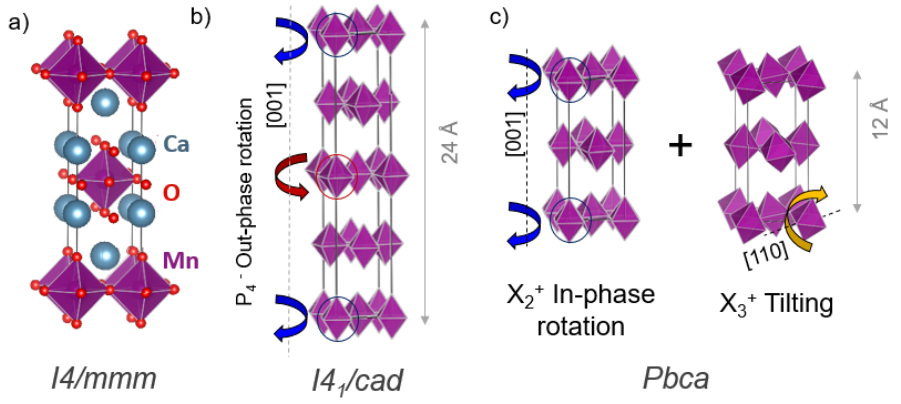

Figure 3.2 – **a)** The Ca_2MnO_4 structure in the aristotypical symmetry $I4/mmm$. The MnO_6 octahedra distortion modes for distinct structural phases: **b)** $I4_1/cad$; **c)** $Pcba/Aba_2$. Red/Blue circles highlight equivalent MnO_6 octahedra belonging to neighbour perovskite layers, and the colored arrows the orientation of the respective octahedral rotations. (Taken from Ref. 102)

For the **$Ca_3Mn_2O_7$** (n = 2) it was previously reported[103] that, at room temperature, this RP material was the I-centered tetragonal lattice symmetry, $I4/mmm$. This amiss characterization was latter blamed on the very small differences in the XRD pattern between the tetragonal and orthorhombic model, as expressed by *Guiblin*[104] in the Fig. 3.3.

The high temperature symmetry is attributed[1,12] to the tetragonal space group $I4/mmm$, just like in Ca_2MnO_4, although not yet confirmed.

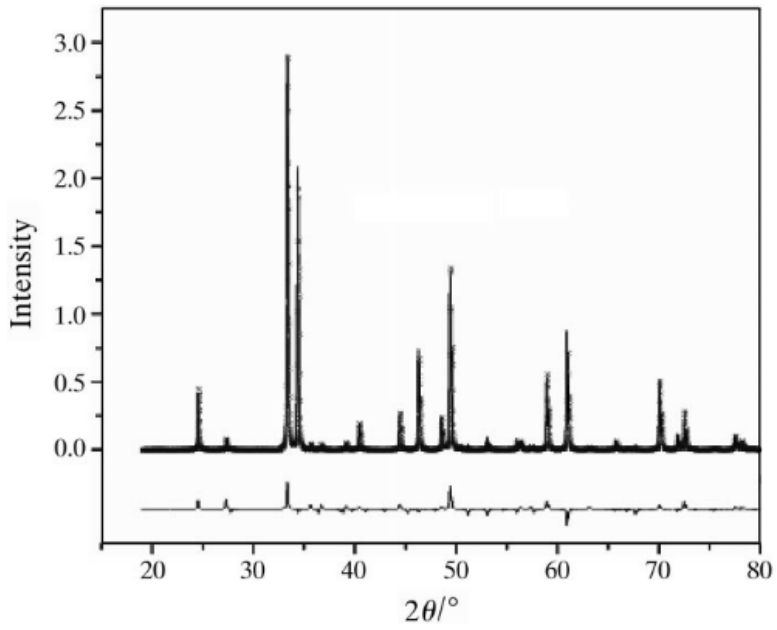

Figure 3.3 – Simulated XRD patterns for $Ca_3Mn_2O_7$ in the tetragonal *I*4/*mmm* and orthorhombic $A2_1am$ space group, with the respective difference at the bottom. (Taken from Ref. 104)

When at room temperature, it was possible to measure a mixture of phases with high-resolution x-ray powder diffraction. Here, the polar symmetry $A2_1am$ and the *Acaa* phase[20] (see Fig. 3.4), seem to coexist over a range of temperature (from 150 K to 350 K). Thus confirming what it was known from group theory[4,105] which strongly forbids direct transition from $A2_1am$ to *I4/mmm*. In this case an intermediate phase appears, the *Acaa*.

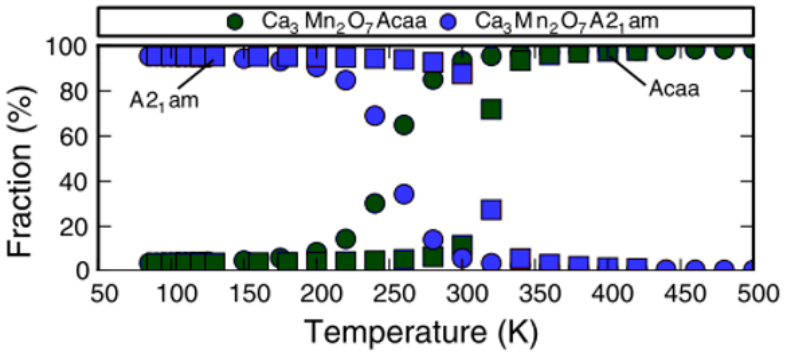

Figure 3.4 – **a)** Evolution of the phase fraction in $Ca_3Mn_2O_7$ as a function of temperature. Circle and square symbols represent data collected on cooling and warming respectively. (Adapted from Ref. 106)

The $A2_1am$ phase was found to be formed from the octahedral rotation (X_2^+) of MnO_6 and tilting (X_3^-) modes associated with an anti-displacement of the calcium ions (Γ_5^-). Since the *Acaa* phase (see Fig. 3.5) corresponds to having just a rotation and no tilting there is no possibility of HIF here[106].

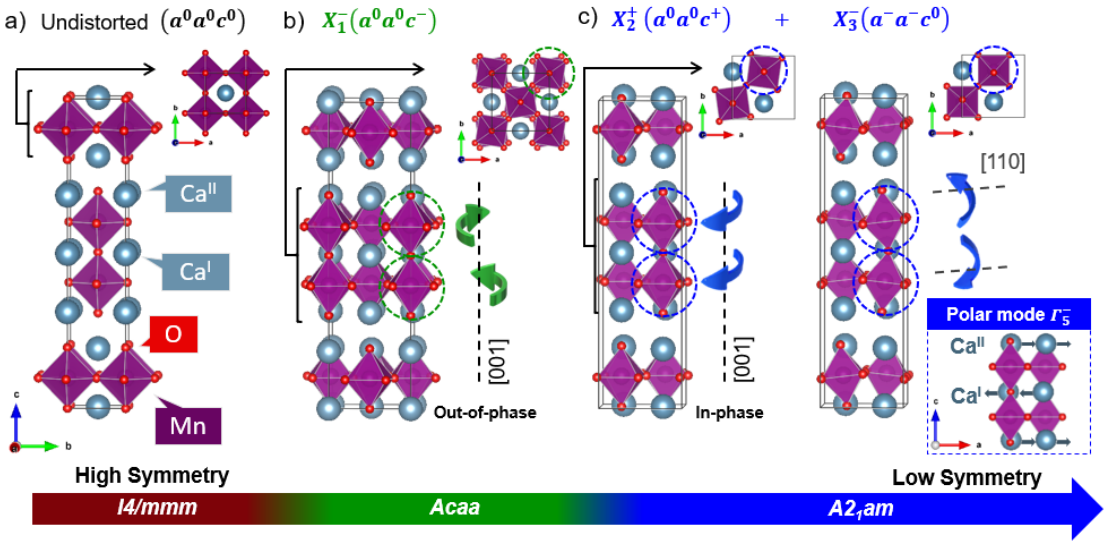

Figure 3.5 – Schematic view of each $Ca_3Mn_2O_7$ structure from the tetragonal *I*4/*mmm* to the *Acaa* (X_1^-) and $A2_1am$ (X_2^-, X_3^-) structural phases[106]. Green/blue arrows schematize the orientation of rotation and tilting of the MnO_6 octahedra that are enclosed by the respective green/blue dashed circles. (Adapted from Ref. 107)

The calcium cation anti-displacement (Γ_5^-) mode was predicted by *Benedek et al.* in 2011[1], resulting in a net ferroelectric polarization of $\approx 5\mu$ C/cm^2[1]. The polarization orientation was shown to be reversed by changing the sign either the rotational or tilting modes, see Section 1.2.3.1. Only recently, in 2018, experimental evidence for $Ca_3Mn_2O_7$[108] has been obtained for its HIF, measuring a switchable ferroelectric polarization and also an electrical field induced decrease in magnetization ($\approx 3\%/\approx 6\%$) at low temperatures (10 K[108]/4 K[9]).

The magnetic susceptibility measurements show spontaneous magnetic ordering to antiferromagnetic states at $T_N \approx 110$ K for both Ca_2MnO_4 and $Ca_3Mn_2O_7$[103], see Fig. 3.6 a). This magnetic transition temperature is confirmed by several magnetic studies[99,103,109–112].

The observed bump at higher temperatures[99,109,113], *i.e.* deviations from the Curie-Weiss law in the paramagnetic region, (≈ 230 K) is characteristic of layered compounds, since it corresponds to magnetic interactions in the planes that are not coherent along the stacking c-axis. It was noticed by *Fawcett*[103] that theses deviations from the Curie-Weiss law increased with lower dimensionality, *e.g.* from $Ca_3Mn_2O_7$ to Ca_2MnO_4, this could be perceived in Fig. 3.6 a).

Additionally, ZFC and FC modes, for the two compounds[109,114], show a deviation in magnetic susceptibilities below T_N. Hence, it suggests that the magnetic moments of Mn^{4+} ions order with a slight ferromagnetic component below T_N[115]. This net magnetization is caused by Dzyaloshinsky-Moriya (D-M) interactions[112].

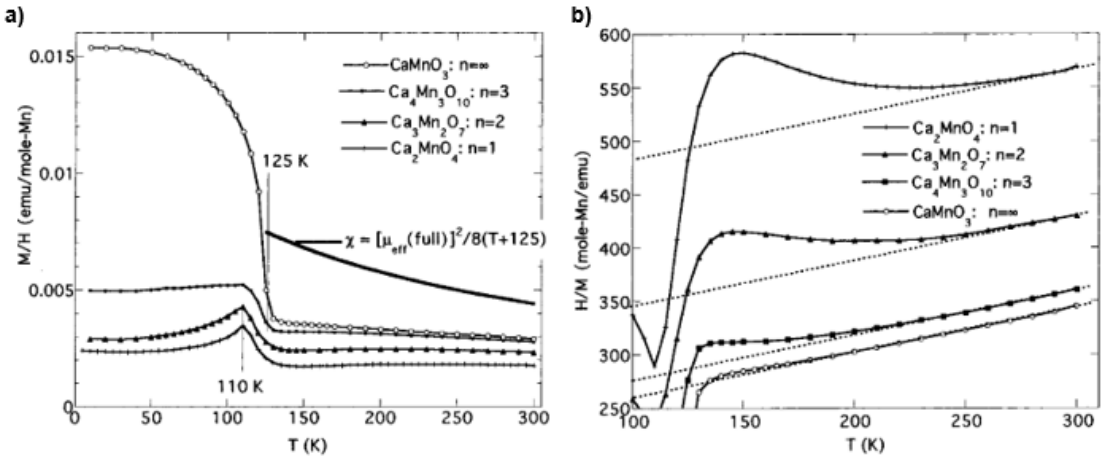

Figure 3.6 – **a)** Molar magnetic susceptibility, χ, of the RP series $Ca_{n+1}Mn_nO_{3n+1}$ for $n = 1, 2, 3$ and ∞, as a function of temperature in a field of 15 kG. **b)** The corresponding inverse of magnetic susceptibility, χ^{-1}. The dot line represents the Curie-Weiss law. (Taken from Ref. 103)

In Fig. 3.6, the magnetic susceptibility was described as following the Curie-Weiss law in the temperature range of 200 K to 350 K. Although in some studies, *e.g.* in Ca_2MnO_4, the linearity of the inverse susceptibility is only guaranteed above 300 K[103,116] or 500 K[110].

This linear fit, presented in Fig. 3.6 b), yielded a Θ_p= -1037 K for Ca_2MnO_4 and Θ_p= -714 K for $Ca_3Mn_2O_7$. This negative Weiss constant shows that the spin alignment is antiferromagnetic.

The effective magnetic moment of the manganese ions in $Ca_3Mn_2O_7$ was estimated to be 4.19 μB[115] and in Ca_2MnO_4 4.34 μB[103], which are larger than the theoretical value. The theoretical value of effective magnetic moment, M_{eff}, for Mn^{4+}, is calculated to be 3.84μ_B/Mn. Since Mn^{4+} has the electronic distribution of $3d_3$, no Jahn-Teller effect should occur in this system.

Other interesting property for materials engineering, the uniaxial NTE was experimentally measured in both **Ca_2MnO_4**[20,97,99] and **$Ca_3Mn_2O_7$**[106], see Fig. 3.7. The measured NTE coefficient are ≈ -4.4 ppm/K and ≈ -3.6 ppm/K both for Ca_2MnO_4 and $Ca_3Mn_2O_7$, respectively. In Fig. 3.7 b) it is seen that the $A2_1am$ displays positive thermal expansion of the c-axis in $Ca_3Ti_2O_7$ and $Ca_3Mn_2O_7$.

Generally, many NTE compounds contain transition metals which increase product cost[65]. On the other side, calcium and manganese are quite abundant in the Earth's crust and, in the case of manganese, it is known a large worldwide production due to its importance in industrial metal alloys.

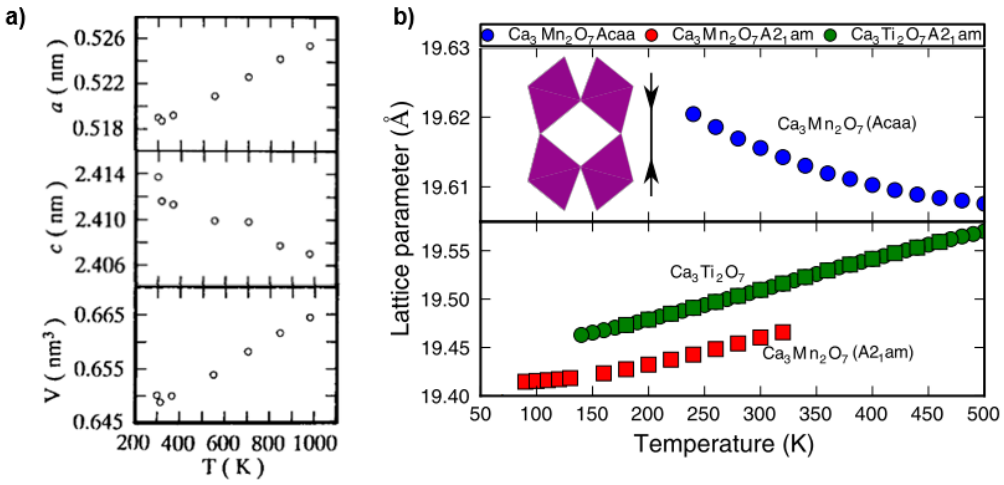

Figure 3.7 – Temperature evolution of the lattice parameters showing the uniaxial NTE according the c-axis of **a)** Ca_2MnO_4 and **b)** $Ca_3Mn_2O_7$. For the phase *Acaa* at high temperatures it is consistent with a soft mode mechanism (shown in inset). Circle and square symbols represent data collected on cooling and warming respectively. (Taken from Refs. 97,106)

3.2 Sample Preparation

In this work, it was performed a standard solid-state reaction for the preparation of polycrystalline samples using high purity reagents $CaCO_3$ (99.0%, Sigma-Aldrich) and MnO_2 (99.99%, Sigma-Aldrich) mixed in a stoichiometric ratio and carefully ground in an agate mortar. This technique is not the only one available to produce RP compounds as it can be found in the literature other synthesizing systems[111,117], *e.g.* citrate sol-gel process[103,118], nevertheless, this presents as a simple and reliable method.

These samples were then pressed into pellets and underwent through a set of heat treatments with intermediate grindings as described in Section 2.1 with the parameters summarized in Table 3.1. The crucible was made of high-density Al_2O_3 and in between annealings the samples were reground and pelletized.

Table 3.1 – Nominal compositions, Calcination, Heat Treatment and label of the studied calcium manganese naturally layered perovskites.

Nominal Composition	Calcination	Heat Treatment	Label
Ca_2MnO_4	1123 K (3h)	1473 K (12h)	NIU
$Ca_3Mn_2O_7$	1123 K (3h)	1648 K (12h)	CMO

Measurements of thermogravimetry[97] found a (reversible) reduction of $\delta = 0.06$ in $Ca_2MnO_{4-\delta}$ at 1573 K, see Fig. 3.8. Although no sample was measured at such high-temperatures.

To assure that the compounds produced were pure it was performed a powder x-ray diffraction pattern, see Figs. 3.9, and 3.15.

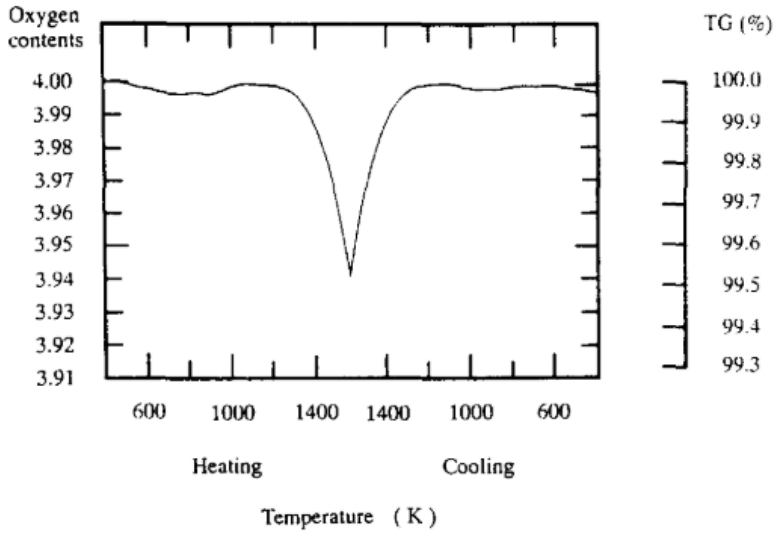

Figure 3.8 – Temperature dependence of weight of Ca_2MnO_4 in air. (Taken from Ref. 97)

3.3 Ca_2MnO_4 (n = 1)

3.3.1 Crystallographic Characterization

The sample's crystallographic structure and lattice parameters have been checked and refined employing x-ray powder diffraction (XRD), in Bragg Brentano (BB) mode at RT (300 K). A Le Bail profile matching was applied using as starting fitting parameters neutron powder diffraction data from Ref. 99. The resulting diffractogram of the experimental data, the calculated diffraction pattern, their difference and the respective Bragg reflections are presented in Fig. 3.9.

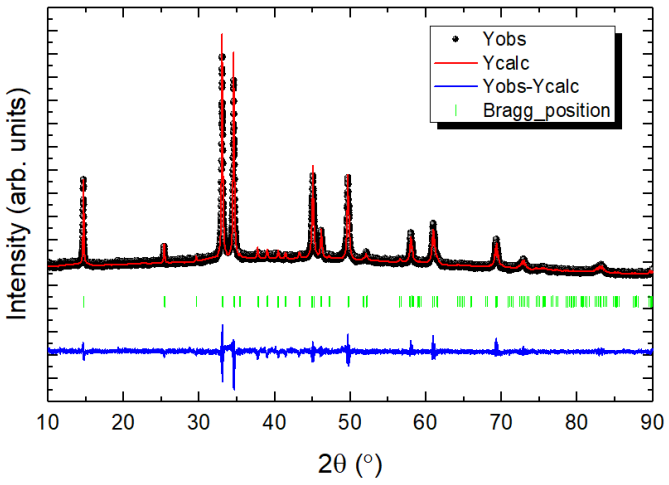

Figure 3.9 – The XRD experimental data of Ca_2MnO_4 and the respective Le Bail refinement output, namely, the calculated diffraction pattern, the difference between the calculated and measured diffractogram (at the bottom) and the respective Bragg reflections for this symmetry.

The fit reveals that the sample is single phase.The crystallographic parameters are a = 5.188(1) Å and c = 24.132(1) Å, in the space group $I4_1/cad$. Similar cell parameters have been found in literature for this system in Refs. 99,103,114,119.

3.3.2 Magnetic Characterization

In Fig. 3.10 is shown the temperature dependence of the molar magnetic susceptibility, χ_{molar}. Two modes were measured: the FCC (300 K → 5 K) and FCH (5 K → 300 K), both under a magnetic field of 200 Oe. Comparing the two curves no major differences can be observed, *i.e.* a satisfactory overlap between them is observed, thus assuring the system reversibility as a function of temperature.

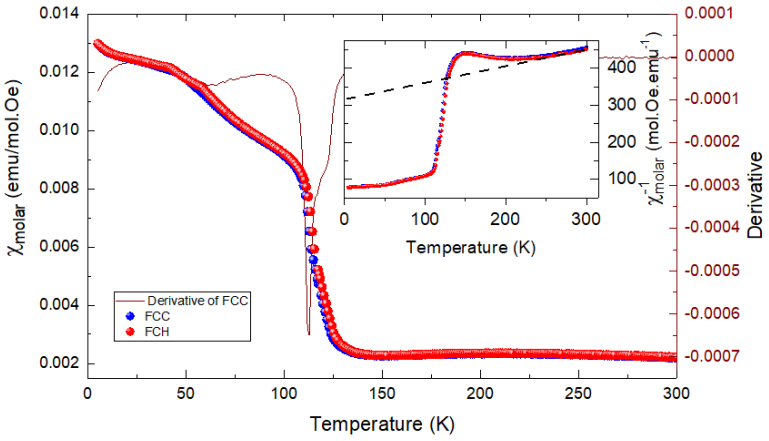

Figure 3.10 – Molar magnetic susceptibility of Ca_2MnO_4 measured at 200 Oe for the FCC and FCH modes with the respective derivative of the FCC. Inset: Molar inverse magnetic susceptibility, χ^{-1}, of Ca_2MnO_4 as a function of temperature. The dashed line represents the Curie Weiss law.

When the temperature decreases from room temperature, both the FCC and the FCH curves sharply increase at ≈ 113 K which corresponds to the Néel Temperature, T_N, which is in good agreement with the previous values found[99,103,109–111]. Observing the inverse magnetic susceptibility in the interval 250 K to 300 K it is seen that the magnetic susceptibility follows approximately the Curie-Weiss law (see Eq.2.5). Using a linear fit in this region it is obtained $C \approx 2.40$ emu Oe K mol^{-1} and $\theta_p \approx -792.42$ K. The μ_{eff} is estimated to be $4.38\mu_B$ which is higher than the predicted, spin-only, value for Mn^{4+} ion, i.e. $3.84\mu_B$ although similar to the measured $4.34\mu_B$ by *Fawcett*[103].

The value for θ_P is negative, as expected for an antiferromagnetic alignment of the spins, even though its value is quite different from other found in literature, *e.g.* -1037 K[103]. This might happen because the linearity needed for the application of the Curie-Weiss law might not be fully reached in the temperature range[110,116]. According to *Fawcett*[103] the Curie-Weiss law in Ca_2MnO_4 is guaranteed only for temperatures above 300 K, hence above the highest experimental temperature.

In the Fig. 3.11 it is shown isothermal magnetization as a function of a magnetic

field, M-H curves, which were measured in the range between -50 kOe to 50 kOe at temperatures above/below T_N (5 K/300 K).

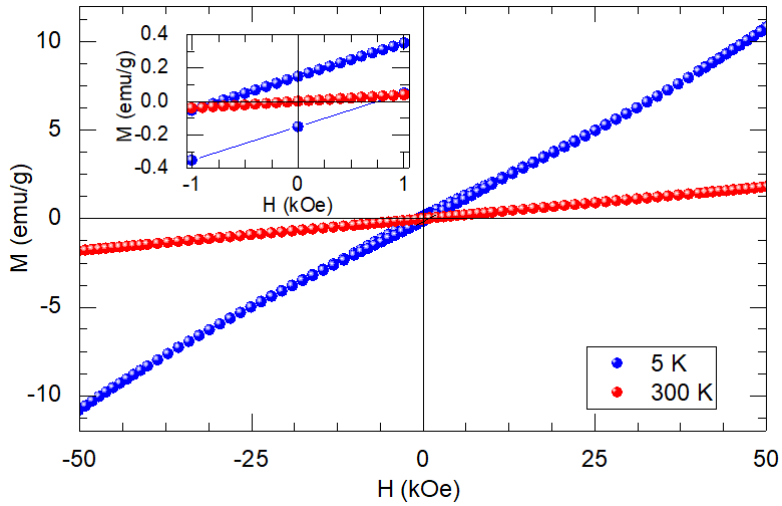

Figure 3.11 – Magnetic measurement of Ca_2MnO_4 at 5K and 300 K from -50 kOe to 50 kOe. Inset: the corresponding enlarged views of M-H loops at a low magnetic field, -1 kOe to 1 kOe.

The value of magnetization increases continuously with the magnetic field, which is not saturated even under a high field up to 5 kOe. The value of the coercive field, H_c, at 5 K was ≈ 700 Oe, as it can be seen in the inset in Fig. 3.11. This small magnetic irreversibility might be due to the weak ferromagnetism behavior foreseen in previous measurements[109].

3.3.3 Perturbed Angular Correlation Results

At the ISOLDE facilities, using a radioactive probe of ^{111m}Cd in the temperature range from 10 K to 1200 K, it was performed several PAC measurements as described in the Section 2.4.2.6. In the Fig. 3.12 depicts the representative experimental R(t) anisotropy function and the respective Fourier transform obtained by the measurements. The fits to the R(t) experimental data were performed considering by only electric quadrupole interactions and static regular EFG distributions assumed to be Lorentzian-like.

Here, it is possible to notice that at both low and high temperatures there are two distinct electrical field gradients, correspondingly EFG1 and EFG2. At low temperature, the EGF1 is characterized by having axially a low symmetry, $\eta \approx 1$. Then, the system goes through a mixture of phases ending up in the EFG2, which is characterized by being highly symmetric, $\eta \approx 0$. This can be more intuitively seen in the evolution of the frequency from a doublet (ω_1=ω_2, ω_3) to a triplet of frequencies (ω_1, ω_2, ω_3) in Fig. 3.12 (right side).

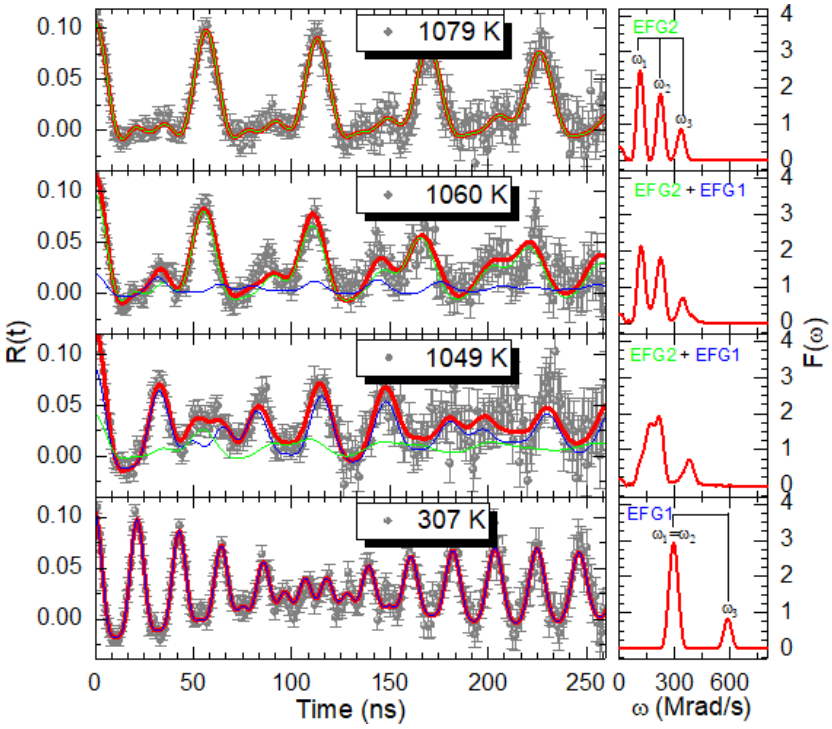

Figure 3.12 – Representative R(t) functions with the corresponding fits, and respective Fourier transforms taken at different temperatures using the ^{111m}Cd probe. The blue (EFG1) and green (EFG2) lines correspond to two different fractions at characteristic frequency which its sum represented in red.

In the Fig. 3.13 it is represented the fitting parameters obtained for the distinct measuring temperatures, such as the EFG principal component, V_{zz}, and the asymmetry parameter, η. At room temperature the EFG1 is characterized by a $V_{zz} \approx 90$ V/Å^2 with $\eta \approx 0.9$ (identified as the blue dots in 3.13) while at the highest temperatures the EFG2 is characterized by a $V_{zz} \approx 57 V$/Å^2 with $\eta \approx 0$ (identified as the green dots in 3.13).

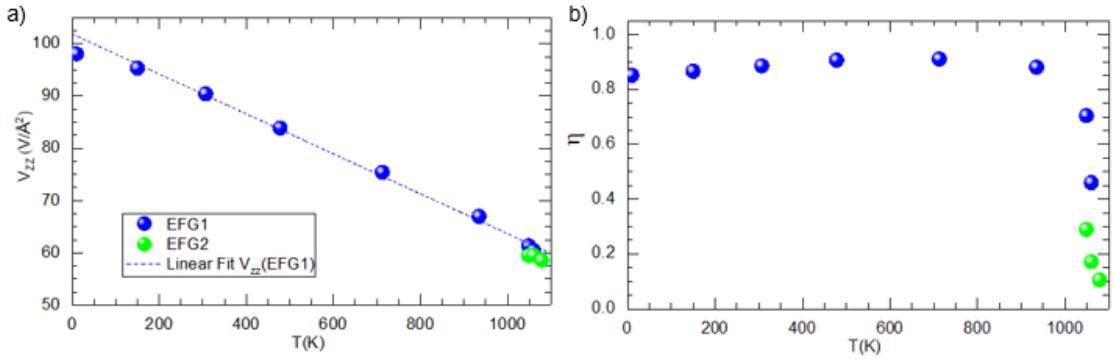

Figure 3.13 – **a)** Experimental electric field gradient, V_{zz} and the **b)** asymmetry parameter, η, evolution with temperature for the Ca_2MnO_4 sample.

The EFG temperature dependence has been extensively studied in solids[89,90]. In order to evaluate its tendency is possible to use a least-squares fit defined as V_{zz} =

$V_{zz}(0)(1+\alpha T)$. For the EFG1 it was obtained a negative coefficient of α_{EFG1} = –3.74(8)$x10^{-4}$ K^{-1}.

The decrease of V_{zz} with increase temperature observed in Fig. 3.13 is common for perovskite structures and is frequently associated with the increase of the atomic vibrations and (volume) thermal expansion[89]. However, the V_{zz} temperature dependence cannot be attributed exclusively to a thermal expansion because its coefficient is usually one order of magnitude smaller. Nevertheless, this temperature dependence V_{zz} coefficient is similar to those presented by manganites with perovskites structures with the same order of magnitude[89,90].

In Fig. 3.14 it is presented the phase evolution, *i.e.*, the temperature evolution of the associated EFG1 and EFG2 phases described previously in Fig. 3.12. Above 1000 K it is observed a sharp decrease of the EFG1 with a correspondent increase of the EFG2.

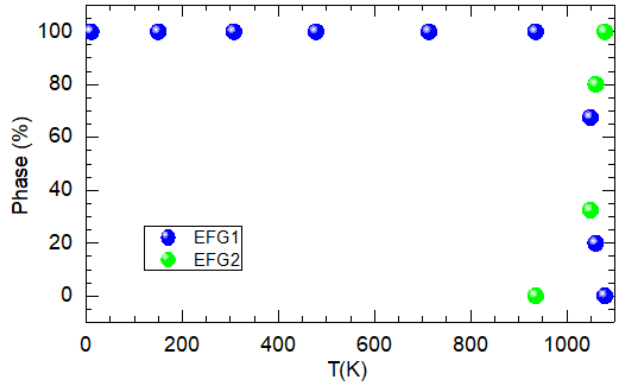

Figure 3.14 – Temperature evolution of the EFG1 and EFG2 described previously in Ca_2MnO_4.

When observing the asymmetry evolution, in Fig. 3.13 b), and the phase evolution, in Fig. 3.14 the experimental results suggests a transition from a local environment at low temperatures to a completely different at high temperatures within the temperature range from 1049 K to 1079 K. This transition is also perceived in the frequency domain of the experimental PAC data, see Fig. 3.12.

Given that the tetragonal *I*4/*mmm* is highly symmetric, η should be around zero for this phase and non-zero for the lower symmetry phase, $I4_1/cad$, as confirmed with point charge model simulations. These results are interpreted[102] as a shred of possible evidence for the structural transition from the *I4/mmm* to the $I4_1/cad$. Surprisingly, in this case, it was noted to occur at a much lower temperature (from 1049 K to 1079 K) than the predicted 1500 K by *Takahashi*[97].

In contrast to the TEM results published by *Autret* and co-workers[99] which suggested a coexistence of the $I4_1/cad$ and *Aba2* in this work it was found solely one, well defined, local environment at room temperature conditions, see Fig. 3.12 (307 K).

3.4 $Ca_3Mn_2O_7$ (n=2)

3.4.1 Crystallographic Characterization

The sample's crystallographic structure has been checked employing x-ray powder diffraction (XRD), in Bragg Brentano (BB) mode at RT (300 K). In Fig. 3.15 it is presented the XRD pattern of $Ca_3Mn_2O_7$ and the simulated XRD pattern of *Acaa* and *A*2$_1$*am* at 260 K from CIFs in Ref.[106].

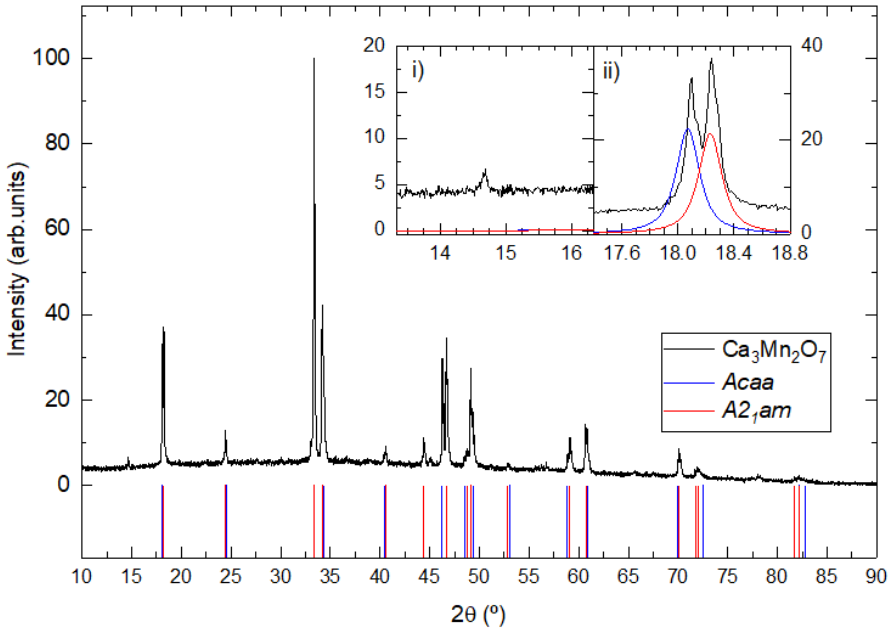

Figure 3.15 – X-Ray diffraction pattern of $Ca_3Mn_2O_7$ at room temperature (black line). In the bottom is displayed the reflections of the *Acaa* phase and the *A*2$_1$*am* phase from simulated XRD patterns (CIFs from Ref. 106 at 260 K). Insets: (i) the single 14.5°peak; (ii) the corresponding double peaks for the *Acaa* and the *A*2$_1$*am* phases.

By direct comparison, it is confirmed that the two known phases, *Acaa* and *A*2$_1$*am*, which are expected to coexist at room temperature, are indeed present in the sample, see the inset in Fig. 3.4 ii). The pattern also possesses an odd peak at ≈ 14.5° that was formerly observed in Ca_2MnO_4.

3.4.2 Magnetic Characterization

In Fig. 3.16 is presented the temperature dependence of the molar magnetic susceptibility, χ_{molar}. Several modes were measured: FCC1 (300 K → 5 K); FCH1 (5 K → 300 K); FCC2 (300 K → 5 K); FCH2 (5 K → 300 K) always under a magnetic field of 200 Oe.

When the temperature decreases from room temperature, both the FCC and the FCH curves sharply increase at 111 K which corresponds to the Néel Temperature, T_N, which is in good agreement with the previous values found[103,108,111,112,120]. Observing the inverse magnetic susceptibility in the interval 250 K to 300 K it is seen that the

magnetic susceptibility follows approximately the Curie-Weiss law (see Eq.2.5). Using a linear fit in that temperature range it is obtained $C \approx 3.5$ emu Oe K mol^{-1} and $\theta_p \approx -400$ K, close to the measured by *Fawcett*[120] of –465 K. The μ_{eff} is estimated to be 5.28μ_B which is higher than the measured 4.19μ_B[115], and much higher than the predicted value for, spin only, Mn^{4+} ion, *i.e.* 3.84μ_B. This might happen because the linearity needed for the application of the Curie-Weiss law might not be fully reached in the temperature range.

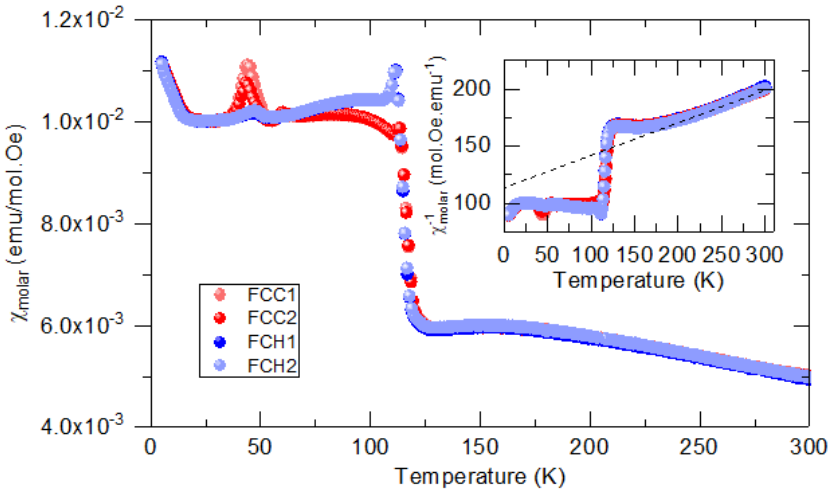

Figure 3.16 – Molar magnetic susceptibility of $Ca_3Mn_2O_7$ measured at 200 Oe during heating (FCH1/FCH2) and cooling (FCC1/FCC2). Inset: Molar inverse magnetic susceptibility, χ^{-1}, of $Ca_3Mn_2O_7$ as a function of temperature. The dashed line represents the Curie Weiss law.

Near the T_N it is found a divergence from the measurements, that were done while heating and while cooling, which might be due to short-range correlations in the magnetic stacking[112].

A small upturn below 15 K, persisting down to 4 K, is supposed to be due to the paramagnetic spins at low concentration[112].

An extra peak at 45 K appears in Fig. 3.16 and, although it is more expressive in the measurements done while heating (FCH1 and FCH2), this is regarded as a typical behavior when there is experimental contamination of O_2[121].

Fig. 3.17 shows the temperature dependence of the molar susceptibility, χ_{molar}. The experimental data were obtained in the zero-field cooling (ZFC) mode under a magnetic field of 200 Oe.

When reaching T_N, the FC curve starts to abruptly differ from the ZFC curve[i]. Such magnetic behavior is a characteristic of a weak ferromagnet, then the low-temperature phase at $T < T_N$ has a weak ferromagnetic moment. These results indicate that the magnetic moments are canted below T_N, such as in Refs. 9,122.

[i] Below 250 K there is also a mismatch between the FC and ZFC curves because in the FC measurement there was a remanent field in the SQUID coils (due to previous measurements) that it was needed to adjust to the gathered data. The value estimated was ≈ 24 Oe.

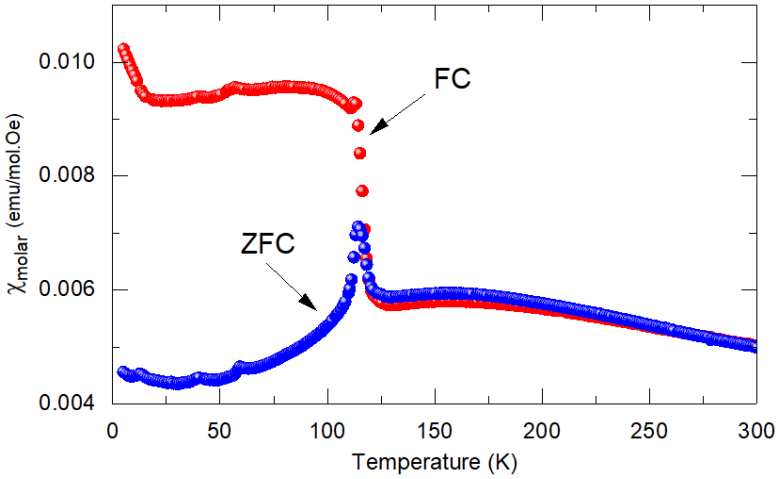

Figure 3.17 – Molar magnetic susceptibility of $Ca_3Mn_2O_7$ as a function of temperature, cooled in zero field (ZFC) and in a field of 200 Oe (FC).

In the Fig. 3.18 it is shown isothermal magnetization as a function of a magnetic field, M-H curves, which were measured in the range between -50 kOe to 50 kOe at temperatures above/below T_N (125 K/5 K).

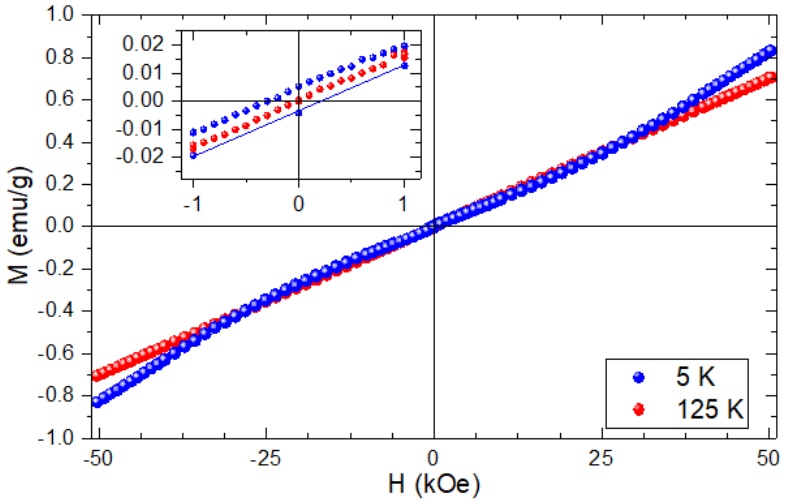

Figure 3.18 – Magnetic Measurements of $Ca_3Mn_2O_7$ at 5K and 125 K from -50 kOe to 50 kOe. Inset: the corresponding enlarged views of M-H loops at low magnetic field, -1 kOe to 1 kOe.

The value of magnetization increases continuously with the magnetic field, which is not saturated even under a high field up to 5 kOe. The value of the coercive field, H_c, at 5 K was ≈ 260 Oe, as it can be seen in Fig. 3.18 inset. This small magnetic irreversibility might be due to the weak ferromagnetism behavior foreseen in previous measurements[9,122].

3.4.3 Perturbed Angular Correlation Results

At the ISOLDE facilities, using a radioactive probe of ^{111m}Cd in the temperature range from 11 K to 1200 K, it was performed several PAC measurements as described in the section 2.4.2.6. In the Fig. 3.19 depicts the experimental R(t) anisotropy function and the respective Fourier transform. The fits to the R(t) experimental data were performed considering only electric quadrupole interactions and static regular EFG distributions assumed to be Lorentzian-like.

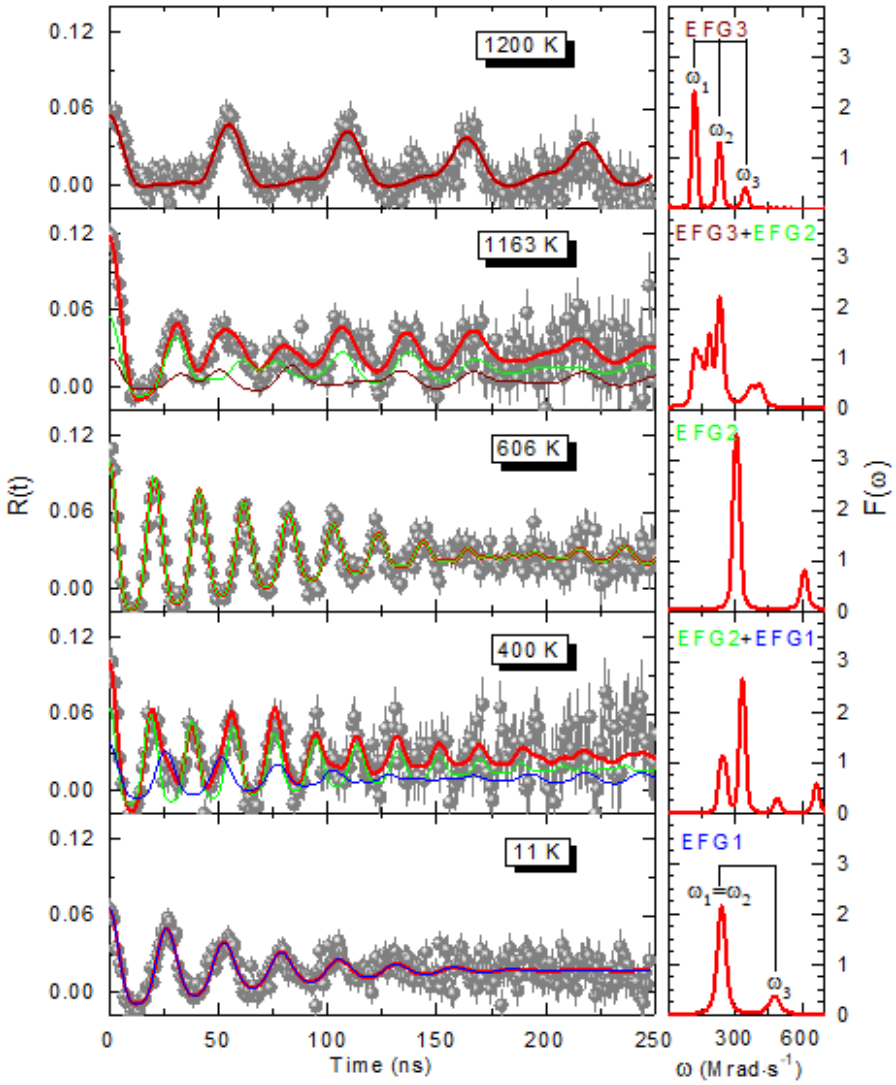

Figure 3.19 – Representative R(t) functions with the corresponding fits, and respective Fourier transforms taken at different temperatures using the ^{111m}Cd probe. The blue (EFG1), green (EFG2) and brown (EFG3) lines correspond to two different fractions at characteristic frequency which its sum represented in red.

Here, it is possible to notice three distinct electrical field gradients, see Fig. 3.19 (right side). The EFG3, a highly symmetric local environment at 1200 K, represented by an equidistant frequency triplet in the Fourier Transform. The EFG2, a low symmetric local

environment at 606 K, with a phase coexistence at 1163K and 400 K. And, at last, the EFG1, a low symmetric local environment at 11 K, represented by an doublet ($\omega_1 = \omega_2$, ω_3).

In the Fig. 3.20 it is represented the fitting parameters obtained for the distinct measuring temperatures, such as the EFG principal component, V_{zz}, and the asymmetry parameter, η. At room temperature the EFG1 is characterized by a $V_{zz} \approx 75.5\ V/Å^2$ with $\eta \approx 1$ (identified as the blue dots in Fig. 3.20) and the EFG2 is characterized by a $V_{zz} \approx 106\ V/Å^2$ with $\eta \approx 1$ (identified as the green dots in Fig. 3.20). At 1200 K the EFG3 is characterized by a $V_{zz} \approx 60.8\ V/Å^2$ with $\eta \approx 0.1$ (identified as the brown dots in Fig. 3.20).

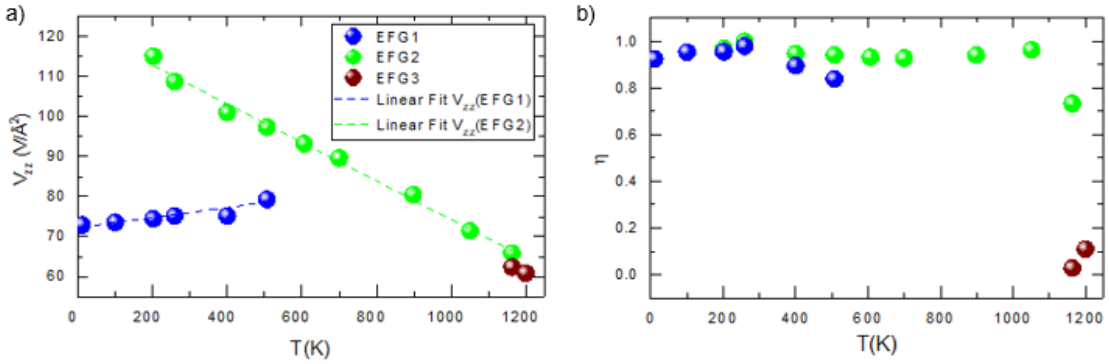

Figure 3.20 – **a)** Experimental electric field gradient, V_{zz}, for the $Ca_3Mn_2O_7$ sample and the **b)** asymmetry parameter evolution with temperature.

In order to evaluate their tendency is possible to use a least-squares fit defined in Eq.3.3.3. For the EFG1 it was obtained a positive coefficient of $\alpha_{EFG1} = 1.7(3)x10^{-4}\ K^{-1}$ and for the EFG2 a negative coefficient of $\alpha_{EFG2} = -3.9(3)x10^{-4}\ K^{-1}$. Both coefficients are in the same order as to the one found for Ca_2MnO_4.

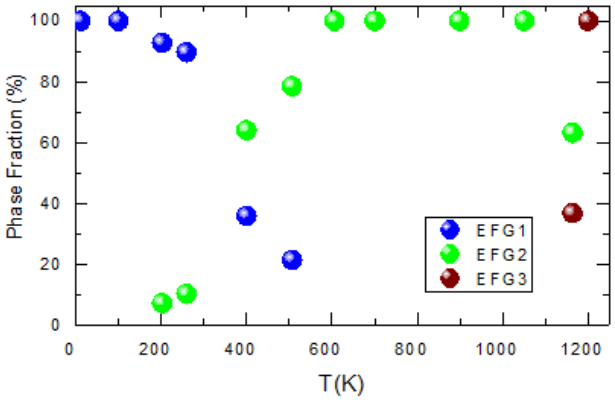

Figure 3.21 – Temperature evolution of the three different EFG found in $Ca_3Mn_2O_7$.

In Fig. 3.21 it is presented the phase evolution, *i.e.*, the temperature evolution of the

associated EFG1, EFG2 and EFG3 phases described previously in Fig. 3.19. From 11 K until 100 K there is solely the presence of a single EFG1. From therein up to to 507 K it is observed a coexistence of EFG1 and EFG2 with an increasing percentage of the EFG2. Then it stabilizes in a single phase of EFG2 from 606 K up to 1051 K. Here, a percentage of the EFG3 quickly emerges until 1200 K.

From the magnetic measurements in section 3.4.2, which have shown the phase transition from a paramagnetic to antiferromagnetic at T_N = 115 K, it is seen that below this magnetic phase transition, the magnetic hyperfine interaction between the canted antiferromagnetic ions and the probe nuclear magnetic dipole moment offers no abrupt change to the R(t) function. Instead, a gradual increase of the R(t) damping is observed for decreasing temperature and a broader peak in the respective Fourier Transform at 11 K, see Fig. 3.19.

Based on the literature[4,20,105,106], it is suggested that the EFG1, EFG2 and EFG3 are the $A2_1am$, *Acaa* and $I4/mmm$ space groups, correspondingly. When compared with the high-resolution XRD[106] results concerning the ferroelectric $A2_1am$ and the non-polar *Acaa* phase in this work it is perceived a wider persistence, from $\approx$ 200 K to $\approx$ 500 K, *i.e.* when heating up to $\approx$ 500 K the $A2_1am$ structure persists, whereas it was previously shown that it should be almost fully converted to the *Acaa* phase around 350 K. Thus, these results suggest the presence of small clusters of the $A2_1am$ phase up to 500 K.

The phase diagram recently published by *Ablitt et al.*[20] shows that, within the range from $\approx$ 350 K to 1150 K, purely the *Acaa* phase is observed. Our work found a low symmetry single phase but in the range of 607 K up to 1051 K. Hence, disapproving of the reported existence by *Liu et al.*[108] of the $I4/mmm$ phase at 673 K.

The local nature of the technique allows a precise atomic position assignment, within the unit cell, when this experimental data are complemented with the theoretical DFT results[107]. It is worth to notice that the axial symmetry observed at high temperatures in $Ca_3Mn_2O_7$, which was expected to be the same *I4/mmm*, agrees with the high axial symmetry observed in the local probe studies performed for the homologous Ca_2MnO_4, see Section 3.3.3. Thus, $Ca_3Mn_2O_7$, cadmium probes should occupy the Ca sites located in the rock-salt layers, see the Ca^{II} in the Fig. 3.5.

3.5 Thin film deposition

Strain and dimensional confinement can be used to tune magnetic and ferroelectric properties or improve material performance. In epitaxial films, the different lattice spacing of an underlying substrate can be used to impose a biaxial strain. Experimental studies have shown that strain engineering can induce multiferroicity and influence the magneto-electric properties in thin films[2]. Despite the influence on these properties, there is still little published research on these thin-film systems.

In $Ca_3Ti_2O_7$ thin films, it was found out that the coercive field is nearly two orders of magnitude lower than the bulk single crystals. Nevertheless, this effect on the H_c is attributed by *Li et al.*[53] to the lattice imperfections in the thin films rather than substrate-induced lattice strains, thus suggesting high sensitivity of the ferroelectric properties to lattice defects.

Previous studies have successfully deposited Ca_2MnO_4[123] on polycrystalline spark plasma sintered Sr_2TiO_4(STO) substrates and $Ca_3Mn_2O_7$[124] on $YAlO_3$ substrates. In this last, magnetic properties were measured without any significant differences comparing with the bulk $Ca_3Mn_2O_7$.

There are several depositing techniques from reactive molecular-beam epitaxy (MBE) to the one used in this work, the pulsed laser deposition (PLD) as previously introduced in section 2.1.3.

3.5.1 Sample Preparation

Using a standard Pulsed Laser Deposition (PLD) technique, it was initiated the study of $Ca_3Mn_2O_7$(CMO) deposition in $SrTiO_3$(STO) and Si substrates. An oxidant, O_2, was inserted in the deposition chamber. The depositing conditions are summarized in Table 3.2. After the deposition, the samples were slowly cooled at atmospheric pressure in the air.

Table 3.2 – Thin film deposition conditions of $Ca_3Mn_2O_7$

Substrate	Label	$T_{deposition}$ (°C)	$t_{deposition}$ (min)
$SrTiO_3$	Sample A	717	20
Si	Sample B	$\approx$ 520	30
Si	Sample C	717	20

In Fig. 3.22 can be seen as distinct optical differences between each sample. Both sample B and sample C display a blue coloration although in the last one is solely concentrated in a spot in the middle of the Si substrate.

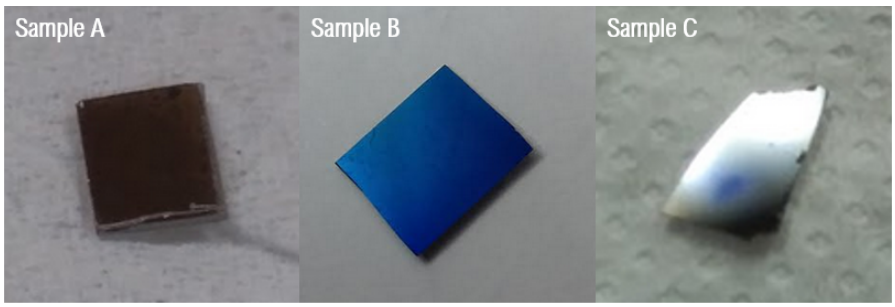

Figure 3.22 – Photo of $Ca_3Mn_2O_7$ deposited thin films, samples A, B and C. The dimensions are $\approx$ 0.5 x 0.5 cm.

3.5.2 Crystallographic Characterization

The sample's crystallographic structure has been checked employing x-ray diffraction to determine the phase purity, orientation, and structural perfection of the films. it was used the Bragg Brentano (BB) mode for sample A and sample B and the Parallel Beam (PB) for sample C, all at RT (300 K). In Fig. 3.15 it is presented the XRD pattern of $Ca_3Mn_2O_7$ (CMO) and the simulated XRD pattern of *Acaa* and $A2_1am$ from CIFs[106] at 260 K.

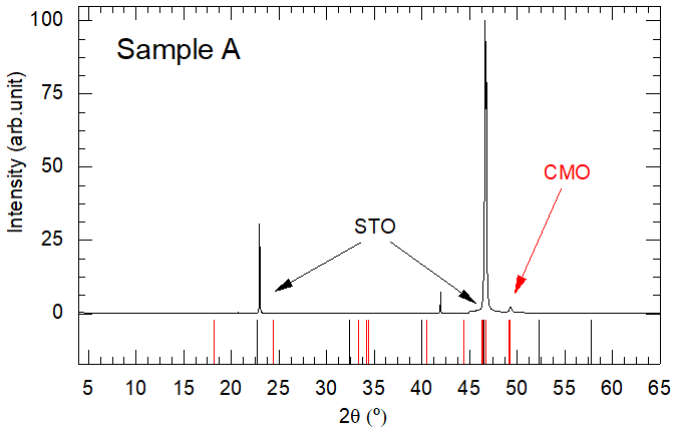

Figure 3.23 – XRD pattern of $Ca_3Mn_2O_7$ thin film deposited in STO in Bragg-Brentano (BB) mode with a sample tilt of 0.8°. On the bottom there is the XRD peaks at RT of bulk CMO (in red) and the STO substrate (in black).

In Fig. 3.23 sample A has the reflection peaks of STO substrate (at 32.3°[100] and 46.54°[200]) and a peak corresponding to the bulk CMO[ii] at 49.31°, [220] (*Acaa*). An extra peak is observed at 41.96° which corresponds to the K_{beta} peak, associated with the peak of highest intensity.

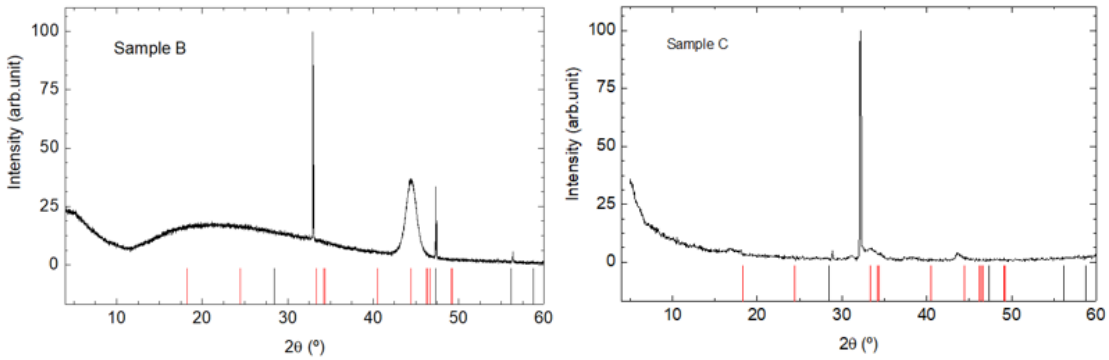

Figure 3.24 – XRD patterns of the of $Ca_3Mn_2O_7$ thin film deposited in Si. For the **sample B** it was measured in Bragg-Brentano (BB) mode with a sample tilt of 0.8°. For the **sample C** it was measured in Parallel Beam (PB) mode. On the bottom there is the XRD peaks at RT of a bulk sample of CMO (in red) and the STO substrate (in black).

[ii] At 46.64°[0 0 10] $Ca_3Mn_2O_7$ ($A2_1am$) might have been deposited but there is maybe a double contribution from the substrate peak at [200].

In Fig. 3.24 sample B has one peak from the substrate at [220] and it might have another from the target at 44.44°, [206] (*Acaa*/*A*2$_1$*am*). The **sample C** there is a lump after the most intense peak, coinciding with the peaks of 32.96°, [115] (*Acaa*/*A*2$_1$*am*), 34.28°, [200] (*Acaa*/*A*2$_1$*am*) of the bulk CMO.

3.5.3 Magnetic Characterization

In Fig. 3.25 is shown the temperature dependence of the sample A magnetization. Two modes were measured: the FCC (300 K → 5 K) and FCH (5 K → 300 K), both under a magnetic field of 200 Oe. Comparing the two curves there is a slight parallel mismatch, after 160 K until room temperature.

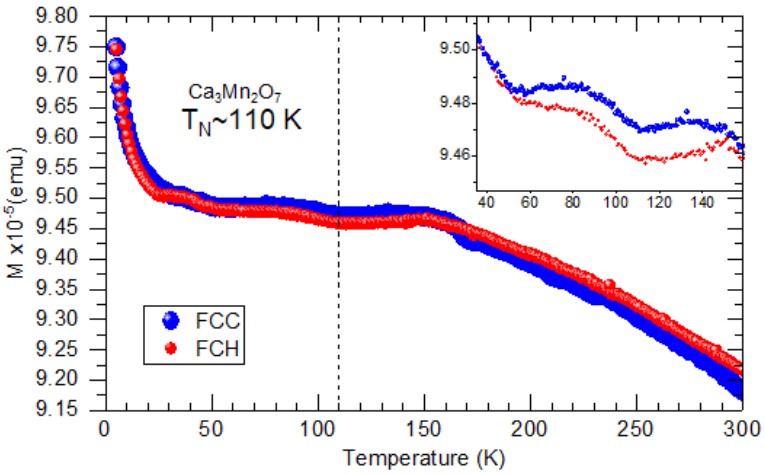

Figure 3.25 – Magnetization of sample A measured at 200 Oe for the FCC and the FCH modes. Inset: the corresponding enlarged view around the Néel temperature of the bulk $Ca_3Mn_2O_7$.

When the temperature decreases from the room temperature, both the FCC and the FCH curves increase. At 160 K the curves tend to stabilize until ≈ 115 K. This anomaly at 115 K might suggest the presence of $Ca_3Mn_2O_7$ corroborating the XRD data. An upturn below 50 K is supposed to be due to the paramagnetic spins at low concentration[112].

In Fig. 3.26 is shown the temperature dependence of the sample C magnetization. Two modes were measured: the FCC (300 K → 5 K) and FCH (5 K → 300 K), both under a magnetic field of 200 Oe. Comparing the two curves there is a slight, though increasing, mismatch up to room temperature.

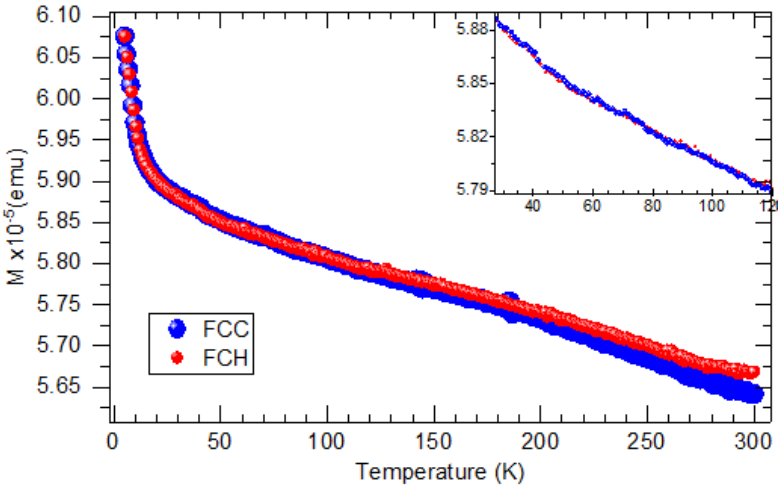

Figure 3.26 – Magnetization of sample C measured at 200 Oe for the FCC and the FCH modes. Inset: the corresponding enlarged view around the Néel temperature of the bulk $Ca_3Mn_2O_7$.

When the temperature decreases from the room temperature, both the FCC and the FCH curves decrease in what would be described as a regular paramagnetic behavior with a possible ferromagnetic contribution. Here, no anomaly around 115 K is observed, hence casting doubt about the presence of $Ca_3Mn_2O_7$.

3.5.4 Morphological Characterization and EDS Analysis

The surface morphology and composition of sample A and sample C were checked by Scanning Electron Microscopy (SEM) and Electron-Dispersive X-ray Spectroscopy (EDS). In Fig. 3.27 and Fig. 3.28 are displayed the micrographs taken with secondary electrons (SE) for both samples. In sample C it was taken the care to focus the electron beam in a region out of the bluish spot observed in Fig. 3.22.

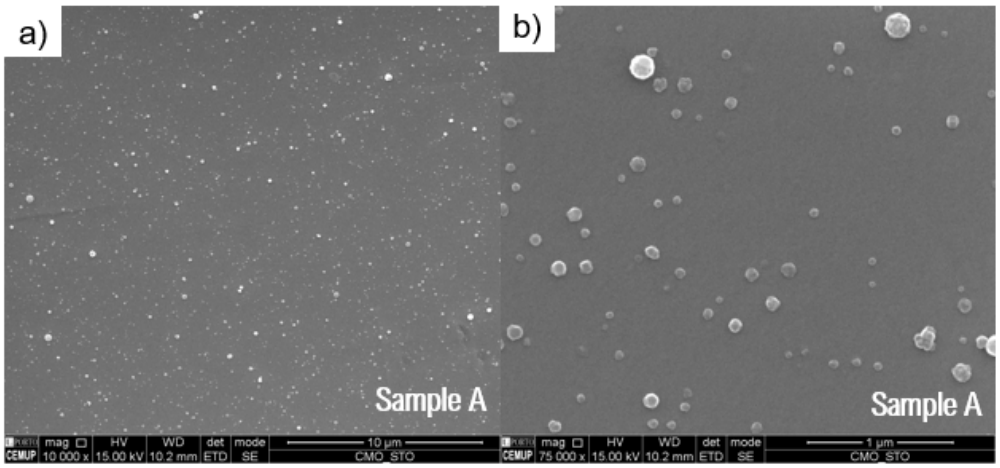

Figure 3.27 – Scanning electron microscope micrographs performed in sample A using secondary electrons (SE). With a magnification: **a)** 10 000× and **b)** 75 000×.

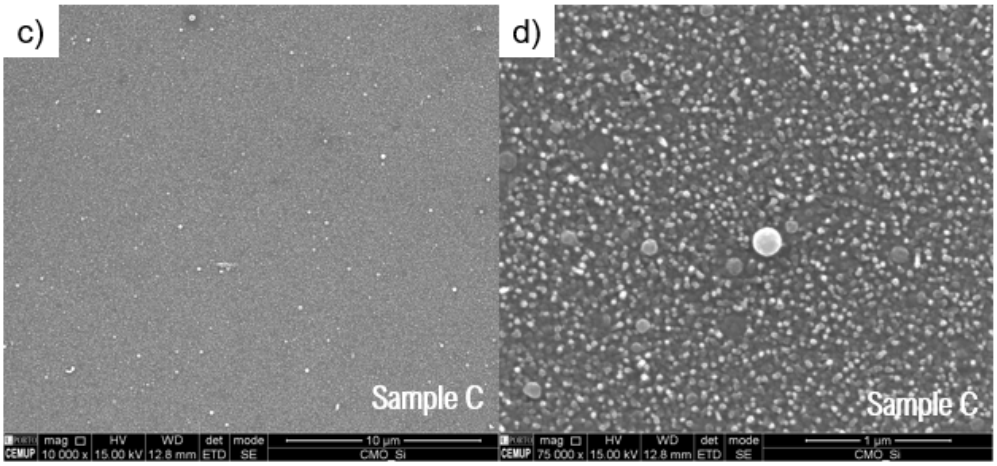

Figure 3.28 – Scanning electron microscope micrographs performed in sample C using secondary electrons (SE). With a magnification: **c)** 10 000× and **d)** 75 000×.

According to the results, the sample surface seems to be composed of sphere-like structures ($r_{max} \approx 0.2$ µm) across their surface, even in the sample A which at the naked eye has a uniform appearance, unlike the bluish spot in sample C (see Fig. 3.22). Afterwards, the grains were analyzed to obtain the corresponding elemental composition, using the EDS analysis of x-rays. In Figs. 3.29 and 3.30 are displayed the EDS analysis of sample A, which was target in the darker regions, and sample C.

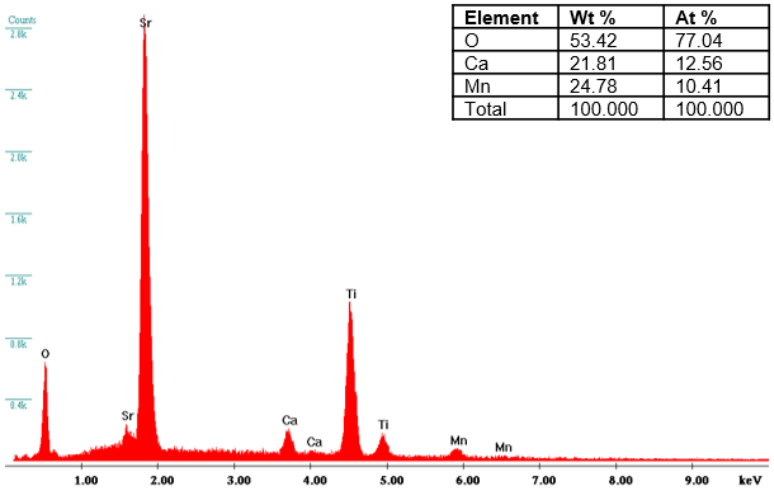

Element	Wt %	At %
O	53.42	77.04
Ca	21.81	12.56
Mn	24.78	10.41
Total	100.000	100.000

Figure 3.29 – EDS result of sample A in a uniform region shown in 3.27 d).

In Fig. 3.29 it is possible to observe a high contribution from the substrate elements, *i.e.* Sr, Ti and O. Bear in mind that the oxygen peak has two contributions, one from the substrate and another from the deposited compound $Ca_3Mn_2O_7$. It was also found the presence of Ca, Mn and O, thus assuring that some of the material was deposited.

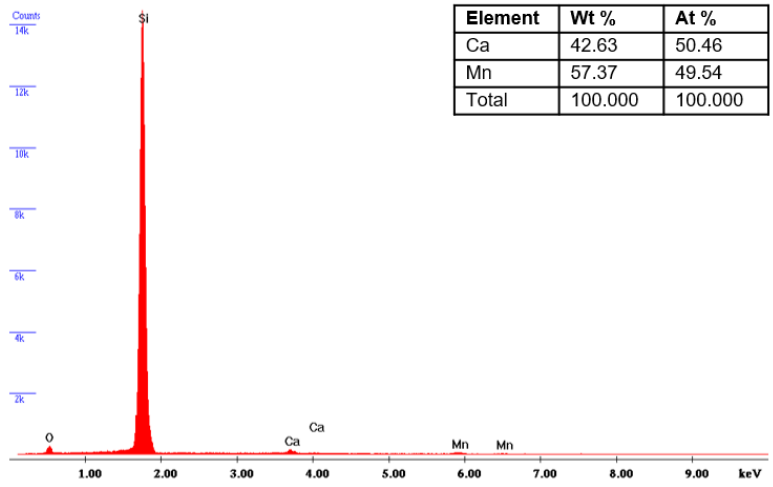

Element	Wt %	At %
Ca	42.63	50.46
Mn	57.37	49.54
Total	100.000	100.000

Figure 3.30 – EDS result of sample C in the darker region shown in 3.28 c).

Like in the previous sample, in Fig. 3.30, it is possible to observe a high contribution of the substrate, *i.e.* Si, and another from the elements of the deposited compound $Ca_3Mn_2O_7$. Here, it was found the presence of Ca, Mn and O, thus assuring that some of the material was deposited.

The chemical composition of the spheres previously described remain of unknown. They might be $Ca_3Mn_2O_7$ or binary oxides like CaO which formed on top of the film. To find a more accurate stoichiometry of these structures it would be interesting to use XPS analysis in these particular regions since it has low penetration depth into the samples, thus reducing the contribution from the substrate.

Summarizing, analysing the XRD and SEM measurements the sample A (STO substrate), which was further confirmed in the magnetic measurements, might have the correct phase of $Ca_3Mn_2O_7$ deposited. For the sample C (Si substrate), based on the XRD, SEM and magnetic measurements, it is not possible to conclude that it was a successful epitaxial deposition of $Ca_3Mn_2O_7$.

CHAPTER 4

Calcium Titanium Oxides

4.1 Introduction

Increasing attention was paid to this compound when, as with $Ca_3Mn_2O_7$, it was found by *Benedek et al.*[1] to have a rich set of coupled structural and polar domains in which TiO_6 octahedral rotations induce hybrid improper ferroelectricity (HIF). The polarization was found from first-principles calculations to be $P \approx 20\mu C/cm^2$ [1,57].

In 2015, *Oh et al.*[25] provided an experimental demonstration of HIF and confirmed an interesting ferroelectric domain structure resulting from orthorhombic twins and switchable planar polarization in $(Ca, Sr)_3Ti_2O_7$. Nonetheless, its extremely high coercive field of 120 kV/cm make applications in other fields infeasible[25]. One path used to minimize this factor was through epitaxial thin films achieving the ultra-low value of 2−5 kV/cm[53], see section 3.5. More recently, in 2016 *Nonandic*[57] studied the polar and antipolar domains of $Ca_3Ti_2O_7$ and enumerates possible ferroelectric switching pathways.

In the case of $Ca_{n+1}Ti_nO_{3n+1-\delta}$, it is concluded by *I. Kim et al.*[71] that the electrical transport phenomena of the system has a strong dependence on the oxygen deficiency δ, but little dependence of the stacking number of the perovskite slabs, n. While $Ca_3Mn_2O_7$ is known for its high electric leakage.

By comparison with $BiFeO_3$, the Curie temperature for the ferroelectric transition is expected to be higher than 1000 K. *Liu et al.*[52] in DSC studies have found a first-order transition at around 1100 K that suggested to be the paraelectric to ferroelectric transition, hence it is predicted to be the value of ferroelectric Curie temperature.

Calcium titanium-based oxides were investigated in studies related to ferroelectric photovoltaic materials[28], oxides superconductors[71] and with several ion doping for optimization of optical properties, see section 4.1.2.

4.1.1 Structural Transitions

The $Ca_3Ti_2O_7$ compound consists of a stacking of two $CaTiO_3$ layers of perovskite blocks (n = 2) intercalated periodically with a rock-salt like CaO layer.

Early studies[18], on what was latter called Ruddlesden Popper phase series, investigated $Sr_3Ti_2O_7$ identifying these structures to be a non-polar *I*4/*mmm*. Later, using neutron powder diffraction, *Elcombe et al.*[125] confirmed for $Sr_3Ti_2O_7$ the high symmetry

group, nevertheless, the analog $Ca_3Ti_2O_7$ was attributed to the space group symmetry of $A2_1am$.

In the pursuit to find the transition to the high symmetry group $I4/mmm$, which *in situ* high-temperature XRD at 1173 K found to be true, *Liu et al.*[52] used DSC measurements discovering a phase transition at around 1100 K, see Fig. 4.1.

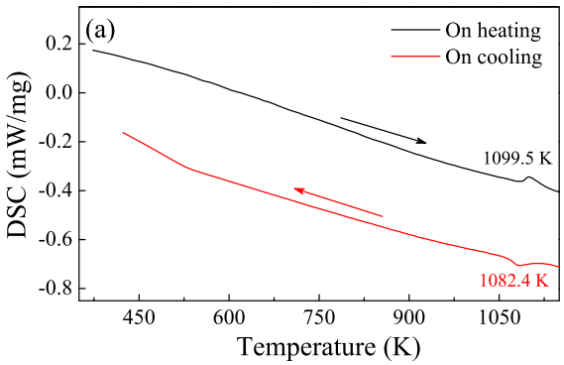

Figure 4.1 – The temperature dependence of DSC signs for $Ca_3Ti_2O_7$ ceramics during the heating and cooling cycles. (Taken from Ref. 52)

Note that in $Ca_3Ti_2O_7$ there is no condensation of an intermediary phase, *Acaa*, as seen in $Ca_3Mn_2O_7$.

4.1.2 Ion substitution

There are several ways in which this compound could be engineered to tune some of its properties. For example, the ferroelectric coercive field greatly decreased via Na doping. Oxygen vacancies were found to increase after Na doping, which contributes to the increasing leakage current[56], see Fig. 4.2.

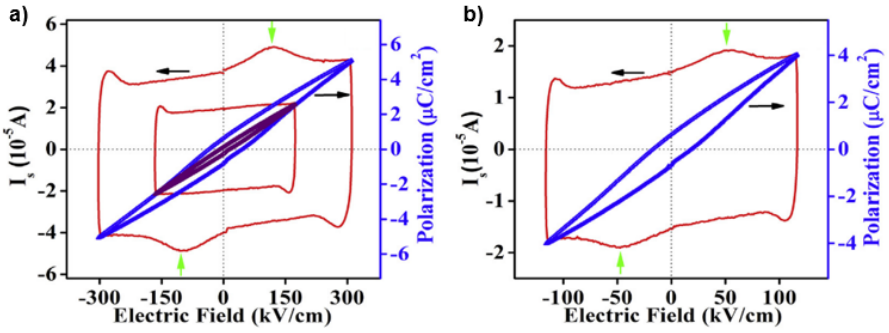

Figure 4.2 – Polarization-electric field (P-E) hysteresis loops (blue line) and displacement currents (black line) recorded at room temperature with a different electric filed at frequency of 100 Hz for **a)** $Ca_3Ti_2O_7$ and **b)** $Ca_{2.85}Na_{0.15}Ti_2O_7$ ceramics. (Taken from Ref. 56)

Okazaki et al.[126] investigated the Rh-doped $Ca_3Ti_2O_7$ and found out that photocatalytic activities were enhanced in these materials after treated under a reducing at-

mosphere of 3% H_2. *Cao et al.*[127] demonstrated that the maximum peak intensity of $Ca_3Ti_2O_7:Eu^{3+}$ phosphor can be improved significantly with Bi^{3+} co-doped due to an energy transfer between the Bi^{3+} and Eu^{3+} ions. *Wang et al.*[128] confirmed a continuous exponential distribution of trap depth of 0.69 – 0.92 eV in $Ca_3Ti_2O_7:Pr^{3+}$ phosphor, which is found to be responsible for the persistent luminescence behavior.

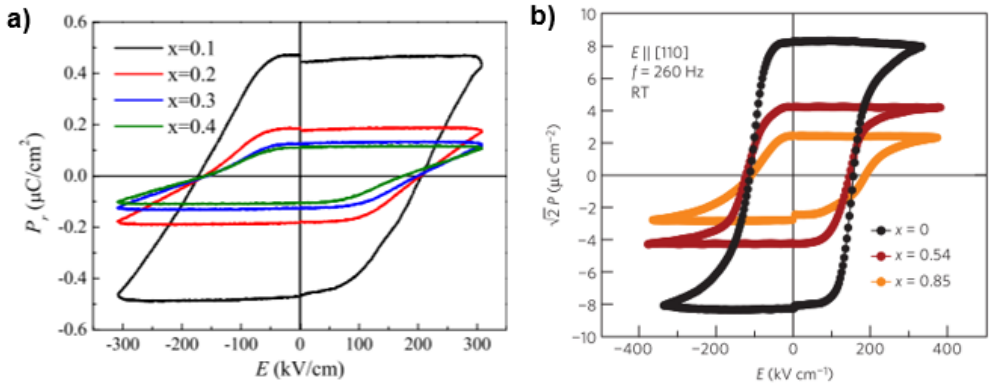

Figure 4.3 – The ferroelectric P-E field loops of **a)** $Ca_{3-x}Sr_xTi_2O_7$ ceramics measured at room-temperature by the PUND method. **b)** Single crystals at room-temperature with electric fields applied along the [110] direction at frequency f = 260 Hz. (Taken from Refs. 25,27)

In terms of structure, as it was seen from neutron powder diffraction[125] and XRD[27] data, when substituting the Ca sites with Sr the octahedral rotation and tilt angles are reduced, see Fig. 4.4 a). This decrease affects directly the remnant polarization in these ceramics as it can be seen from Fig. 4.3 b).

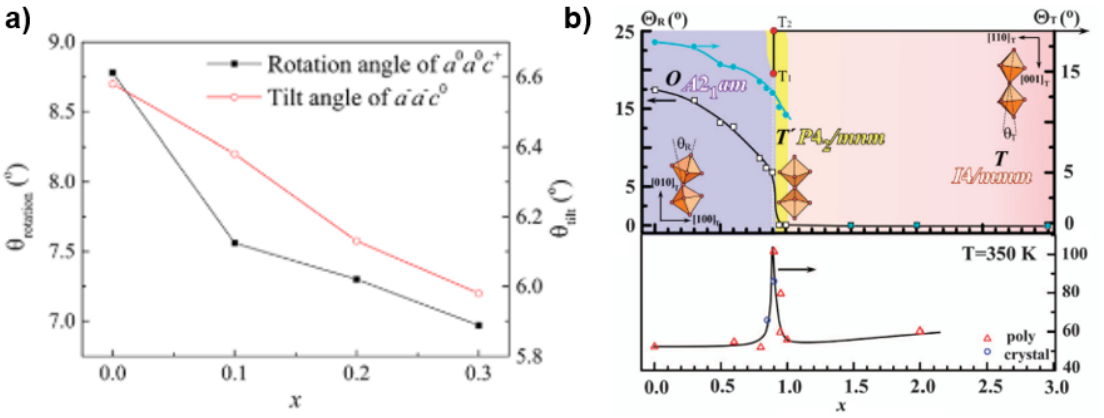

Figure 4.4 – Structural phase diagram of $Ca_{3-x}Sr_xTi_2O_7$ with the angles of octahedral rotation (θ_r) and octahedral tilting (θ_t) as a function of Sr doping, x. (Taken from Refs. 27,32)

The results[25,32] from $Ca_{3-x}Sr_xTi_2O_7$ single crystals and ceramics show that a ferroelectric $A2_1am$ phase can exist up to $x \approx 0.9$, and for the first time is reported a new non-polar $P4_2/mnm$ phase in the range x = 0.9 – 1 at room temperature.

In section 5.2, of the following chapter 5 it is addressed the issue of $Ca_3Mn_2O_7$ doped with Ti atoms.

4.2 Sample Preparation

As with the manganese RP samples, it was performed a standard solid-state reaction for the preparation of $Ca_3Ti_2O_7$ polycrystalline samples using high purity reagents $CaCO_3$ (99.0%, Sigma-Aldrich) and TiO_2 (99.8%, Sigma-Aldrich) mixed in a stoichiometric ratio and carefully ground in an agate mortar. These samples were then pressed into pellets and underwent through a set of heat treatments (at 1123 K for 3h and at 1473 K for 12h) with intermediate grindings as described in section 2.1. The crucible was made of high-density Al_2O_3 and in between annealings the samples were reground and pelletized.

According to *Senn et al.*[106] above 1150 K the sample starts to decompose. *R. Roth*[129] measured the melting point of $Ca_3Ti_2O\,7$ at about 1740°C. To assure that the compounds produced were pure it was performed a powder x-ray diffraction pattern, see Fig. 4.5.

4.3 $Ca_3Ti_2O_7$ (n=2)

4.3.1 Crystallographic Characterization

The sample's crystallographic structure and lattice parameters have been fully checked and refined employing x-ray powder diffraction (XRD) taken at RT (300 K). The XRD pattern of a non-implanted $Ca_3Ti_2O_7$ sample is shown in Fig. 4.5. Rietveld analysis was performed using the least-squares refinement program Fullproof.

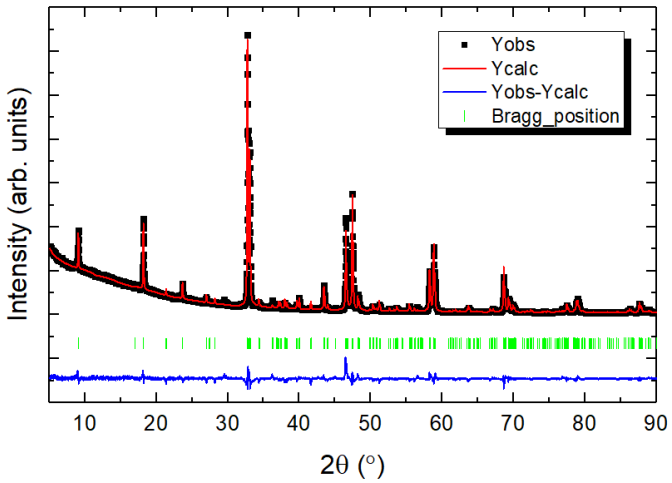

Figure 4.5 – X-Ray diffraction pattern of $Ca_3Ti_2O_7$ at room temperature and the respective Rietveld refinement output, namely, the calculated diffraction pattern, the difference between the calculated and measured diffractogram (at the bottom) and the respective Bragg reflections for this symmetry.

It was used just one phase ($A2_1am$) to fit the XRD diffraction pattern obtained. The fit reveals that the sample is a single-phase, and it is not observed the presence of substantial asymmetry in the diffraction profile and shift in peak positions reported pre-

viously[52]. The crystallographic parameters from the refinement are a = 19.501(1) Å, b = 5.413(1) Å, and c = 5.419(1) Å.

4.3.2 Perturbed Angular Correlation Results

At the ISOLDE facilities, using a radioactive probe of ^{111m}Cd in the temperature range from 10 K to 1220 K, as described in the section 2.4.2, it was obtained the following results. In the Fig. 4.6 depicts the experimental R(t) anisotropy function and the respective Fourier transform. The fits to the R(t) experimental data were performed considering only electric quadrupole interactions and static regular EFG distributions assumed to be Lorentzian-like.

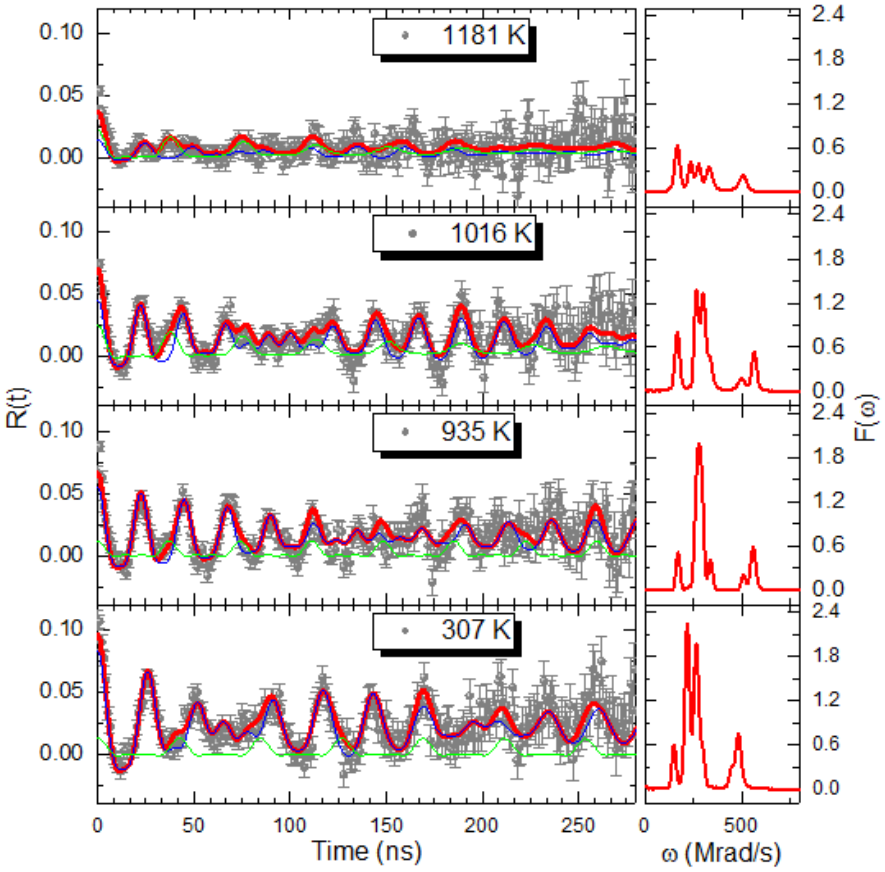

Figure 4.6 – Representative R(t) functions with the corresponding fits, and respective Fourier transforms taken at different temperatures using the ^{111m}Cd probe. The blue (EFG1) and green (EFG2)lines correspond to two different fractions at characteristic frequency which its sum is represented in red.

Here, it is possible to notice a possible mixture of two EFG throughout the measured temperature range.

In the Fig. 4.7 it is represented the fitting parameters obtained for the distinct measuring temperatures, such as the EFG principal component, V_{zz}, and the asymmetry parameter, η. At room temperature the EFG1 is characterized by a $V_{zz} \approx 76.36$ V/A^2

with $\eta \approx 0.8$ (identified as the blue dots). The EFG2 is characterized by a $V_{zz} \approx 76.4$ V/A^2 with $\eta \approx 0$ (identified as the green dots).

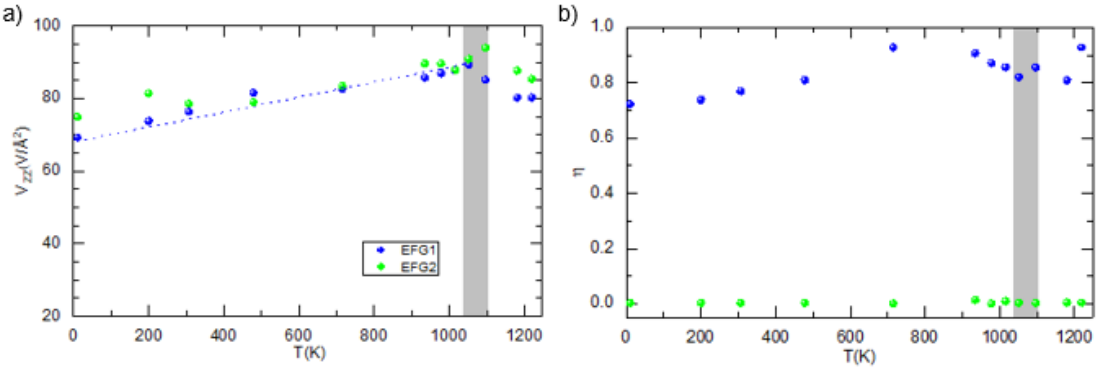

Figure 4.7 – **a)** Experimental electric field gradient, V_{zz}, for the $Ca_3Ti_2O_7$ sample and the **b)** asymmetry parameter evolution with temperature. The grey bar represents the temperature interval where is described to happen the structural transition [26,52].

In order to evaluate the EFG1 tendency is possible to use a least-squares fit defined in Eq.3.3.3. It was obtained a positive coefficient of $\alpha_{EFG1} = 2.45(1)x10^{-4}$ K^{-1}. This coefficient is in the same order as to the one found for Ca_2MnO_4 and $Ca_3Mn_2O_7$.

In Fig. 4.8 it is presented the phase evolution, *i.e.*, the temperature evolution of the associated EFG1 and EFG2 phases described previously in Fig. 4.6. From 10 K until 935 K there is a main presence of the EFG1 with a small contribution from EFG2. After 979 K up to 1097 K the presence of the EFG1 and EFG2 is about 60% to 40%, respectively, ending up with a increase of EFG2 above 1181 K.

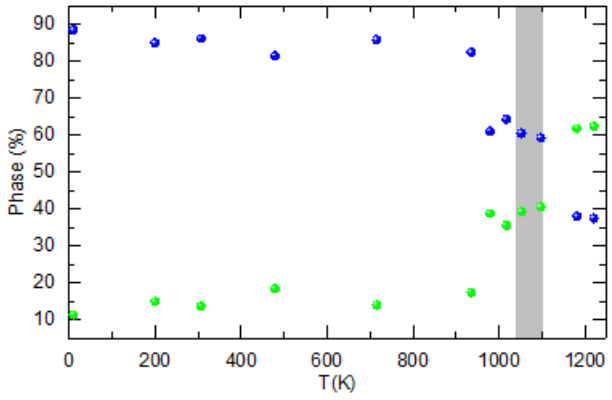

Figure 4.8 – Temperature evolution of the two fractions observed in $Ca_3Ti_2O_7$(Fig. 4.7). The grey bar represents the temperature interval where is described to happen the structural transition [26,52].

When observing the asymmetry evolution within the temperature above 1000 K, see Fig. 4.7 b), the experimental results reveal a possible transition from local environment of low axial symmetry, $\eta \approx 0.8$, to a high axial symmetry $\eta \approx 0$.

The V_{zz} thermal tendency present in Fig. 4.7 a) only follows the most common trend observed in PAC measurements, i.e. a decrease in magnitude for increasing temperature[130], at high temperatures after ≈ 1050 K. Similar positive trend for the V_{zz} was seen in the $Ca_3Mn_2O_7$ for the phase $A2_1am$, see Fig. 3.20 a).

In Fig. 4.8 there is an increasing contribution to the PAC spectra from this highly symmetric phase with increasing temperature (> 1000 K). These results suggest a structural transition from the reported $A2_1am$ to a high symmetry phase, probably the $I4/mmm$ one. If this transitions comes to be confirmed, this will occur at a temperature lower than the predicted ≈ 1100 K[26,52].

About the sample stability it was studied three different samples all submitted through PAC but at different temperatures of measurement, T_M, or the after implantation annealing, T_a. Comparing all of them, both low T_a and T_M, high T_a and low T_M, low T_a and high T_M with the literature[125] XRD at room temperature ($A2_1am$ space group) no loss/gain of peak(s) is observed as well as any significant shift of the existent ones. Thus confirming the sample stability under the operating temperatures of the PAC measurements.

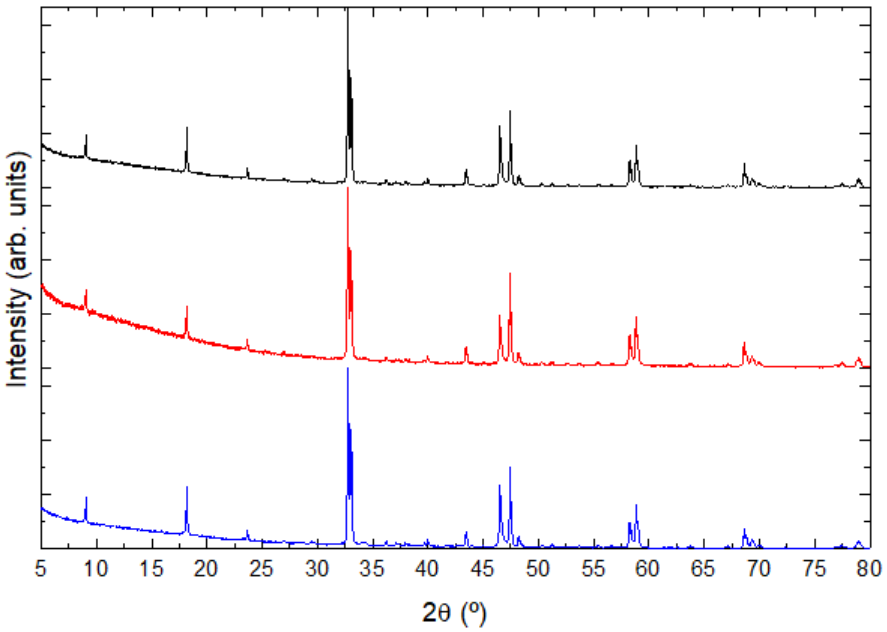

Figure 4.9 – XRD patterns of $Ca_3Ti_2O_7$ samples that went through PAC measurements at high temperatures. In black a reference sample that was not under any PAC measurement, in red a sample annealed at 1283 K and measured at 308 K and in blue a sample annealed at 1123 K and measured at 1181 K.

CHAPTER 5

Other Ruddlesden Popper Compounds

5.1 Designing new compounds

From an engineering point of view, chemistry provides a valuable path for exploration of the properties of the materials, as previously discussed when introduced the tolerance factor in section 1.1.4 and for the particular case of $Ca_3Ti_2O_7$ in section 4.1.2.

As *Benedek*[12] explains, in the case of magnetism in perovskite $AMnO_3$[i] manganites, through substitution on the A-site with cations of different ionic radius, it is possible to control the degree to which the MnO_6 octahedra are rotated and hence the Mn–O–Mn bond angle. Such changes in bond angles can have a profound effect on the interaction between spins. As an example, in the simplest case of spins interacting through super exchange, materials in which the Mn–O–Mn bond angles are closer to 180° are generally AFM, whereas materials in which the Mn–O–Mn bond angles are closer to 90° tend to be FM.

In fact, the substitution at the A-site could improve the properties of perovskite-like materials effectively, *e.g.* it has been reported that substitution of the alkali element Na can further improve piezoelectric properties of the KNO_3 ceramic[131], while in Na-doped $BiFeO_3$ nanoparticles, an increased Na^+ doping could reduce the bandgap and simultaneously cause the decrease of the leakage current[132].

The study of the compound $Ca_2Mn_{1-x}Ti_xO_4$ for novel near-infrared (NIR) reflective black pigments[133] revealed an increase in lattice volume with the Ti^{4+} addition. From these results, the composition was optimized to $Ca_2Mn_{0.85}Ti_{0.15}O_4$ to satisfy both of appropriate black color and the NIR reflecting property. This black pigment has enough NIR solar reflectance (R = 66.2%), higher than those of the commercially available pigments (R < 50%).

In the particular case of RP phase series[54] the question of dimensionality, *i.e.* the number of n layers of perovskite, also plays a role in properties enhancement. For $Sr_{n+1}Ti_nO_{3n+1}$ it was found a decrease in bandgaps with increasing n (for finite n). Through first-principles calculations[15] it is suggested that as n increases and the TiO_6 octahedra become connected for increasing distances along the c-axis, leading to the band edge electronic states being less confined.

[i] Where A is typically an alkaline-earth and/or a rare-earth cation(s).

5.2 $Ca_3Mn_{2-x}Ti_xO_7$ (n = 2)

5.2.1 Introduction

As a pursuit for room temperature operation materials that combine both polarization and magnetization in bulk n = 2 RP oxides, intermediary compositions with different amounts of manganese and/or titanium were synthesized and studied[26,52]. This particular choice comes from the theoretical calculation and experimental results[1,25] that pointed out that $Ca_3Mn_2O_7$ and $Ca_3Ti_2O_7$ are HIFs. Furthermore, the valence of Ti^{4+} is equivalent to the Mn^{4+} and when introducing the Ti^{4+} it is expected to stabilize the polar phase of $Ca_3Mn_2O_7$ at higher temperatures, although sacrificing the magnetic properties with a decreasing Néel temperature, see Fig. 5.2 a).

In the polarization studies[26,52] it was found that a nominal 1.5 of titanium composition could reveal an hysteresis loop, see Fig. 5.1 a) and that a small increase in the manganese concentration increases the coercive field, E_c, and decreased the remanent polarization, P_r. It is reasoned by *Liu* to be attributed by the much smaller theoretical predicted electric polarization of $Ca_3Mn_2O_7$[1] (about 5μC/cm^2). Also in comparison with single crystals, although the remanent polarization is smaller the coercive field of 120 kV/cm is almost the same[52].

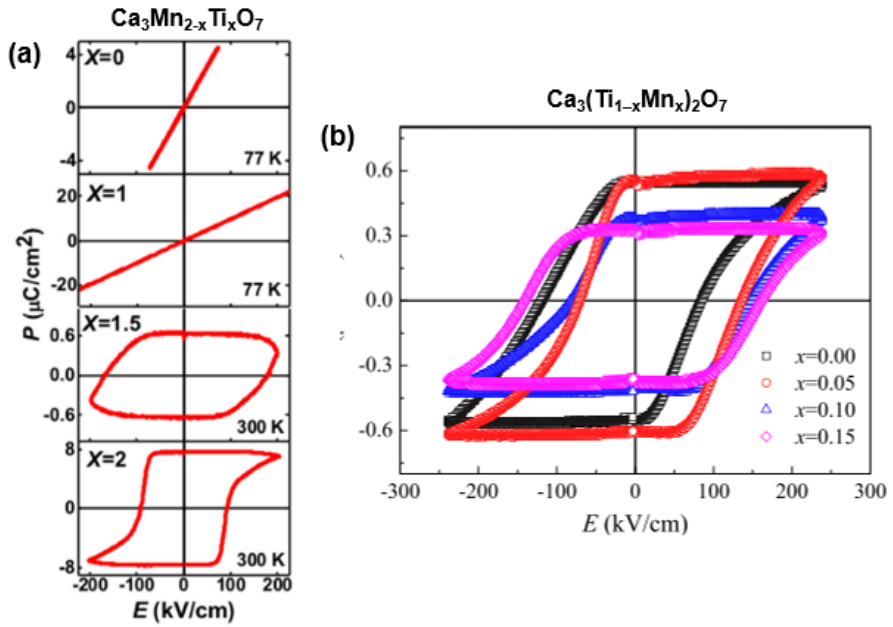

Figure 5.1 – **a)** Electric polarization, P, vs. electric field, E, curves of the four crystals at the frequency of f = 1 kHz. The $P(E)$ curves are straight lines for x = 0 and 1 even at 77 K. P(E) hysteresis loops appear for x = 1.5 and 2 crystals at room temperature. **b)** P(E) hysteresis loops of $Ca_3(Ti_{1-x}Mn_x)_2O_7$ ceramics at room temperature with electrical fields up to 240 kV/cm at frequency of 100 Hz. (Taken from Refs. 26,52)

In titanium rich compounds, it was found from DSC measurements that the temperature of the $I4/mmm$ to the $A2_1am$ phase transition decreased linearly with an higher

content of manganese in the $Ca_3(Ti, Mn)_2O_7$ ceramics[52], see Fig. 5.2b).

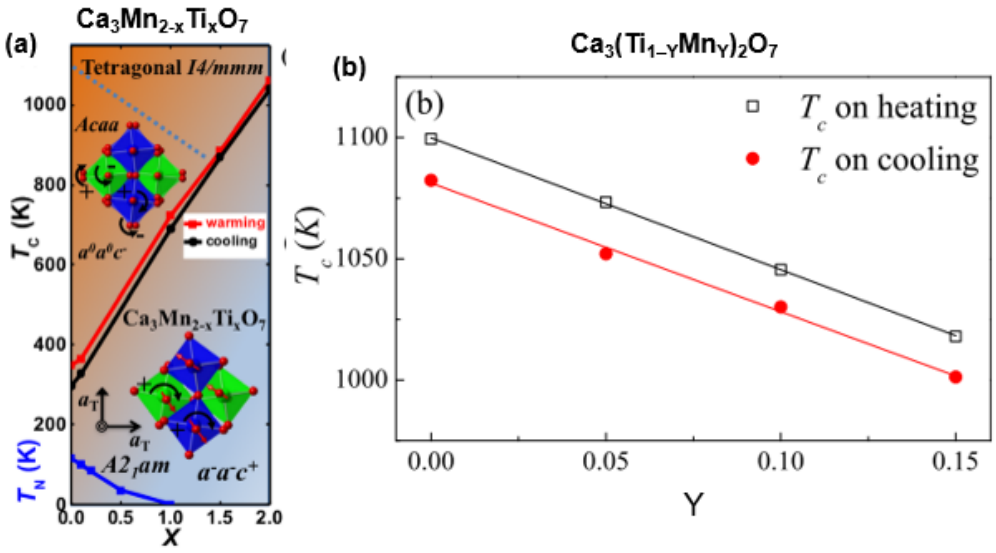

Figure 5.2 – **a)** Structural Transition of $Ca_3Mn_{2-x}Ti_xO_7$ in the spectrum of calcium manganese (x = 0) to calcium titanium oxide (x = 2) from low to high temperatures. **b)** The temperatures of endothermic and exothermic peaks for $Ca_3(Ti_{1-y}Mn_y)_2O_7$ ceramics in DSC measurements. The solid lines are the linear fitting results. (Taken from Refs. 26,52)

5.2.2 Sample Preparation

Low titanium doped polycrystalline samples of $Ca_3Mn_{2-x}Ti_xO_7$ (x = 0.1, 0.25) were prepared using a conventional solid state reaction method. The samples were synthesized from high purity $CaCO_3$ (99.9%, Alfa), MnO_2 (99.9%, Alfa) and TiO_2 (99.8%, Aldrich) powders, mixed in a stoichiometric ratio and carefully grinded in an agate mortar.

These samples were then pressed into pellets and underwent through a set of heat treatments with intermediate grindings as described in Section 2.1 with the parameters summarized in Table 5.1. The crucible was made of high-density Al_2O_3 and in between annealings the samples were regrinded and pelletized.

Table 5.1 – Nominal compositions, Calcination, Heat Treatment and label of the studied calcium manganese/titanium naturally layered perovskites.

Nominal Composition	Calcination	Heat Treatment	Label
$Ca_3Mn_{1.9}Ti_{0.1}O_7$	1123 K (3h)	1648 K (12h)	CMTOC
$Ca_3Mn_{1.75}Ti_{0.25}O_7$	1123 K (3h)	1648 K (12h)	CMTOB

To assure that the compounds produced were pure it was performed a powder x-ray diffraction pattern (XRD).

5.2.3 Crystallographic Characterization

The sample's crystallographic structure and lattice parameters have been checked and by means of XRD, in Bragg Brentano (BB) mode at RT (300 K). In Fig. 5.3, it is presented the XRD pattern of $Ca_3Mn_{2-x}Ti_xO_7$ for $x = 2, 0.25, 0.1, 0$ and the simulated XRD pattern of *Acaa* and $A2_1am$ from CIFs data[106] at 260 K..

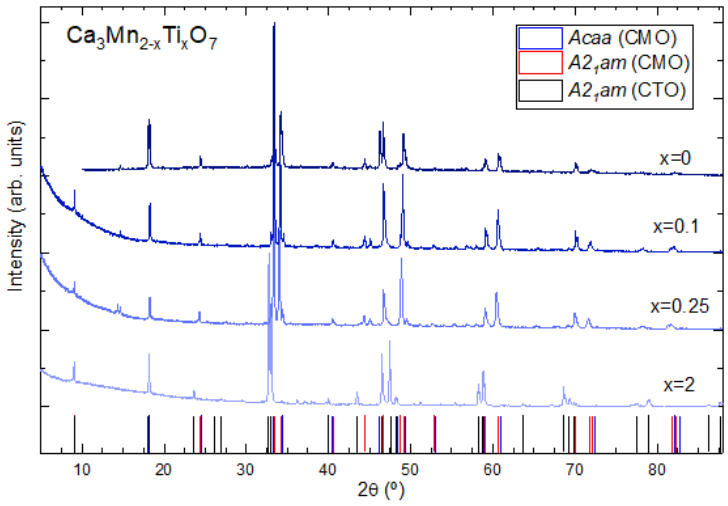

Figure 5.3 – X-Ray diffraction patterns of $Ca_3Mn2\text{-}xTi_xO_7$ with $x = 0, 0.1, 0.25$ and 2. At the bottom there is the correspondent peaks for $Ca_3Mn_2O_7$ in the *Acaa* (in blue), $A2_1am$ (in red) phases and for $Ca_3Ti_2O_7$ in the $A2_1am$ (in black) phase.

It is confirmed, in both intermediary compounds, a main contribution from the $A2_1am$ phase of the $Ca_3Mn_2O_7$. As expected, with an increase in the titanium concentration there is a distortion on the structure, in which the peaks of highest intensity are shifted to lower angles, see Fig. 5.4.

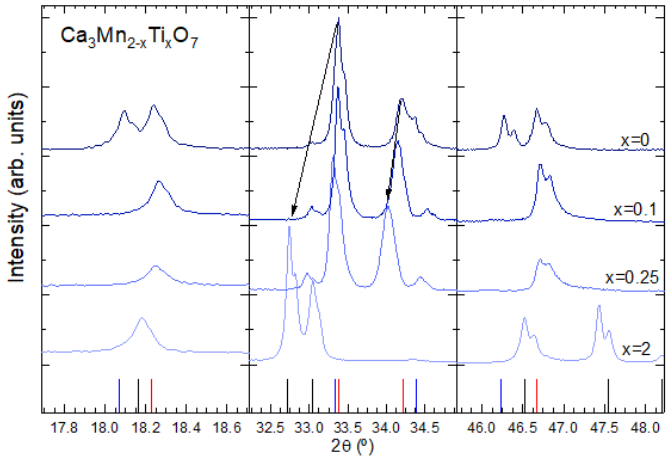

Figure 5.4 – Close up of the XRD patterns of $Ca_3Mn2\text{-}xTi_xO_7$ with $x = 0, 0.1, 0.25$ and 2. At the bottom there is the correspondent peaks for $Ca_3Mn_2O_7$ in the *Acaa* (in blue), $A2_1am$ (in red) phases and for $Ca_3Ti_2O_7$ in the $A2_1am$ (in black) phase.

In opposition to what was found in Fig. 3.15 for $Ca_3Mn_2O_7$, the *Acaa* phase appears to be not present in the intermediary compounds at room temperature, see Fig.5.4.

The peak at ≈ 14.5 °(in samples containing manganese) was formerly observed in Ca_2MnO_4 leading to the conclusion that a small portion of lower-dimensional (n = 1) is present in the sample.

5.2.4 Magnetic Characterization

In Fig. 5.5 is shown the temperature dependence of the molar magnetic susceptibility, χ_{molar}. Two modes were measured: the FCC (300 K → 5 K) and FCH (5 K → 300 K), both under a magnetic field of 200 Oe. Comparing the two curves no major differences can be observed[ii], *i.e.* a satisfactory overlap between them is observed, thus assuring the system reversibility as a function of temperature.

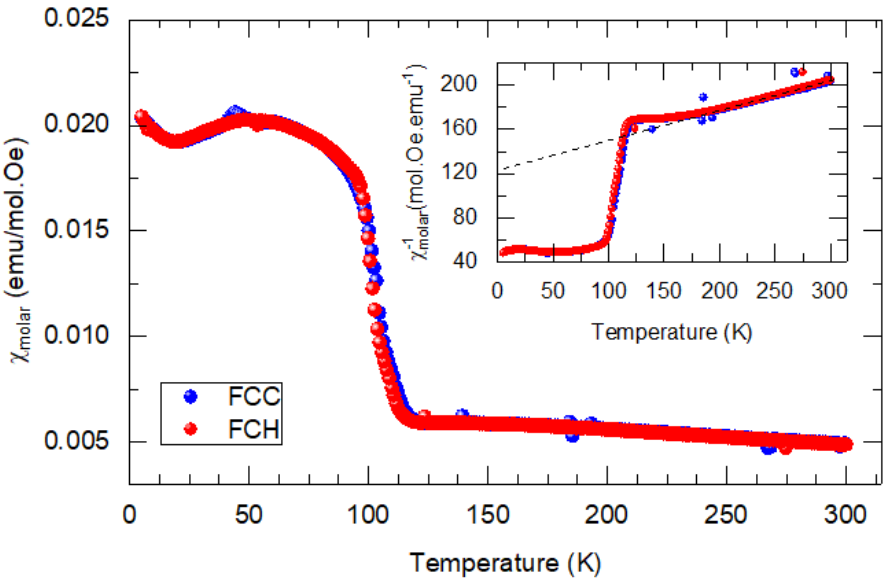

Figure 5.5 – Molar magnetic susceptibility of $Ca_3Mn_{1.9}Ti_{0.1}O_7$ measured at 200 Oe during heating (FCH) and cooling (FCC). Inset: Molar inverse magnetic susceptibility, χ^{-1}, of $Ca_3Mn_{1.9}Ti_{0.1}O_7$ as a function of temperature. The dashed line represents the Curie Weiss law.

When the temperature decreases from room temperature, both the FCC and the FCH curves sharply increase at 104 K which corresponds to the Néel Temperature, T_N. This value is lower than the one found for $Ca_3Mn_2O_7$ (T_N = 111 K), as seen by *Gao et. al*[26]. Observing the inverse magnetic susceptibility in the interval 250 K to 300 K it is seen that the magnetic susceptibility follows approximately the Curie-Weiss law (see Eq.2.5). Using a linear fit in this region it is obtained $C \approx 3.61$ emu Oe K mol^{-1} and $\theta_p \approx -441$ K. The μ_{eff} is estimated to be $5.37\mu_B$ which is, as previously noticed, a value much higher than the predicted value for Mn^{4+} ion. This might happen because the

[ii] The small peak at 45 K, as detected before in a FCC measurement in Section 3.4.2, comes from an experimental inaccuracy of O_2 contamination in the system[121]

linearity needed for the application of the Curie-Weiss law might not be fully reached in the temperature range.

5.2.5 Perturbed Angular Correlation Results

At the ISOLDE facilities and using a radioactive probe of ^{111m}Cd in the temperature range from 8 K to 606 K it was performed several PAC measurements as described in the Section 2.4.2.6. In the Fig. 5.6 (right side) depicts the experimental R(t) anisotropy function and the respective Fourier transform obtained by the measurements. The fits to the R(t) experimental data were performed considering only electric quadrupole interactions and static regular EFG distributions assumed to be Lorentzian-like.

Here it is possible to notice that at low temperature (< 39 K) there is one electrical field gradient, EFG1, characterized by having axially a low symmetry ($\eta \approx 0.9$). At this temperature a well defined doublet ($\omega_1 = \omega_2, \omega_3$) can be seen in Fig. 5.6 (right side). Then, at higher temperatures appears a second phase, EFG2, also characterized by having axially a low symmetry ($\eta \approx 0.9$).

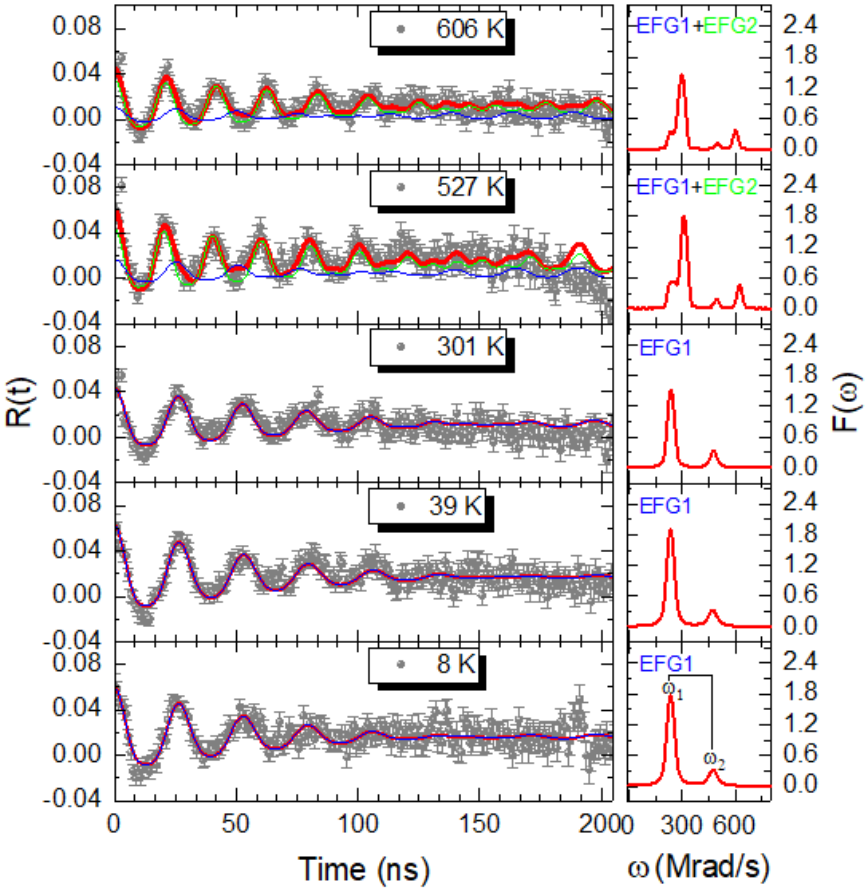

Figure 5.6 – Representative R(t) functions with the corresponding fits, and respective Fourier transforms taken at different temperatures using the ^{111m}Cd probe. The blue (EFG1) and green (EFG2) lines correspond to two different fractions at characteristic frequency, and the sum is represented in red.

In the Fig. 5.7 it is represented the fitting parameters obtained for the distinct measuring temperatures, such as the EFG principal component, V_{zz}, and the asymmetry parameter, η. At room temperature the EFG1 is characterized by a $V_{zz} \approx 75\ V/Å^2$ with $\eta \approx 0.92$ (identified as the blue dots in Fig. 5.7) while, at the highest temperature measured (606 K), the EFG2 is characterized by a $V_{zz} \approx 92.2 V/Å^2$ with $\eta \approx 0.94$ (identified as the green dots in Fig. 5.7).

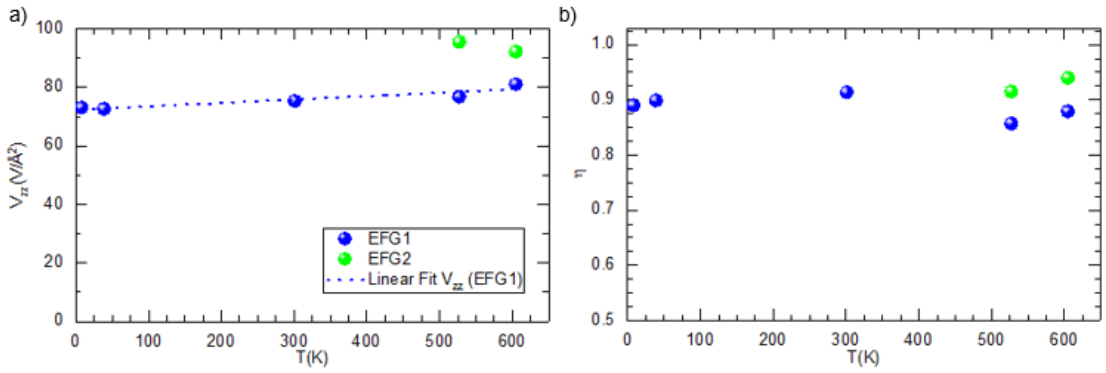

Figure 5.7 – **a)** Experimental electric field gradient, V_{zz} and the **b)** asymmetry parameter evolution with temperature for the $Ca_3Mn_{1.9}Ti_{0.1}O_7$ sample.

In order to evaluate the EFG principal component, V_{zz}, it is possible to use a least-squares fit defined in Eq. 3.3.3. It was obtained a coefficient of $\alpha_{EFG1} = 1.6(1)x10^{-4}\ K^{-1}$. This value is fairly close to the one found at low temperature, the $A2_1am$ phase, of $Ca_3Mn_2O_7$ ($1.7(3)x10^{-4}\ K^{-1}$). Additional PAC measurements at higher temperatures might confirm if EFG2 follows the trend characteristic of the *Acaa* phase as in the $Ca_3Mn_2O_7$.

In Fig. 5.8 it is presented the phase evolution, *i.e.*, the temperature evolution of the associated EFG1 and EFG2 phases described previously in Fig. 5.6. From 8 K until 301 K there is a single presence of the EFG1 with a small contribution from EFG2. After 301 K up to 606 K it is found a majority of the EFG2. The contribution of this phase increases until a maximum of ≈ 80% with an ≈ 20% of the EFG1.

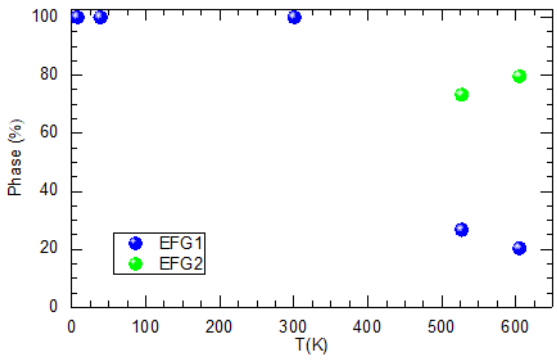

Figure 5.8 – Temperature evolution of the two EFG observed in $Ca_3Mn_{1.9}Ti_{0.1}O_7$.

When observing the asymmetry evolution, in Fig. 5.7 b), and the phase evolution in Fig. 5.8, the experimental results suggest that the appearance of this EFG2, could reveal a structural transition, in analogy with the titanium non-doped $Ca_3Mn_2O_7$. As previously seen, in $Ca_3Mn_2O_7$, there is the emergence of a second local environment, coexisting with the first one measured at low temperatures from 200 K to 500 K. It was not found any experimental study in the literature on $Ca_3Mn_{1.9}Ti_{0.1}O_7$ reporting a phase transition, although *Gao*[26] provided some guidance for intermediary compounds from $Ca_3Mn_2O_7$ to $Ca_3Ti_2O_7$, see Fig. 5.2.

Comparing with the previous work, in section 3.4.3, at room temperature the percentage of the possible polar phase, $A2_1am$, is increased from $\approx$ 77% to 100%. This could indicate an improvement in the ferroelectric properties solely with nominal doping of 0.1 of titanium.

Conclusion

Stoichiometric Ruddlesden Popper materials were produced in this work, as confirmed by XRD measurements. The obtained diffractograms proved the high purity of the Ruddlesden Popper samples Ca_2MnO_4 (n = 1), $Ca_3Mn_2O_7$ (n = 2) and $Ca_3Ti_2O_7$ (n = 2) produced for this thesis. The magnetization measurements are in agreement with what was found in the literature, hence confirming the quality of the produced samples.

The local probing gave us an insightful glimpse into the electrical field gradient evolution of the studied RP compounds, accordingly to the temperature. It was detected in Ca_2MnO_4 a possible structural phase transition from the low $I4_1/cad$ phase to a highly symmetric one at high temperatures. The critical temperature was found to be in the range from 1049 K to 1079 K.

In $Ca_3Mn_2O_7$, within the studied experimental temperature range, three local environments were unambiguously observed. From 11 K to 506 K a phase with a low asymmetry parameter ($\eta \approx 1$) is detected. Continuing to increase the temperature until 1151 K another low symmetry phase appears. From 1151 K to 1200 K is found a highly symmetric environment with $\eta \approx 0$. These are assumed to be the structural transition pathway from the low temperature $A2_1am$ polar phase, passing through the nonpolar $Acaa$ symmetry, ending in the highly symmetric space group, $I4/mmm$. Moreover, in this sample, the XRD measurements come to confirm, at room temperature, a coexistence of $A2_1am$ and $Acaa$ which is consistent with our local probe measurements and recent literature.

The Rietveld of the XRD diffractogram for the ferroelectric $Ca_3Ti_2O_7$ bulk sample in the space group $A2_1am$ was properly performed. Observing the phase percentage of the PAC fittings it was possible to detect a high increase of the phase with axial symmetry at high temperatures, thus suggesting a hypothetical structural transition above 1050 K. If later confirmed to be true, the transition occurs at a temperature lower than the predicted. As in the compounds studied before, a change in the asymmetry parameter is associated with a change in the octahedral distortions and, in this case, possibly with a change from the low temperature $A2_1am$ to the highly symmetric $I4/mmm$ phase.

On the intermediary compounds of $Ca_3Mn_{2-x}Ti_xO_7$, it was possible to produce a low Ti doped $Ca_3Mn_2O_7$ samples, as checked by XRD measurements. Here it was discussed the effect of partially substitute ions of Mn for Ti on the stabilization of the polar phase $A2_1am$.

Concerning the $Ca_3Mn_2O_7$ thin films deposition, the analysis performed seems to indicate that perhaps in one case we might have the desired composition. Nevertheless the depositing conditions must be further exploited to assure that the target material of

the PLD is deposited in the substrates with the pretended composition.

Future work

The main conclusions of this thesis were thoroughly presented in this chapter. Nevertheless, this doesn't mean that there is a closed door in what was shown here. A detailed analysis of the phase transitions suggested here is ongoing.

Now, having the production and characterization of these Ruddlesden Popper materials controlled, it is interesting to push boundaries exploring with other doping quantities of titanium and other elements in the crystal structure. Partially, this work has already begun.

Bibliography

[1] N. A. Benedek, C. J. Fennie, Hybrid improper ferroelectricity: A mechanism for controllable polarization-magnetization coupling, Phys. Rev. Lett. **106** (10) (2011) 3–6. arXiv:1007.1003, doi:10.1103/PhysRevLett.106.107204.

[2] J. H. Lee, L. Fang, E. Vlahos, X. Ke, Y. W. Jung, L. F. Kourkoutis, J.-w. Kim, P. J. Ryan, T. Heeg, M. Roeckerath, V. Goian, M. Bernhagen, J. W. Freeland, R. Uecker, P. C. Hammel, K. M. Rabe, S. Kamba, D. A. Muller, C. J. Fennie, P. Schiffer, V. Gopalan, E. Johnston-halperin, D. G. Schlom, A strong ferroelectric ferromagnet created by means of spin-lattice coupling, Nature **466** (2010) 954–958. doi:10.1038/nature09331.

[3] N. A. Benedek, J. M. Rondinelli, H. Djani, P. Ghosez, P. Lightfoot, Understanding ferroelectricity in layered perovskites: new ideas and insights from theory and experiments, Dalt. Trans. **44** (23) (2015) 10543–10558. doi:10.1039/C5DT00010F.

[4] A. B. Harris, Symmetry analysis for the Ruddlesden-Popper systems $Ca_3Mn_2O_7$ and $Ca_3Ti_2O_7$, Phys. Rev. B - Condens. Matter Mater. Phys. **84** (6) (2011) 1–21. arXiv:arXiv:1101.2593v1, doi:10.1103/PhysRevB.84.064116.

[5] M. M. Vopson, Fundamentals of Multiferroic Materials and Their Possible Applications, Crit. Rev. Solid State Mater. Sci. **40** (4) (2015) 223–250. doi:10.1080/10408436.2014.992584.

[6] M. Fiebig, T. Lottermoser, D. Meier, M. Trassin, The evolution of multiferroics, Nat. Rev. Mater. **1** (2016) 16046. doi:10.1038/natrevmats.2016.46.

[7] A. Ecija, K. Vidal, A. Larrañaga, L. Ortega-San-Martín, M. I. Arriortua, Synthetic Methods for Perovskite Materials - Structure and Morphology, 2012. doi:10.5772/36540.

[8] M. Dawber, C. Lichtensteiger, M. Cantoni, M. Veithen, P. Ghosez, K. Johnston, K. M. Rabe, J. M. Triscone, Unusual behavior of the ferroelectric polarization in $PbTiO_3$/$SrTiO_3$ superlattices, Phys. Rev. Lett. **95** (17) (2005) 2–5. doi:10.1103/PhysRevLett.95.177601.

[9] W. Zhu, L. Pi, Y. Huang, S. Tan, Y. Zhang, Electrically induced decrease of magnetization in $Ca_3Mn_2O_7$, Appl. Phys. Lett. **101** (19) (2012) 192407. doi:10.1063/1.4767139.

[10] L. G. Tejuca, J. L. G. Fierro, J. M. D. Tascón, Structure and Reactivity of Perovskite-Type Oxides, Adv. Catal. **36** (1989) 133.

[11] L. Pan, G. Zhu (Eds.), Perovskite Materials: Synthesis, Characterisation, Properties, and Applications, BoD - Books on Demand, 2016.

[12] N. A. Benedek, A. T. Mulder, C. J. Fennie, Polar octahedral rotations : A path to new multifunctional materials, J. Solid State Chem. **195** (2012) 11–20. doi:10.1016/j.jssc.2012.04.012.

[13] J. H. Haeni, C. D. Theis, D. G. Schlom, W. Tian, X. Q. Pan, H. Chang, I. Takeuchi, X. D. Xiang, Epitaxial growth of the first five members of the $Sr_{n+1}Ti_nO_{3n+1}$ Ruddlesden Popper

homologous series, Appl. Phys. Lett. **78** (21) (2001) 3292–3294. doi:10.1063/1.1371788.

[14] L. Yan, H. Niu, C. A. Bridges, P. A. Marshall, J. Hadermann, G. Van Tendeloo, P. R. Chalker, M. J. Rosseinsky, Unit-cell-level assembly of metastable transition-metal oxides by pulsed-laser deposition, Angew. Chemie - Int. Ed. **46** (24) (2007) 4539–4542. doi:10.1002/anie.200700119.

[15] C. H. Lee, N. J. Podraza, Y. Zhu, R. F. Berger, S. Shen, M. Sestak, R. W. Collins, L. F. Kourkoutis, J. A. Mundy, H. Wang, Q. Mao, X. Xi, L. J. Brillson, J. B. Neaton, D. A. Muller, D. G. Schlom, Effect of reduced dimensionality on the optical band gap of $SrTiO_3$, Appl. Phys. Lett. **102** (12) (2013) 1–6. doi:10.1063/1.4798241.

[16] M. A. McCoy, R. W. Grimes, W. E. Lee, Phase stability and interfacial structures in the SrO - $SrTiO_3$ system, Philos. Mag. A **75** (3) (1997) 833–846. doi:10.1080/01418619708207205.

[17] S. N. Ruddlesden, P. Popper, New compounds of the K_2NIF_4 type, Acta Crystallogr. **10** (8) (1957) 538–539. doi:10.1107/S0365110X57001929.

[18] S. N. Ruddlesden, P. Popper, The compound $Sr_3Ti_2O_7$ and its structure, Acta Crystallogr. **11** (1) (1958) 54–55. doi:10.1107/S0365110X58000128.

[19] D. Balz, K. Plieth, Die Struktur des Kaliumnickelfluorids, K_2NiF_4, Zeitschrift für Elektrochemie, Berichte der Bunsengesellschaft für Phys. Chemie **59** (6) (1955) 545–551. doi:10.1002/bbpc.19550590613.

[20] C. Ablitt, A. A. Mostofi, N. C. Bristowe, M. S. Senn, A. Sanson, Control of Uniaxial Negative Thermal Expansion in Layered Perovskites by Tuning Layer Thickness, Front. Chem. **6** (2018) 1–13. doi:10.3389/fchem.2018.00455.

[21] Y. Moritomo, A. Asamitsu, H. Kuwahara, Y. Tokura, Giant magnetoresistance of manganese oxides with a layered perovskite structure, Nature **380** (6570) (1996) 141–144. doi:10.1038/380141a0.

[22] T. Takata, Y. Furumi, K. Shinohara, A. Tanaka, M. Hara, J. N. Kondo, K. Domen, Photocatalytic Decomposition of Water on Spontaneously Hydrated Layered Perovskites, Chem. Mater. **9** (5) (1997) 1063–1064. doi:10.1021/cm960612b.

[23] P. A. Salvador, K. B. Greenwood, J. R. Mawdsley, K. R. Poeppelmeier, T. O. Mason, Substitution behavior and stable charge carrier species in long-bond length layered cuprates, Chem. Mater. **11** (7) (1999) 1760–1770. doi:10.1021/cm9811489.

[24] E. Bousquet, M. Dawber, N. Stucki, C. Lichtensteiger, P. Hermet, S. Gariglio, J. M. Triscone, P. Ghosez, Improper ferroelectricity in perovskite oxide artificial superlattices, Nature **452** (7188) (2008) 732–736. doi:10.1038/nature06817.

[25] Y. S. Oh, X. Luo, F. T. Huang, Y. Wang, S. W. Cheong, Experimental demonstration of hybrid improper ferroelectricity and the presence of abundant charged walls in $(Ca, Sr)_3Ti_2O_7$ crystals, Nat. Mater. **14** (4) (2015) 407–413. arXiv:1411.6315, doi:10.1038/nmat4168.

[26] B. Gao, F. T. Huang, Y. Wang, J. W. Kim, L. Wang, S. J. Lim, S. W. Cheong, Interrelation between domain structures and polarization switching in hybrid improper ferroelectric $Ca_3(Mn, Ti)_2O_7$, Appl. Phys. Lett. **110** (22) (2017) 0–4. doi:10.1063/1.4984841.

[27] G. J. Li, X. Q. Liu, J. J. Lu, H. Y. Zhu, X. M. Chen, Crystal structural evolution and hybrid

improper ferroelectricity in Ruddlesden-Popper $Ca_{3-x}Sr_xTi_2O_7$ ceramics, J. Appl. Phys. **123** (1) (2018) 0–5. doi:10.1063/1.5001956.

[28] H. Wang, G. Gou, J. Li, Ruddlesden-Popper perovskite sulfides $A_3B_2S_7$: A new family of ferroelectric photovoltaic materials for the visible spectrum, Nano Energy **22** (2016) 507–513. doi:10.1016/j.nanoen.2016.02.036.

[29] A. M. Glazer, The classification of tilted octahedra in perovskites, Acta Crystallogr. Sect. B Struct. Crystallogr. Cryst. Chem. **28** (11) (1972) 3384–3392. doi:10.1107/s0567740872007976.

[30] H. D. Megaw, Crystal Structure of Double Oxides of The Perovskite Type, Proc. Phys. Soc. **58** (326).

[31] H. T. Stokes, E. H. Kisi, D. M. Hatch, C. J. Howard, Group-theoretical analysis of octahedral tilting in ferroelectric perovskites, Acta Crystallogr. Sect. B **58** (2006) 934–938.

[32] F. T. Huang, B. Gao, J. W. Kim, X. Luo, Y. Wang, M. W. Chu, C. K. Chang, H. S. Sheu, S. W. Cheong, Topological defects at octahedral tilting plethora in bi-layered perovskites, Nat. Publ. Gr. **1** (2016) 1–6. arXiv:1606.01203, doi:10.1038/npjquantmats.2016.17.

[33] V. M. Goldschmidt, Die Gesetze der Krystallochemie, Naturwissenschaften **14** (21) (1926) 477–485. doi:10.1007/bf01507527.

[34] N. A. Benedek, C. J. Fennie, Why Are There So Few Perovskite Ferroelectrics?, J. Phys. Chem. C **117** (26) (2013) 13339–13349.

[35] A. T. Mulder, N. A. Benedek, J. M. Rondinelli, C. J. Fennie, Turning ABO_3 antiferroelectrics into ferroelectrics: Design rules for practical rotation-driven ferroelectricity in double perovskites and $A_3B_2O_7$ Ruddlesden-Popper compounds, Adv. Funct. Mater. **23** (38) (2013) 4810–4820. arXiv:1205.5526, doi:10.1002/adfm.201300210.

[36] C. J. Bartel, C. Sutton, B. R. Goldsmith, R. Ouyang, C. B. Musgrave, L. M. Ghiringhelli, M. Scheffler, New Tolerance Factor to Predict The Stability of Perovskite Oxides and Halides, Sci. Adv. **5** (2) (2019) 1–19. doi:10.1126/sciadv.aav0693.

[37] H. Schmid, Multi-ferroic magnetoelectrics, Ferroelectrics **162** (1) (1994) 317–338. doi:10.1080/00150199408245120.

[38] H. Schmid, The Dice - Stone Der Würfelstein : Some Personal Souvenirs Around the Discovery of the First Ferromagnetic Ferroelectric, Ferroelectric **427** (1) (2012) 1–33. doi:10.1080/00150193.2012.673896.

[39] P. Curie, Sur la symétrie dans les phénomènes physiques, symétrie d'un champ électrique et d'un champ magnétique, J. Phys. Theor. Appl. **3** (1) (1894) 393–415.

[40] W. Eerenstein, N. D. Mathur, J. F. Scott, Multiferroic and magnetoelectric materials, Nature **442** (7104) (2006) 759–765. doi:10.1038/nature05023.

[41] N. A. Hill, Why Are There so Few Magnetic Ferroelectrics?, J. Phys. Chem. B **104** (2000) 6694–6709.

[42] B. K. Ponomarev, S. A. Ivanoc, Y. F. Popov, V. Negrii, B. S. Red'kin, Magnetoelectric Properties of Some Rare Earth Molybdates, Ferroelectrics **161** (1994) 43–48.

[43] M. Vopsaroiu, M. Stewart, T. Hegarty, A. Muniz-Piniella, N. McCartney, M. Cain, G. Srinivasan, Experimental determination of the magnetoelectric coupling coeffi-

cient via piezoelectric measurements, Meas. Sci. Technol. **19** (4) (2008) 0–5. doi:10.1088/0957-0233/19/4/045106.

[44] J. Varignon, N. C. Bristowe, É. Bousquet, P. Ghosez, Novel magneto-electric multiferroics from first-principles calculations, Comptes Rendus Phys. **16** (2) (2015) 153–167. arXiv:arXiv:1410.4047v1, doi:10.1016/j.crhy.2015.01.011.

[45] J. Valasek, Piezo-Electric and Allied Phenomena in Rochelle Salt, Phys. Rev. **17** (4) (1921) 475–481. doi:10.1103/PhysRev.17.475.

[46] P. Ghosez, J.-m. Triscone, Coupling of three lattice instabilities, Nat. Publ. Gr. **10** (4) (2011) 269–270. doi:10.1038/nmat3003.

[47] J. M. Perez-Mato, M. Aroyo, A. García, P. Blaha, K. Schwarz, J. Schweifer, K. Parlinski, Competing structural instabilities in the ferroelectric Aurivillius compound $SrBi_2Ta_2O_9$, Phys. Rev. B - Condens. Matter Mater. Phys. **70** (21) (2004) 1–14. doi:10.1103/PhysRevB.70.214111.

[48] E. E. Mccabe, E. Bousquet, C. P. Stockdale, C. A. Deacon, T. T. Tran, P. S. Halasyamani, M. C. Stennett, N. C. Hyatt, Proper Ferroelectricity in the Dion-Jacobson Material $CsBi_2Ti_2NbO_{10}$: Experiment and Theory, Chem. Mater. **27** (24) (2015) 8298–8309. doi:10.1021/acs.chemmater.5b03564.

[49] C. J. Fennie, K. M. Rabe, Ferroelectric transition in $YMnO_3$ from first principles, Phys. Rev. B **72** (2005) 1–4. doi:https://doi.org/10.1103/PhysRevB.72.100103.

[50] A. Malashevich, D. Vanderbilt, First Principles Study of Improper Ferroelectricity in $TbMnO_3$, Phys. Rev. Lett. **101** (2008) 1–4. doi:10.1103/PhysRevLett.101.037210.

[51] P. Tolédano, J. C. Tolédano, Order-parameter symmetries for improper ferroelectric nonferroelastic transitions, Phys. Rev. B **14** (7) (1976) 3097–3109. doi:10.1103/PhysRevB.14.3097.

[52] X. Q. Liu, J. W. Wu, X. X. Shi, H. J. Zhao, H. Y. Zhou, R. H. Qiu, W. Q. Zhang, X. M. Chen, Hybrid improper ferroelectricity in Ruddlesden-Popper $Ca_3(Ti, Mn)_2O_7$ ceramics, Appl. Phys. Lett. **106** (20) (2015) 5–9. doi:10.1063/1.4921624.

[53] X. Li, L. Yang, C. F. Li, M. F. Liu, Z. Fan, Y. L. Xie, C. L. Lu, L. Lin, Z. B. Yan, Z. Zhang, J. Y. Dai, J. M. Liu, S. W. Cheong, Ultra-low coercive field of improper ferroelectric $Ca_3Ti_2O_7$ epitaxial thin films, Appl. Phys. Lett. **110** (4) (2017) 1–6. doi:10.1063/1.4974217.

[54] M. J. Pitcher, P. Mandal, M. S. Dyer, J. Alaria, P. Borisov, H. Niu, J. B. Claridge, M. J. Rosseinsky, Tilt engineering of spontaneous polarization and magnetization above 300 K in a bulk layered perovskite, Science **347** (2015) 420–424. doi:10.1126/science.1262118.

[55] Y. Wang, F.-t. Huang, X. Luo, B. Gao, S.-w. Cheong, The First Room-Temperature Ferroelectric Sn Insulator and Its Polarization Switching Kinetics, Adv. Mater. **29** (2) (2016) 1–5. doi:10.1002/adma.201601288.

[56] C. Huang, W. Wong-Ng, W. F. Liu, X. N. Zhang, Y. Jiang, P. Wu, B. Y. Tong, H. Zhao, S. Y. Wang, Major improvement of ferroelectric and optical properties in Na-doped Ruddlesden-Popper layered hybrid improper ferroelectric compound, $Ca_3Ti_2O_7$, J. Alloys Compd. **770** (2019) 582–588. doi:10.1016/j.jallcom.2018.08.172.

[57] E. A. Nowadnick, C. J. Fennie, Domains and ferroelectric switching pathways in $Ca_3Ti_2O_7$

from first principles, Phys. Rev. B **94** (10) (2016) 1–12. arXiv:1606.06345, doi:10.1103/PhysRevB.94.104105.

[58] K. Scheel, Versuche ueber die ausdehnung fester koerper, insbesondere von quarz in richtung der hauptachse, platin, palladium und quarzglas bei der temperatur der fluessigen Luft., Verh. Deutsch. Phys. Ges **9** (1907) 3–23.

[59] F. A. Hummel, Thermal expansion properties of natural Lithia minerals, Foote Prints **10** (2) (1948) 3–11.

[60] F. A., Thermal Expansion Properties of Some Lithia Minerals, J. Am. Ceram. Soc. **34** (1951) 235–239.

[61] J. P. Boilot, J. P. Salanié, G. Desplanches, D. L. Potier, Phase Transformation in $Na_{1+x}Si_xZr_2P_{3-x}O_{12}$, Mater. Res. Bull. **14** (1979) 1469–1477.

[62] A. W. Sleight, Negative thermal expansion materials, Curr. Opin. Solid State Mater. Sci. **3** (1998) 128–131. doi:10.1039/A904297K.

[63] M. T. Dove, V. Heine, K. D. Hammonds, Rigid unit modes in framework silicates, Mineral. Mag. **59** (397) (1995) 629–639. doi:10.1180/minmag.1995.059.397.07.

[64] V. Heine, P. R. Welche, M. T. Dove, Geometrical origin and theory of negative thermal expansion in framework structures, J. Am. Ceram. Soc. **82** (7) (1999) 1793–1802. doi:10.1111/j.1151-2916.1999.tb02001.x.

[65] C. Lind, Two Decades of Negative Thermal Expansion Research: Where do we stand?, Materials **5** (6) (2012) 1125–1154. doi:10.3390/ma5061125.

[66] E. Grüneisen, Theorie des festen Zustandes einatomiger Elemente, Ann. Phys. **344** (12) (1912) 257–306. doi:10.1002/andp.19123441202.

[67] W.-t. Chen, C. Ablitt, N. C. Bristowe, A. A. Mostofi, T. Saito, Y. Shimakawa, M. S. Senn, Negative thermal expansion in high pressure layered perovskite Ca_2GeO_4, Chem. Comun. **55** (2019) 2984–2987. doi:10.1039/c8cc09614g.

[68] M. Ratner, Solid state chemistry techniques, Int. J. Quantum Chem. **34** (1) (1988) 87–87. doi:10.1002/qua.560340110.

[69] C. N. R. Rao, J. Gopalakrishnan, New Directions in Solid State Chemistry, Cambridge University Press, Cambridge, 1997. doi:10.1017/CBO9780511623141.

[70] C. Pithan, D. Hennings, R. Waser, Progress in the synthesis of nanocrystalline $BaTiO_3$ powders for MLCC, Int. J. Appl. Ceram. Technol. **2** (1) (2005) 1–14. doi:10.1111/j.1744-7402.2005.02008.x.

[71] I. S. Kim, M. Itoh, T. Nakamura, Electrical conductivity and metal-nonmetal transition in the perovskite-related layered system $Ca_{n+1}Ti_nO_{3n+1} - \delta$ (n = 2, 3, and ∞), J. Solid State Chem. **101** (1) (1992) 77–86. doi:10.1016/0022-4596(92)90203-8.

[72] A. C. Pierre, Introduction to Sol-Gel Processing, The International Series in Sol-Gel Processing: Technology & Applications, Springer US, 1998.

[73] C. Popescu, G. Dorcioman, A. C. Popescu, Laser Ablation Applied for Synthesis of Thin Films: Insights into Laser Deposition Methods, in: Appl. Laser Ablation - Thin Film Depos. Nanomater. Synth. Surf. Modif., InTech, 2016. doi:10.5772/65124.

[74] R. E. Dinnebier, S. J. L. Billinge (Eds.), Powder Diffraction, Royal Society of Chemistry, Cambridge, 2008. doi:10.1039/9781847558237.

[75] V. K. Pecharsky, P. Zavalij Y., Crystal Structure Refinement, in: Fundam. Powder Diffr. Struct. Charact. Mater., Springer-Verlag, New York, 2005, pp. 599–701. doi:10.1007/0-387-24567-7_7.

[76] A. W. Hull, A new method of chemical analysis, J. Am. Chem. Soc. **41** (8) (1919) 1168–1175. doi:10.1021/ja02229a003.

[77] Rigaku, Powder diffraction optics for SmartLab X-ray diffractometer, Rigaku J. **26** (2) (2010) 29–30.

[78] H. M. Rietveld, Line profiles of neutron powder-diffraction peaks for structure refinement, Acta Cryst. **22** (151) (1967) 151–152.

[79] J. Rodriguez-carvajal, Recent advances in magnetic structure determination by neutron powder diffraction, Phys. B **192** (1993) 55–69.

[80] L. B. McCusker, R. B. V. Dreele, D. E. Cox, D. Louërd, P. Scardie, Rietveld refinement guidelines, J. Appl. Cryst. **32** (1) (1999) 36–50. doi:10.1107/S0021889898009856.

[81] C. P. M. de Sá, Caracterização morfológica, microestrutural e microanalítica de materiais por: microscopia electrónica de varrimento - SEM e microanálise por raios X - EPMA: EDS/WDS, Tech. rep., Centro de Materiais da Universidade do Porto, Porto (2006).

[82] J. I. Goldstein, D. E. Newbury, P. Echlin, D. C. Joy, C. E. Lyman, E. Lifshin, L. Sawyer, J. R. Michael, Scanning Electron Microscopy and X-ray Microanalysis, Kluwer Academic/ Plenum Publishers, New York, 2003. doi:doi:10.1007/978-1-4615-0215-9.

[83] P. Marcon, K. Ostanina, Overview of Methods for Magnetic Susceptibility Measurement, in: PIERS, Kuala Lumpur, 2012, pp. 420–424.

[84] S. K. Range, Investigating Einstein's Space-time with Gyroscopes, in: J. Spencer, B. Kahn (Eds.), Educ. Guid. to Gravity Probe B, NASA, Stanford, 2004, p. 52.

[85] D. C. Champeney, The scattering of Mossbauer radiation by condensed matter, Rep. Prog. Phys. **42**.

[86] G. D. Morris, β -NMR, in: Hyperfine Interact. J., no. October, 2013, pp. 173–182. doi:10.1007/978-94-007-7963-1.

[87] A. Lerf, T. Butz, Nuclear Quadrupole Interaction and Time-Resolved Perturbed gamma-gamma Angular Correlation Spectroscopy : Applications in Chemistry, Materials Science, and Biophysical Chemistry, Angew. Chemie - Int. Ed. **26** (1987) 110–126.

[88] G. Schatz, A. Weidinger, Nuclear Condensed Matter Physics: Nuclear Methods and Applications, Wiley, New York, 1996.

[89] A. Lopes, Local probe studies on lattice distortions and electronic correlations in manganites, Ph.D. thesis, University of Aveiro (2006).

[90] G. Oliveira, Local probing spinel and perovskite complex magnetic systems, Ph.D. thesis, University of Porto (2012).

[91] M. B. Barbosa, Electronic structure, lattice location and stability of dopants in wide band gap semiconductors, Ph.D. thesis, Porto (2018).

[92] M. Zacate, H. Jaeger, Perturbed Angular Correlation Spectroscopy - A tool for the study of Defects and Diffusion at the Atomic Scale, Defect Diffus. Forum **311** (2011) 3–38. doi: 10.4028.

[93] J. Schell, P. Schaaf, D. C. Lupascu, Perturbed angular correlations at ISOLDE: A 40 years young technique, AIP Adv. **7** (10) (2017) 1–17. doi:10.1063/1.4994249.

[94] T. Butz, S. Saibene, T. Fraenzke, M.Weber, A "TDPAC"-Camera", Nucl. Instruments Methods Phys. Res. **284** (1989) 417–421. doi:10.1016/0168-9002(89)90311-2.

[95] M. J. G. Borge, B. Jonson, ISOLDE past , present and future, J. Phys. G Nucl. Part. Phys. **44** (044011) (2017) 20. doi:10.1088/1361-6471/aa5f03.

[96] A. M. L. Lopes, J. P. Araújo, E. Rita, J. G. Correia, V. S. Amaral, Y. Tomioka, Y. Tokura, R. Suryanarayanan, ISOLDE Collaboration, Perturbed angular correlation study of $Pr_{1-x}Ca_xMnO_3$, J. Magn. Magn. Mater. **272-276** (2004) 1667–1668. doi: 10.1016/j.jmmm.2003.12.957.

[97] J. Takahashi, N. Kamegashira, X-Ray Structural Study of Calcium Manganese Oxide By Rietveld Analysis at High Temperatures Ca_2MnO_4, Mater. Res. Bull. **28** (139) (1993) 565–573.

[98] C. Ablitt, S. Craddock, M. S. Senn, A. A. Mostofi, N. C. Bristowe, The origin of uniaxial negative thermal expansion in layered perovskites, npj Comput. Mater. **44** (2017) 1–8. doi:10.1038/s41524-017-0040-0.

[99] C. Autret, C. Martin, M. Hervieu, R. Retoux, B. Raveau, G. André, F. Bourée, Structural investigation of Ca_2MnO_4 by neutron powder diffraction and electron microscopy, J. Solid State Chem. **177** (6) (2004) 2044–2052. doi:10.1016/j.jssc.2004.02.012.

[100] A. Maignan, C. Martin, G. Van Tendeloo, M. Hervieu, B. Raveau, Ferromagnetism and magnetoresistance in monolayered manganites $Ca_{2-x}Ln_xMnO_4$, J. Mater. Chem. **8** (11) (1998) 2411–2416. doi:10.1039/a805393f.

[101] M. T. Tlili, M. Bejar, E. Dhahri, M. A. Valente, L. C. Costa, E. K. Hlil, Magnetic , Electrical Properties and Spin-Glass Effect of Substitution of Ca for Pr in $Ca_{2-x}Pr_xMnO_4$ Compounds, Open Surf. Sci. J. **1** (2009) 54–58.

[102] P. Rocha-Rodrigues, S. S. M. Santos, G. N. P. Oliveira, T. Leal, I. P. Miranda, J. G. Correia, L. Assali, H. Petrilli, J. P. Araújo, A. M. L. Lopes, Local Probe studies on the Ca_2MnO_4 structure, Phys. Rev. B (to be submitted).

[103] I. D. Fawcett, J. E. Sunstrom Iv, M. Greenblatt, M. Croft, K. V. Ramanujachary, Structure, Magnetism, and Properties of Ruddlesden-Popper Calcium Manganates Prepared from Citrate Gels, Chem. Mater. **10** (6) (1998) 3643–3651. doi:10.1021/cm980380b.

[104] N. Guiblin, D. Grebille, H. Leligny, C. Martin, $Ca_3Mn_2O_7$, Acta Crystallogr. Sect. C Cryst. Struct. Commun. **58** (2002) 3–5. doi:10.1107/S0108270101018492.

[105] H. T. Stokes, D. M. Hatch, Isotropy Subgroups of the 230 Crystallographic Space Groups, World Scientific, 1988.

[106] M. S. Senn, A. Bombardi, C. A. Murray, C. Vecchini, A. Scherillo, X. Luo, S. W. Cheong, Negative thermal expansion in hybrid improper ferroelectric Ruddlesden-popper Perovskites by symmetry trapping, Phys. Rev. Lett. **114** (3) (2015) 1–5. doi:

10.1103/PhysRevLett.114.035701.

[107] P. Rocha-Rodrigues, S. S. M. Silva, I. P. Miranda, G. Oliveira, J. G. Correia, L. V. C. Assali, H. M. Petrilli, J. P. Araújo, A. M. L. Lopes, $Ca_3Mn_2O_7$ structural path unraveled by atomic scale properties: a combined experimental and ab-initio study, Phys. Rev. B (to be published).

[108] M. Liu, Y. Zhang, L.-F. Lin, L. Lin, S. Yang, X. Li, Y. Wang, S. Li, Z. Yan, X. Wang, X.-G. Li, S. Dong, J.-M. Liu, Direct observation of ferroelectricity in $Ca_3Mn_2O_7$ and its prominent light absorption, Appl. Phys. Lett. **113** (2) (2018) 022902. doi:10.1063/1.5037525.

[109] W. H. Jung, E. Iguchi, Electrical conduction behaviour in K_2NiF_4-type $Ca_2MnO_{3.98}$ below room temperature, J. Phys. D Appl. Phys. Electr. **31** (1998) 794–799.

[110] T. Yamashita, K. Kubo, K. Nakao, T. Sakurai, S. Ikegawa, J. Sugiyama, H. Yamauchi, Electrical and magnetic properties of $(Ca_{1-x}A_x)_2MnO_4$ (A=La and Na), Phys. Rev. B **53** (21) (1996) 470–474.

[111] J. B. MacChesney, H. J. Williams, J. F. Potter, R. C. Sherwood, Magnetic Study of the Manganate Phases: $CaMnO_3$, $Ca_4Mn_3O_{10}$, $Ca_3Mn_2O_7$, Ca_2MnO_4, Phys. Rev. **164** (7) (1967) 779–785. doi:https://doi.org/10.1103/PhysRev.164.779.

[112] P. Sahlot, A. Jana, A. M. Awasthi, Exchange Bias in Multiferroic $Ca_3Mn_2O_7$ Effected by Dzyaloshinskii-Moriya Interaction, in: AIP Conf. Proc., Vol. 1942, 2018, pp. 2–6. doi:10.1063/1.5029079.

[113] G. LeFlem, P. Courbin, C.Delmas, J.-L. Soubeyroux, Magnetic Properties of the 2D-Oxides, Z. Anorg. Allg. Chem. **88** (476) (1981) 69–88.

[114] K. Tezuka, M. Inamura, Y. Hinatsu, Y. Shimojo, Y. Morii, Crystal Structures and Magnetic Properties of $Ca_{2-x}Sr_xMnO_4$, J. Solid State Chem. **145** (1999) 705–710.

[115] W.-H. Jung, Weak ferromagnetism of n=2 Ruddlesden-Popper $Ca_3Mn_2O_7$ system, J. Mater. Sci. Lett. **19** (22) (2000) 2037–2038. doi:10.1023/A:1026779406961.

[116] G. L. Flem, R. Colmet, J. Claverie, P. Hagenmuller, R. Georges, Proprietes Magnetiques et Electriques de la Phase $Ca_2MnO_{4-x}F_x$, J. Phys. Chem. Solids **41** (1980) 55–59.

[117] N. Chihaoui, M. Bejar, E. Dhahri, M. A. Valente, M. P. F. Graça, L. C. Costa, Dielectric relaxation of the Ca_2MnO_4 - δ system, J. Alloys Compd. **577** (2013) S483–S487. doi:10.1016/j.jallcom.2012.03.039.

[118] X. Zhang, W. Liu, Y. Han, C. Huang, P. Wu, W. Zhou, J. Gao, G. Rao, S. Wang, The novel optical and magnetic properties in Li-doped quasi-2D manganate $Ca_3Mn_2O_7$ particles, J. Mater. Chem. C **5** (2017) 7011–7019. doi:10.1039/C7TC01667K.

[119] M. E. Leonowicz, K. R. Poeppelmeier, J. M. Longo, Structure Determination Neutron Methods of Ca_2Mn_{04} and $Ca_2Mn_{03.5}$ by X-Ray and Neutron Diffraction, J. Solid State Chem. **59** (1985) 71–80.

[120] I. D. Fawcett, E. Kim, M. Greenblatt, M. Croft, L. A. Bendersky, Properties of the electron-doped layered manganates $La_{2-x}Ca_{1+2x}Mn_2O_7$ (0.6<x<1.0), Phys. Rev. B **62** (10) (2000) 6485–6495.

[121] Q. Design, MPMS Application Note 1014-210: Oxygen Contamination, Tech. rep. (1997).

[122] M. V. Lobanov, E. V. Tsiper, M. V. Lobanov, M. Greenblatt, E. N. Caspi, J. D. Jor-

gensen, D. V. Sheptyakov, B. H. Toby, C. E. Botez, P. W. Stephens, Crystal and magnetic structure of the $Ca_3Mn_2O_7$ Ruddlesden-Popper phase : neutron and synchrotron x-ray diffraction study, J. Phys. Condens. Matter **16** (4) (2004) 5339–5348. doi:10.1088/0953-8984/16/29/023.

[123] M. Lacotte, A. David, D. Pravarthana, C. Grygiel, G. S. Rohrer, P. A. Salvador, M. Velazquez, R. de Kloe, W. Prellier, Growth of Ca_2MnO_4 Ruddlesden-Popper structured thin films using combinatorial substrate epitaxy, J. Appl. Phys. **116** (2014) 1–9.

[124] C. Adamo, R. Misra, S. A. Denev, A. SenGupta, J. A. Mundy, J. H. Lee, D. A. Muller, V. Gopalan, P. Schiffer, D. G. Schlom, Effect of Strain and Dimensionality on the Properties of Manganites, ECS Trans. **41** (3) (2011) 283–292.

[125] M. M. Elcombe, E. H. Kisi, K. D. Hawkins, T. J. White, P. Goodman, S. Matheson, Structure determinations for $Ca_3Ti_2O_7$, $Ca_4Ti_3O_{10}$, $Ca_{3.6}Sr_{0.4}Ti_3O_{10}$ and a refinement of $Sr_3Ti_2O_7$, Acta Crystallogr. Sect. B **47** (3) (1991) 305–314. doi:10.1107/S0108768190013416.

[126] Y. Okazaki, T. Mishima, S. Nishimoto, M. Matsuda, M. Miyake, Photocatalytic activity of $Ca_3Ti_2O_7$ layered-perovskite doped with Rh under visible light irradiation, Mater. Lett. **62** (19) (2008) 3337–3340. doi:10.1016/j.matlet.2008.02.052.

[127] R. Cao, G. Chen, X. Yu, C. Cao, K. Chen, P. Liu, S. Jiang, Luminescence properties of $Ca_3Ti_2O_7$:Eu^{3+}, Bi^{3+}, R^+(R^+= Li^+, Na^+, and K^+) red emission phosphor, J. Solid State Chem. **220** (1) (2014) 97–101. doi:10.1016/j.jssc.2014.08.015.

[128] B. Wang, H. Lin, J. Xu, H. Chen, Z. Lin, F. Huang, Y. Wang, Design, Preparation, and Characterization of a Novel Red Long-Persistent Perovskite Phosphor: $Ca_3Ti_2O_7$:Pr^{3+}, Inorg. Chem. **54** (23) (2015) 11299–11306. doi:10.1021/acs.inorgchem.5b01894.

[129] R. S. Roth, Revision of the Phase Equilibrium Diagram of the Binary System Calcia-Titania, Showing the compound $Ca_4Ti_3O_{10}$, J. Res. Natl. Bur. Stand. (1934). **61** (5) (1958) 437–440.

[130] T. Kushida, G. B. Benedek, N. Bloembergen, Dependence of the Pure Quadrupole Resonance Frequency on Pressure and Temperature, Phys. Rev. **104** (5) (1956) 1364–1377.

[131] H. Du, W. Zhou, F. Luo, D. Zhu, S. Qu, Z. Pei, An approach to further improve piezoelectric properties of $(K_{0.5}Na_{0.5})NbO_3$-based lead-free ceramics, Appl. Phys. Lett. **91** (20) (2007) 28–31. doi:10.1063/1.2815750.

[132] H. Zhang, W. Liu, P. Wu, X. Hai, M. Guo, X. Xi, J. Gao, X. Wang, F. Guo, X. Xu, C. Wang, G. Liu, W. Chu, S. Wang, Novel behaviors of multiferroic properties in Na-Doped $BiFeO_3$ nanoparticles, Nanoscale **6** (18) (2014) 10831–10838. doi:10.1039/c4nr02557a.

[133] R. Oka, T. Masui, Synthesis and characterization of black pigments based on calcium manganese oxides for high near-infrared (NIR) reflectance, RSC Adv. **6** (93) (2016) 90952–90957. doi:10.1039/c6ra21443f.